Friction

(Quarterly, Started in 2013)
Volume 5 Number 4 / December 2017

ISSN 2223-7690
CN 10-1237/TH

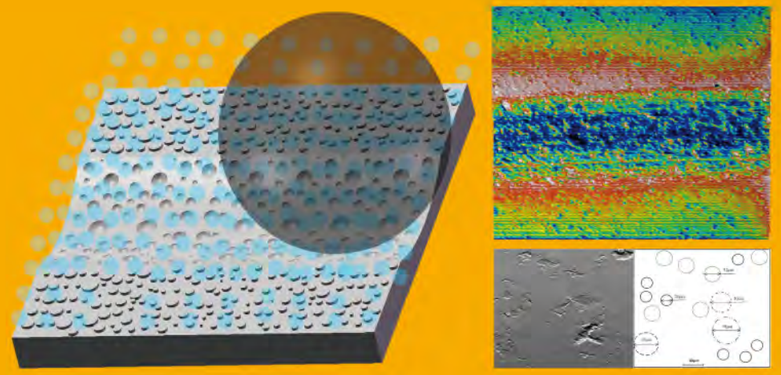

Aqueous lubrication and surface microstructures of engineering polymer materials (PEEK and PI) when sliding against Si_3N_4

摩擦（英文） （季刊，2013年创刊） 第5卷 第4期 2017年12月出版

Editor-in-Chief	Jianbin Luo	主管单位	教育部
Sponsored by	Tsinghua University	主办单位	清华大学
Supported by	Chinese Tribology Institute	学术支持	中国机械工程学会摩擦学分会
Edited by	Friction Editorial Office	主　　编	雒建斌
Published by	Tsinghua University Press	编　　辑	《摩擦》编辑部
Address	Xueyan Building, Tsinghua University, Beijing 100084, China	出版发行	清华大学出版社有限公司
		印刷单位	北京天成印务有限责任公司
Website	http://www.springer.com/40544 http://friction.tsinghuajournals.com		
Online Manuscript Submission, Review and Tracking System	http://mc03.manuscriptcentral.com/friction		

ISSN 2223-7690
12>
9 772223 769170

ISSN 2223-7690
CN 10-1237/TH

Friction

Volume 5 Number 4 2017 pp 361–454

Friction

Volume 5 Number 4 / December 2017

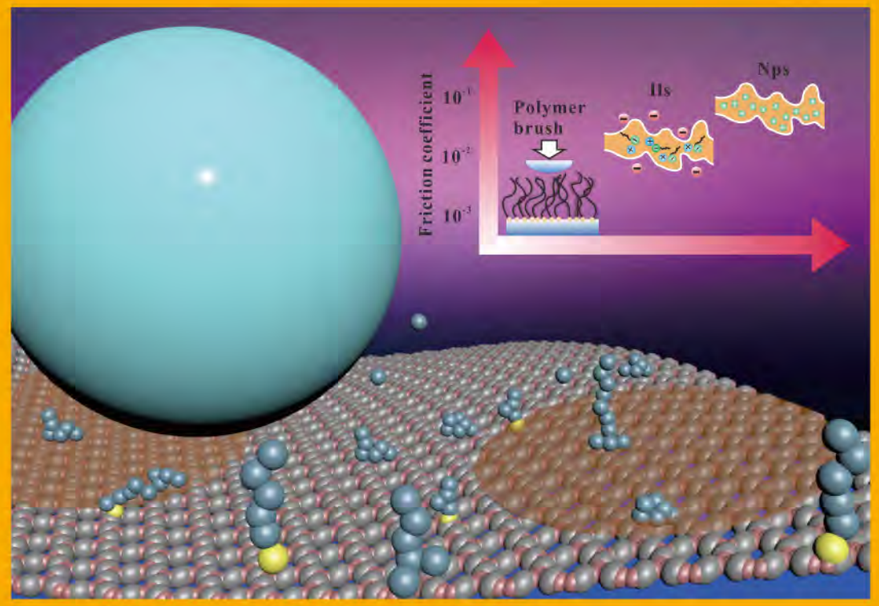

Physicochemistry aspects on frictional interfaces

TSINGHUA UNIVERSITY PRESS
Springer

Friction

ISSN 2223-7690
CN 10-1237/TH
Vol. 5, No. 4, December 2017

Contents

Review Article

Physicochemistry aspects on frictional interfaces / 361–382
Meirong CAI, Qiangliang YU, Feng ZHOU, Weimin LIU

Research Articles

Effect of stick-slip on magneto-rheological elastomer with a magnetic field / 383–391
Chenglong LIAN, Kwang-hee LEE, Jun-wook AN, Chul-hee LEE

Surface roughness characteristics effects on fluid load capability of tilt pad thrust bearings with water lubrication / 392–401
Yuechang WANG, Ying LIU, Zhanchao WANG, Yuming WANG

Tribological behavior of N-doped ZnO thin films by metal organic chemical vapor deposition under lubricated contacts / 402–413
Bolutife OLOFINJANA, Uchenna Sydney MBAMARA, Oyelayo AJAYI, Cinta LORENZO-MARTIN, Eusebius Ikechukwu OBIAJUUWA, Ezekiel Oladele Bolarinwa AJAYI

Aqueous lubrication and surface microstructures of engineering polymer materials (PEEK and PI) when sliding against Si_3N_4 / 414–428
Anying WANG, Shuai YAN, Bin LIN, Xiaofeng ZHANG, Xiaoxue ZHOU

Preparation of Ag_2O modified silica abrasives and their chemical mechanical polishing performances on sapphire / 429–436
Baichun ZHANG, Hong LEI, Yi CHEN

Friction and wear behavior of Cu–4 wt.%Ni–TiC composites under dry sliding conditions / 437–446
Pushkar JHA, Rakesh Kumar GAUTAM, Rajnesh TYAGI

Effects of impact energy on the wear resistance and work hardening mechanism of medium manganese austenitic steel / 447–454
Hui CHEN, Dong ZHAO, Qingliang WANG, Yinghuai QIANG, Jianwei QI

TSINGHUA UNIVERSITY PRESS Springer

Friction **5**(4): 361–382 (2017)
https://doi.org/10.1007/s40544-017-0191-5
ISSN 2223-7690
CN 10-1237/TH

REVIEW ARTICLE

Physicochemistry aspects on frictional interfaces

Meirong CAI, Qiangliang YU, Feng ZHOU*, Weimin LIU

State Key Laboratory of Solid Lubrication, Lanzhou Institute of Chemical Physics, Chinese Academy of Sciences, Lanzhou 730000, China

Received: 22 June 2017 / Revised: 22 August 2017 / Accepted: 02 September 2017

Abstract: Friction exists wherever relative motion occurs and is the main source of energy consumption. Lubrication plays a significant role in improving fuel efficiency, reducing emissions, and prolonging the service life of machines. Surface interactions between two moving solid surfaces or the flow of a fluid (and/or environment) on a solid surface are the primary causes of friction. Apart from the mechanical design of moving parts, surface physicochemistry is of crucial importance to lubrication. This review deals with the frontier research on controlling friction and lubrication, highlights the importance of physicochemistry aspects, and enumerates the state-of-the-art chemistry solutions to tribological issues. It aims at inspiring talented young scientists from different fields to make significant contributions to the area.

Keywords: physicochemistry; friction interfaces; surface adsorption; tribochemistry

1 Introduction

Tribology is the science of the interface of surfaces in relative motion, and primarily deals with friction, lubrication, and wear. Friction consumes a large amount of energy, which along with wear-related energy and material losses, costs about 5%–7% of the gross national product in most industrialized nations [1]. Thus, a reduction in friction will benefit the economic well-being of all nations. Although in many cases, such as in brake systems and roads, high friction is required, this review will basically focus on friction reduction (lubrication) of sliding surfaces and antiwear of materials. Lubrication aims to reduce the friction on a surface with a bearing capacity and tangential shear strength, and it has become one of the core techniques for the purpose of reducing carbon emissions and saving energy [2].

Liquid lubrication can be described by the well-known Stribeck curve, as depicted in Fig. 1. The friction coefficient varies with $Z{\cdot}N/P$, where Z is viscosity of the liquid, N is sliding velocity, and P is applied load. In hydrodynamic and elastohydrodynamic lubrication (EHD or EHL) lubrication, the sliding surfaces are completely separated by a continuous film of lubricating fluid. In that scenario, the friction coefficient is directly related to the fluid viscosity. Mixed lubrication occurs when the velocity decreases and the asperities of the rough surfaces start to touch each other. In this case, part of the load is carried by the direct contact between asperities, thus leading to increased friction. Mixed lubrication is a transition regime between boundary lubrication and EHL, and contains characteristics of both of them. Boundary lubrication is a condition in which the lubricant film becomes too thin to support a substantial part of the load, and the asperities come into a sufficiently close contact to cause ''stick-slip'' break-off of some of them. The main task of a tribological study is to reduce the friction coefficient at all lubrication regimes. As it will be seen, the interface interaction between lubrication medium and frictional materials plays an important role in friction reduction. Optimization of the lubrication condition highly depends on the physical and chemical properties of the solid–liquid interface. In the region of boundary lubrication, the friction coefficient becomes significantly large, and thus, it requires an effective

* Corresponding author: Feng ZHOU, E-mail: zhouf@licp.cas.cn

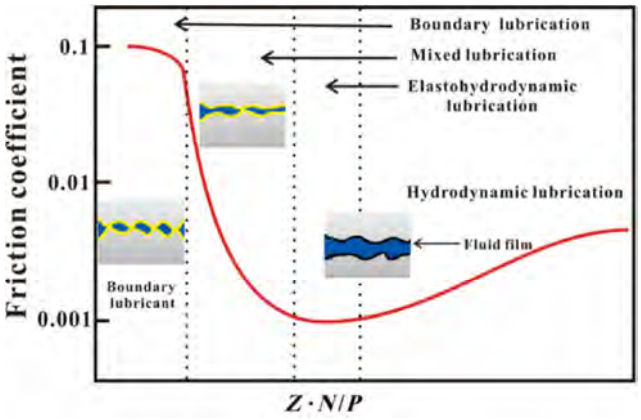

Fig. 1 Stribeck curve during liquid lubrication.

lubrication technology for reducing friction, such as friction modifier, extreme pressure and antiwear agent, and viscosity optimization. The following sections will discuss in detail the research frontier of the boundary and mixed lubrication practice, and their relevant solutions regarding physics, chemistry, and materials.

2 Friction reduction through surface adsorption or surface grafts

In hydrodynamic lubrication, the sliding pairs are separated by a liquid film that is self-generated by the moving surfaces by drawing the lubricant into the wedge, and is formed by the bounding surfaces at a high enough velocity to generate the required pressure to completely separate the surfaces and support the applied load. When the load is further increased or the speed of relative motion is reduced, the fluid thin film cannot be effectively formed to bear a high load, and lubrication will evolve into elastohydrodynamic or boundary lubrication (Fig. 1). This is a condition in which the lubricant film becomes too thin to provide total separation, and where the asperities come into close contact and deform or break-off [3]. It is well known that non-wetting will not benefit friction reduction under enhanced loading, because liquids would be very easily squeezed out of the contact area when load is applied (Fig. 2(a)). Lubricating oils have to wet the surface to form effective lubricating films (Fig. 2(b)). Meanwhile, liquids must have sufficient viscosity to form a hydrodynamic pressure film between the sliding pairs. Therefore, oils (mineral oils, polyolefins, polyether, perfluoro-polyether, polyol esters, etc.) are widely used in practice, because of their relative high viscosity, while water has very low viscosity and can hardly bear high load.

2.1 Base oils from low polarity to high polarity

The above listed oils are widely used in industry. However, their lubricating performance and load-carrying capacities are not satisfactory at severe conditions, such as high loads or low sliding velocities. Besides the improvement of dynamic viscosities of base oils by molecular design, the lubricating and antiwear properties are normally ameliorated by enhancing the surface affinity of lubricants (Fig. 3(a)). Increasing the polarity of mineral oils and polyolefins to polyether and polyol esters lubricants has led to increased load carrying capacity, because the latter oils have stronger interaction with the frictional surfaces. The drawback of a high polarity structure is the easy attack by external triggers (environment, friction practice). Polyethers are prone to degrade and polyol esters are liable to hydrolysis.

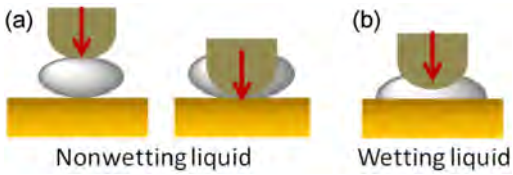

Fig. 2 Stability of liquid upon increasing load. Liquids are prone to be squeezed out of the contact area of sliding, leading to dry friction. Good wetting ability is required to form a stable lubricating film.

Fig. 3 (a) Diagram of lubricating oil interaction with frictional surface: from non/less polarity to high polarity oils. (b) Representative cation and anions that constitute ionic liquids.

A recent successful example in novel high polarity lubricating oils is the design of ionic liquids (ILs) lubricants [4–9]. ILs are ion pairs of cations and anions (Fig. 3(b) shows the structure of imidazolium based ILs), which remain with good mobility even at low temperatures, and maintain stability at high temperatures (some of them have over 350 ˚C decomposition temperature). The high polarity of ILs molecules provides them with high affinity to the friction surface, the main factor leading to good lubricity and load carrying capacity (over 5 GPa vs. ~3 GPa of conventional oils). Forsyth et al. have studied the boundary film generation of various phosphonium ILs on a series of native films on metal and ceramic surfaces using multinuclear solid-state nuclear magnetic resonance (NMR) [10]. The results indicate that SiO_2 and $Mg(OH)_2$ interact strongly with ILs anions and cations, firstly through the adsorption of anions and subsequently by the close proximity of cations in the form of double layers (as observed through ^{1}H–^{29}Si cross-polarization experiments). In contrast, Al_2O_3, MgO, ZnO, and ZrO_2 appear less active owing to less hydroxyl groups on these surfaces. Kajdas developed the anion adsorption model, in which low energy electrons are emitted from contact convex points on the metal surface during friction, leaving a positive charge formed at the surface of the tiny convex volumes, which strengthens the adsorption mode [11]. Clearly, the anions in ILs can be easily adsorbed onto these positively charged sites of a worn metallic surface, and the counter cations are assembled successively by the electroneutrality principle. The dipolar ion structure makes ILs to form an ordered bilayer crystal structure in solid state, in which alkyl chains interdigitated and an extended bilayer with alkyl chains are packed end-to-end. Therefore, it might be true that ILs form ordered adsorption layers on sliding surfaces, most possibly in multilayered fashion, whose structure resembles that of graphite and molybdenum disulfide [7, 12]. This provides good lubricity for ILs under relatively low shear strength. There are thousands of different types of ILs owing to the variable combination of cations and anions. To screen those in which the industry could be interested and that can be used in practice will be a continuous task of future research.

Because 1-hexyl-3-methylimidazolium tris(pentafluoroethyl)trifluorophosphate ([HMIm]FAP) ionic liquid is composed solely of cations and anions, the interface lubricity can be externally controlled *in situ* by application of a potential bias to a highly oriented pyrolytic graphite (HOPG) surface. Atkin et al. revealed that superlubricity can be ''switched'' on and off *in situ* when an ionic liquid is used to lubricate the silica–graphite interface by atomic force microscopy measurements [13]. When the potential is changed, the composition of the interfacial layer responds, which alters the frequency and magnitude of stick slip events, and hence the energy dissipated and friction. At +1.5 V, the anion-rich interfacial layer is ''super-lubricating'' and friction falls to immeasurable values.

2.2 Friction modifier (FM) function owing to interfacial assembly

Another very frequently used way to enhance the lubricity and antiwear of lubricants is the application of FMs (additives) [14]. FMs have polar heads that can interact with the frictional surface. Meanwhile, Van der Waals forces between the molecular tails cause the molecules to align themselves in such a way that they form the absorbed monolayer. If the timescale allows it, all molecules line up, straight, perpendicular to the metal surface, leading to a multilayer formation of the FM molecules (Fig. 4(a)). The FM layers are difficult to compress but very easy to shear at the hydrocarbon tail interfaces, which supports the load-carrying capacity and friction-reducing properties of the FMs, respectively. FMs are usually employed in rather low concentration, but they can significantly enhance the tribological properties of base oils, especially the less polar oils.

Fatty acids have long been used as FMs to reduce friction in mineral oils owing to their high affinity to metal surfaces [15]. Therefore, it is easy to understand that their friction-reduction ability depends on the

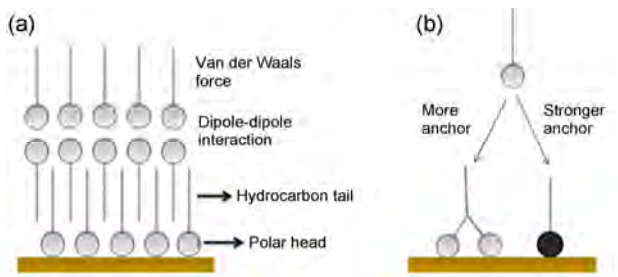

Fig. 4 (a) Interaction of friction reduction additive with frictional surface. (b) Designing novel additives.

type of substrate, because of the differential reactivity of carboxylate with substrates. Besides, their effects will be weakened in polar synthetic fluids such as polyethers and synthetic esters because of the competitive interaction strength. One design criterion is to introduce an additional carboxyl group into the fatty acid to enable divalent interaction, so as to enhance the tribological property (Fig. 4(b)) [16]. Another design approach is to find alternative acting functional groups to replace the carboxylic head (Fig. 4(b)). Fatty acids made a great contribution to lubrication in the early years, since the 1920s, but since the 1950s were gradually overtaken by sulphur/phosphorous containing compounds, which provided greater adsorption strength with a larger variety of metallic materials. Since then, countless studies have been reported in the area. It was many years later, after their application in tribology, that the term "self-assembly" was created (usually, self-assembled monolayers (SAMs)) to elucidate the underlying science [17]. It was revealed that thiols and sulphides could form high quality monolayers on noble metal surfaces, much stronger and faster than fatty acids do on very limited oxides, such as Fe_2O_3 and Al_2O_3, which is the main reason why sulphur-containing additives became popular after fatty acids. A fast and high-quality assembly of the additive on a frictional surface is favorable to heal the surface layer damage under severe sliding conditions.

SAMs have been one of the most important research areas in the past thirty years in surface/material science. The vast amount of research on SAMs should help tribologists to understand the underlying science more clearly, and eventually contribute to a more effective design of new lubricants. Because different head groups have different reactivity with substrate materials, there will be no universal FMs for all materials. Is there any hope to find a modifier that can adhere to all materials? The recently studied mussel-inspired adhesion, based on catecholic chemistry, provides one possibility [18]. However, the self-assembly rate of dopamine at the interface might not match with the frequency of friction. The effective FM might be that in which instantaneous assembly occurs once the absorption layers are sheared off and the assemblies are strong enough to withstand load. Besides additive design, some novel characterization approaches for SAMs should be more extensively used to understand the lubrication mechanisms at molecular level. Work on these aspects will require additional efforts.

Here we would like to mention a novel way of applying FMs by using thermo-reversible (TR) gel lubricants, which consist of a base fluid and gel agent bearing polar groups and alkyl groups [19–24]. TR gel lube includes a high percentage of gelling agent, which is basically an FM that is released when the gel changes to liquid state above the melting point. Thus, they can be easily and strongly absorbed on a metal surface with their own polar group to form a stable film. This absorbed film plays a role as an oiliness agent, and it significantly decreases friction and wear. Substantial work is still required to clarify in detail the mechanism of the TR gel lube and its tribological properties. We also report on a gel lubricant made of ionic liquids (Fig. 5) [25, 26]. The benzotriazole-functionalized imidazolium salt can form a fibrous ordered structure in conventional ionic liquids, and it has been used as lubricant by *in-situ* liquefying. The obtained ionic gels have good anticorrosion ability, conductivity, and thixotropic character, which make them potential anticorrosive solid electrolytes and high performance semisolid lubricants. Especially for some electrical contacts, this ILs gel can be used at low temperatures, and it liquefies upon mechanical shearing with low friction and good antiwear properties. This application prompted us to develop a gel lubrication system by designing low molecular weight gelators (LMWGs) to gelate various lubricant oil [21–24]. We have designed and prepared a class of LMWGs, which can form random three-dimensional networks and cavities, in which liquid lubricants (such as water, mineral oil, and synthetic lubricating oil) are trapped through H-bonding, π−π stacking, hydrophobic interaction, van der Waals force, London dispersion forces, and electrostatic interaction. The

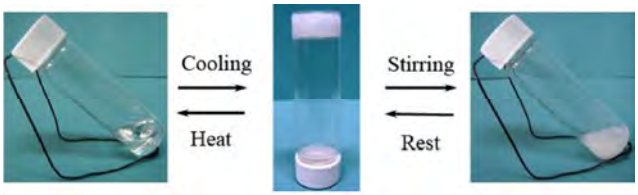

Fig. 5 A gel lubricant that reversibly changes its physical states.

as-prepared gels have good thermoreversible and thixotropic characteristics. This makes that gel lubricants have important implications in lubrication, in which solid-like lubricants are liquefied under high shear strength (high load and lateral shear) and high temperature, and take part in lubrication like oils. The experimental results show that these gel lubricants not only can effectively avoid the lubrication-oil creeping and evaporating loss, which benefits maintenance, but also have better lubricating and antiwear performances than the blank base lubricating liquid and grease. For some special contacts, the gelated base oil can be used to solve problems of base oil creeping and evaporating loss, and thus to enhance maintenance and operation.

2.3 Improved aqueous lubrication by amphiphilic surfactant adsorption

Different from the wide application of oil lubrication in industry, aqueous lubrication is used in relatively limited areas, such as metal working processes, bearings in marine industries, and biological systems. Water has limited boundary lubricating capability (load carrying capacity) owing to its low viscosity and viscous pressure coefficient. One main task of aqueous lubrication is to improve the viscosity of aqueous liquids. For example, it has been recently reported that a large-molecular-weight polyanion, sodium poly(7-oxanorbornene-2-carboxylate), can be a high performance synthetic water lubricant for biolubrication because it can significantly improve the rheological property of water [27].

Aside from the viscosity concerns, friction in aqueous media can be similarly reduced through the adsorption of amphiphilic surfactants onto substrates. Briscoe et al. found that the frictional stress between sliding surfaces coated with amphiphilic surfactant layers (N,N-dimethyl-N,N-diundecyl ammonium bromide) immersed in water could be reduced by 1–2 orders of magnitude or more, relative to its value in dry air, although the adhesion hysteresis is comparable in both cases [28]. The surfactant head groups at the substrate surface become hydrated under water and as a result, the slip plane between the sliding surfaces shifts from the alkyl tails/alkyl tails interface in air or oil environment, to the head group/substrate interface in water. The high fluidity of the hydration sheath around the head groups results in greatly reduced friction. Sliding is much easier as a result of the hydration-lubrication mechanism of the hydrated head groups.

Lipids are another type of amphiphilic molecules in biological environments and exist mostly in form of liposomes. Goldberg et al. coated mica with small (approx. diameter 70 nm) unilamellar (single bilayer wall) vesicles of hydrogenated soy phosphatidyl choline (HSPC, structure shown in Figs. 6(a)–6(c)), and investigated the friction acting between two such liposome-coated surfaces by surface force balance (SFB) [29]. The lipsomes may form close-packed boundary layers on surfaces under water, which could lead to a striking reduction in the sliding friction, with the friction coefficients down to 2×10^{-5} at pressures up to more than 100 atm (Fig. 6(d)). This is attributed to hydration-lubrication by the highly-hydrated phosphocholine groups, which exposed at the surface of the liposomes rub against each other, together with the very robust nature of the adsorbed layers of vesicles. This is due to the closed structure, uniformity, and close packing of the liposomes on the surface, and particularly their rigidity by virtue of being in the gel phase, which enhances their load-carrying capacity. The extreme boundary lubricating properties of liposomes arising from the hydration lubrication mechanism thus offers great promise for medical and biomedical applications where friction is an issue, including osteoarthritis, contact lenses, or knee- or hip-joint implants [30].

2.4 Improved aqueous lubrication by brush-like macromolecules

Polymers cannot only increase viscosity, but have potential to form boundary adsorption, and thus are an important choice for water lubricants. They are largely inspired by lubrication in nature. The friction coefficient of articular cartilage can be as low as 0.001, and it takes advantage of water lubrication through brush-like glycoproteins grafted on the surface or in bulk, which retain water molecules to generate repulsive hydration forces at the interface of the sliding surfaces (Figs. 7(a) and 7(b)) [31–33]. The presence of hydrated glycoprotein at the friction surface simply increases the interface viscosity of water and makes it

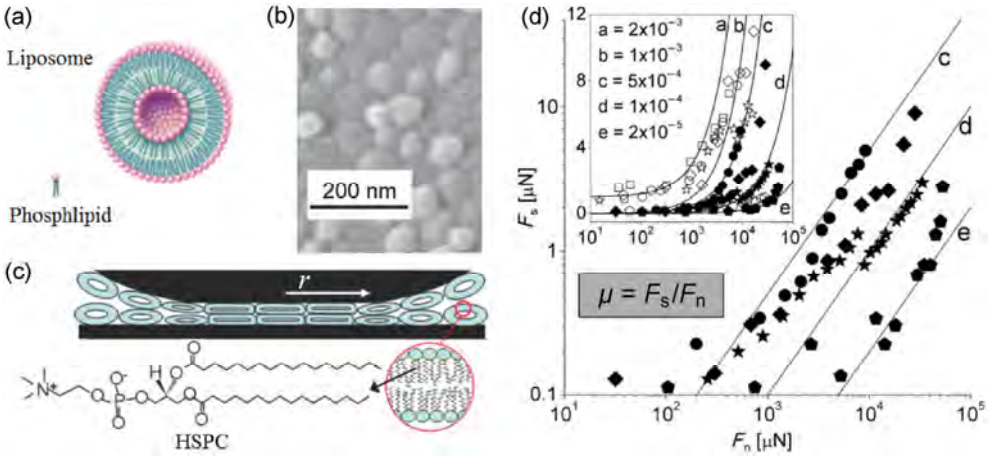

Fig. 6 (a) Liposome, (b) cryo-SEM image of the HSPC-SUV adsorbed on freshly cleaved mica, (c) scheme of HSPC-SUV self-assemble in close-packed layers on mica surfaces, and (d) friction forces F_s versus applied loads F_n between two HSPC-SUV-coated mica surfaces (as in Fig. 6(c)). The inset shows the F_s versus F_n variation on a first approach (empty symbols), and on second or subsequent approaches (correspondingly filed symbols). Curves a–e show the variation $F_s = \mu F_n$, with friction coefficient μ values as indicated in the inset [29, 30].

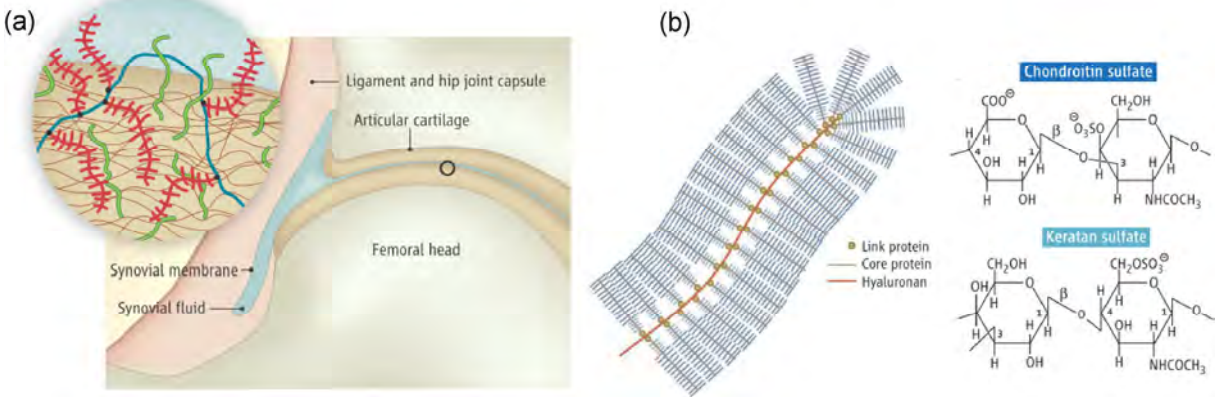

Fig. 7 (a) The close-up view of the articular cartilage surface. (Inset) The detailed structure at the outer cartilage surface is thought to include charged macro-molecules, mainly hyaluronic acid (blue), to which are attached aggrecans (red) and lubricins (green) that extend from the surface to form a brush-like layer [33]. (b) Illustration of the bottle-brushes structure of aggrecans [32].

a good lubricant. In a good solvent, the high polymer grafting density forces the polymer chain to stretch away from the surface to avoid overlap of the molecular chain [18]. When the counter sliding pair approaches and presses the polymer chains, the crowded polymer chains will produce a very large osmotic pressure that generates a direction opposite to the applied load through osmolality exclusion. Macromolecular brushes form a hydration layer that is easy to flow, leading to ultra-low friction.

However, whether a hydrophilic polymer can result in ultralow friction depends on its capability to form an effective boundary layer. For a rational polymer design, the polymer structures listed in Fig. 8 are highly desirable. They are either diblock polymers, or end functionalized polymers, or combing polymers with anchoring groups, wherein one compartment

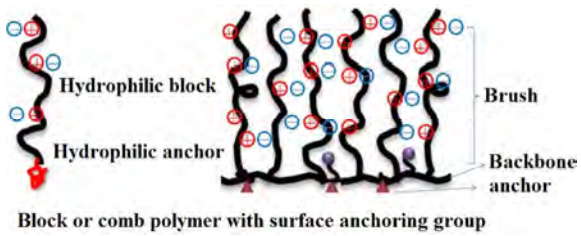

Fig. 8 Structures of hydrophilic polymers with surface anchoring groups.

forms strong interaction with the frictional surface and the other hydrophilic part forms a hydration layer. Klein et al. reported on the water lubrication behavior of the poly(methylmethacrylate)-block-poly (sodium sulphonated glycidyl methacrylate) copolymer (PMMA-b-PSGMA) on the hydrophobic surface of mica. PMMA segments have strong hydrophobic interaction with the mica surface, which is able to anchor in-situ the anionic PSGMA onto the frictional surface, with polymer chains stretching outwards to form a "brush" type structure [31]. Figure 9 shows that the polymer surfactants lead to very low effective friction coefficients, whereas the neutral brushes and the adsorbed charged chains (coloured symbols and bands) show a rapid increase in friction coefficients at higher volume fractions. Friction mediated by PSGMA brushes (black symbols and grey band) remains extremely low, up to the point where the volume fraction is close to unity. This is attributed to the exceptional resistance to mutual interpenetration displayed by the compressed, counterion-swollen brushes, together with the fluidity of the hydration layers surrounding the charged, rubbing polymer segments. Spencer et al. studied the tribological properties of the positively charged lysine as main chain, hydrophilic polyethylene glycol as side chain, and "bottle brush" type polymer (PLL-g-PEG) as a water-lubricated additive [34, 35]. The polypeptide backbone with a positive charge can be anchored to the negative

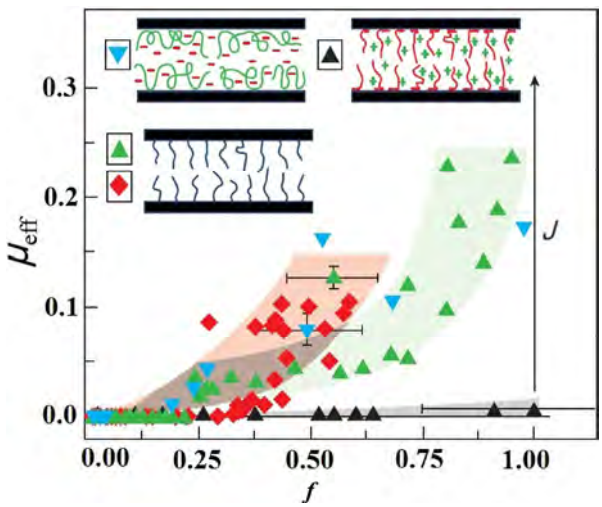

Fig. 9 Variation of the effective friction coefficient μ with volume fraction f of confined polymer for different polymer lubricants [31].

charge of the metal and the oxide surface by electrostatic interaction. The PEG chain extending outwards forms a "brush"-type structure, and it is combined with a large number of water molecules, which play a very good boundary lubrication effect through an increase in the chain length of the side chain PEG segment, to obtain a lower friction coefficient. They also studied the self-healing effect of the water-soluble polymer additives in the process of friction. When the boundary lubrication layer is damaged because of wear, the bulk polymer in the solution is able to repair the wear surface quickly through electrostatic interactions, which maintains the friction coefficient low.

2.5 Improved aqueous lubrication by surface grafted polymer brushes

Surface-initiated polymerization from a surface bound initiator monolayer offers the easiest way to prepare surface-grafted polymer brushes in high density, and it can be used for aqueous lubrication. Spencer et al. have used a photoinduced "grafting from" approach to grow polymethacrylic acid (PMAA) brushes on Si/SiO_2 surfaces, and investigated the lubrication properties of the PMAA brushes of different molecular weights and soft, hydrophilic ox-PDMS pins in macroscopic tribological experiments under low-contact-pressure, aqueous conditions [36]. The results showed that the PMAA brushes could not be distinguished from the μ vs. sliding speed plots, and long-term stability of the short 15 nm PMAA brushes showed to be inferior to that of long brushes (240 nm dry thickness). PMAA brushes display significantly lower friction than PEG monolayers under aqueous lubrication conditions. This is mainly due to the higher grafting densities of the PMAA compared to PEG layers, enhanced swelling of the polyelectrolyte brushes in neutral aqueous media, and additional electrostatic repulsion against the oxidized PDMS slider. Klein et al. used a surface force apparatus to study the behavior of water-lubricated mica surfaces with grafted polymer PMPC brushes, and found that the surfaces can have μ values as low as 0.0004 at pressures as high as 7.5 MPa (Fig. 10) [37]. The primary mechanism underlying the low friction was attributed to the side-chain phosphorylcholine group, capable of binding a large number of water molecules and

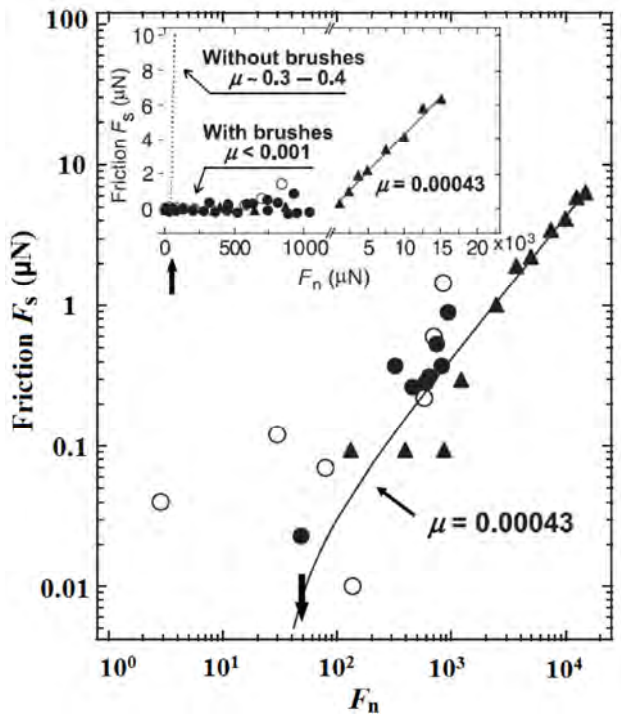

Fig. 10 Variation of friction F_s with load F_n and with sliding velocity, and vs. PMPC brush–coated surfaces [37].

allowing easy flow of the hydration layer. The flexibility of the hydration layer can withstand high loads and maintain a very low friction coefficient.

Friction and wear are often an issue in human-made systems. These results may have relevance for boundary lubrication in human-made systems, and they reveal potential in aqueous or physiological media, especially for biomedical devices.

The interactions between the responsive polymer brushes are strongly dependent on the conformation of the brush, which can be finely controlled. The change in conformation of polyelectrolyte brushes can be translated into friction control [38]. Rutland and Nordgren investigated the stimuli-induced lubrication behavior between poly(2-(dimethylamino)ethyl methacrylate) (PDMAEMA) grafts on gold under different pH and temperature environments with colloidal probe atomic force microscopy, and found out friction response to pH and temperature [39]. The effects of these two parameters on the brush collapse are subtly different, because pH affects primarily the charging of the amine moieties, whereas temperature controls the strength of the hydrophobic interactions between the polymer chains and the solvent. At low pH, the brush with low friction was attributed to the formation of a repulsive, highly charged, hydrated cushion. At high pH, the friction was significantly increased. The system turned attractive above the lower critical solution temperature, with a small friction reduction interpreted as being due to nanoscopic flattening at the interfacial boundary.

Despite several works being conducted on tuning friction of polyelectrolyte, the types of counterions and the magnitude of friction change are still very limited. We systematically present feasible surfaces for dramatically tuning macroscale friction from superior lubrication (μ ~10^{-3}) to ultrahigh friction (μ > 1) via exchanging counterions into polyelectrolyte brushes when the surface is sliding against a silicone elastomer ball [38]. The tunable friction is based on counterion-driven interactions in polyelectrolyte brushes that can be simply achieved by exchanging the counterions. The effects of opposite counterions of different types on the friction properties of polyanionic, polycationic, and polyzwitterionic brushes were systematically investigated. Figure 11(b) showed that the friction coefficient of cationic brushes with quaternary ammonium groups was progressively tuned from ~ 10^{-3} to ~ 10^{0} according to the counterions series Cl^- < ClO_4^- < PF_6^- < $TFSI^-$. The friction of anionic brushes can be tuned by oppositely charged surfactants (tetraalkylammonium) with different length of hydrophobic tails, multivalent metal ions, and protons. The friction increase of cationic brushes is due to the dehydration and the collapse of polyelectrolyte chains induced by ion-pairing interactions. For anionic brushes, the friction increased with the length of hydrophobic tails of surfactants, which resulted from hydrophobicity-induced electrostatic interaction among the surfactants and polymer chains (Fig. 11(c)). The anionic brushes with the carboxylate and the sulfonate side groups revealed different friction responses, which is due to the carboxylate groups getting a stronger specific interaction with the quaternary ammonium, and thus, with the multivalent metal ions. The mechanism of tuning friction was finally concluded; that is, highly hydrated and swelling polymer brushes show superior lubrication, partially collapsed polymer chains have moderate lubrication, while the completely dehydrated

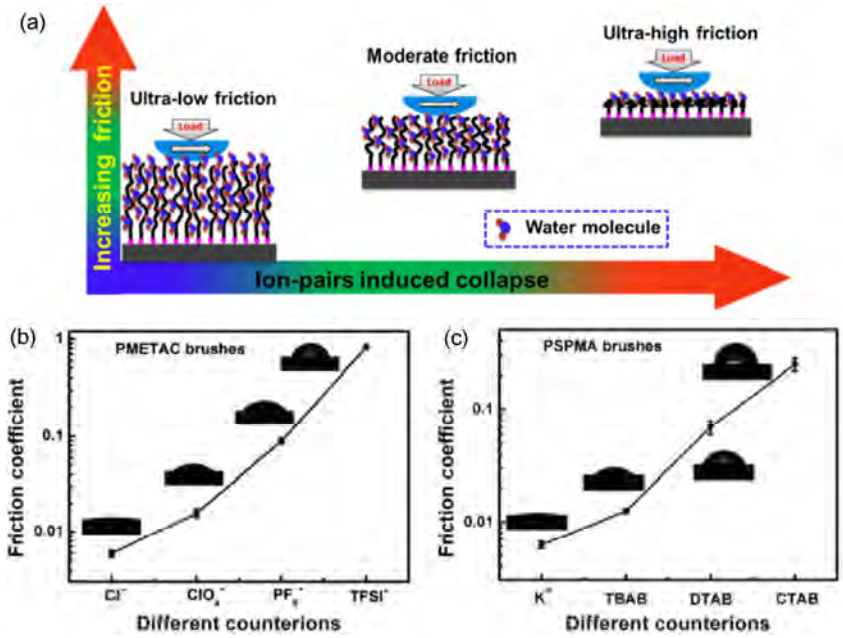

Fig. 11 (a) Illustration of correlation between lubrication and conformation of polymer brushes, changes in friction coefficients and wettability (inserted images) corresponding to (b) and (c). (b) PMETAC brush on Si substrates when the counterions are Cl^-, ClO_4^-, PF_6^-, and $TFSI^-$. (c) Polyanionic brushes on Si substrates; the counterions are cationic surfactants (TBAB, DTAB, and CTAB) for PSPMA brushes [38].

and collapsed conformation loses lubricating capability (Fig. 11(a)). The tunable lubrication platform would be helpful to further understand the lubricating mechanism of polymer brushes and would promote applications of these smart surfaces in micro fluidic devices, biosensors, and so on.

Recently, our group found that the weak interaction between polymers and surfactants played an important role in the lubrication behavior and wettability of polymer brushes, which depended on the surfactant concentration [40]. Taking cationic (PMETAC) and anionic (PSPMA) brushes as examples, with the addition of surfactant above the critical micelle concentration (CMC), the weak interaction achieved a gradual transition from ultralow friction to ultrahigh friction, because the surfactant exchange led to a strong dehydration of the brush. When the addition of surfactant was above the CMC, a reduction in friction for the anionic brushes was observed, owing to the lubricating effect of micelles, while the cationic brushes maintain a high friction, without this micelle lubricating effect. These results reveal the relation between surfactant adsorption and lubrication behavior.

2.6 Improved wear resistant by surface grafted polymer brushes

Migration of the artificial femoral head to the inside of the pelvis caused by the degeneration of the acetabular cartilage has emerged as a serious issue in resurfacing or bipolar hemi-arthroplasty [41]. Surface modification of the cobalt–chromium–molybdenum alloy (Co–Cr–Mo) is one of the promising means of improving lubrication for preventing the migration of the artificial femoral head. Ishihara et al. systematically investigated the surface properties of the various surface modification layers formed on the Co–Cr–Mo surface by the MPC polymer by dip coating or photo-induced radical grafting. The results showed that the cartilage/poly(MPC) (PMPC)-grafted Co–Cr–Mo interface mimicked a natural joint, with an extremely low friction coefficient of <0.01, as low as that of a natural cartilage interface. Moreover, in the PMPC-grafted layer no hydrolysis of the siloxane bond was observed throughout soaking in phosphate-buffered saline for 12 weeks, and it showed a long-term stability in water. These results illustrated that

cartilage/poly(MPC) (PMPC)-grafted Co–Cr–Mo interface prevented degeneration of the articular cartilage. Current artificial joints with polyethylene (PE) surfaces have considerably less efficient lubrication and thus much greater wear, leading to osteolysis and aseptic loosening. Then, they reported the development of nanometer-scale hydrophilic layers with varying charge (nonionic, cationic, anionic, or zwitterionic) on cross-linked PE (CLPE) surfaces, which could fully mimic the hydrophilicity and lubricity of the natural joint surface [42]. The POEGMA- and PMPC-grafted CLPE cups exhibited high wear resistance in the hip simulator tests along with low coefficients of dynamic friction in the ball-on-plate friction tests. The primary mechanism underlying the low friction and high wear resistance must be attributed to the high level of hydration of the grafted layer, where water molecules act as very efficient lubricants. The secondary mechanism is repulsion of protein molecules and positively charged inorganic ions by the grafted polyelectrolyte layer.

Many excellent theoretical and computer simulation studies have been performed to elucidate the mechanism responsible for low friction between polymer brushes. However, to extend these insights to sliding layers is a challenge. Goujon et al. have calculated the kinetic friction coefficient of neutral and charged polymer brushes with the same grafting density at different compression ratios, in an effort to model SFB experiments in these systems using dissipative particle dynamics (DPD). They found that the kinetic friction coefficient between the charged brushes is higher than that of neutral brushes at low compressions and smaller at high compressions, although the differences remain small. They also showed that it is possible to simulate ultra-low friction coefficients, comparable with experiments, using the smallest shear rate accessible in a mesoscale simulation. The polyelectrolyte brushes can support a higher load due to the presence of free counterions within the brush. The viscosity in the polymer free gap is smaller in charged brushes than in neutral brushes, indicating that the solvent particles in this region assist the sliding of the two interacting charged brushes. The unexpected behavior of the shear deformation-induced structural heterogeneities in charged polymer brushes calls for further experiments to elucidate this local reorganization of the ions in adsorbed charged polymers.

The surface graft polymer brushes have a low coefficient of friction in a water environment, but are usually worn out within 50–100 cycles of macroscopic reciprocating friction by the sliding probe under a high normal load of around 100 MPa, resulting in a high friction coefficient owing to the exposure of the bare substrate. Thus, the wear resistance for the application of a polymer brush is not sufficient for its practical use under load bearing conditions. However, it is not difficult to solve this issue, because the polymer brushes composition and structure can be flexibly designed by researchers. Takahara et al. reported that partially cross-linked ion-containing polymer brushes were effective for the improvement of wear resistance without loss of good lubrication. They prepared copolymer brushes of 2-dimethylaminoethyl methacrylate (DMAEMA), 2-(methacryloyloxy)ethyl phosphorylcholine (MPC), 2-(methacryloyloxy)ethyl trimethylammonium chloride) (METAC), and 3-sulfopropyl methacrylate potassium salt (SPMK) with excellent waterwettability [43]. Among them, the poly(SPMK) revealed an extremely low friction coefficient of around 0.01, even after 450 friction cycles. Furthermore, the poly(SPMK-co-METAC) brush with electrostatically cross-linked structure showed an extremely low friction coefficient in water, even after 1,400 friction cycles under a pressure of 139 MPa. The cross-linking structure improved the shear strength of the polymer brush thin films, thus preventing wear of the brush, and maintaining hydrophilicity to assist water lubrication.

From the above, lowering friction can be basically achieved by interface adsorption of small molecules in oil lubrication, so that viscous shearing can be transformed to shearing between an ordered molecular assembly or by adsorption of hydrated molecules to generate hydration lubrication in water environment. A comparison of research on aqueous and oil lubrication would be of benefit to both. One question is whether it is possible to achieve ultralow friction in an oil lubricating system, and how. How can stable ultralow friction be achieved under most engineering conditions, e.g., high loads, engineering surfaces rather than atomic flat surfaces, and conformal surfaces?

3 Friction reduction and antiwear based on tribochemistry

In mixed and boundary lubrication, surface asperities come to contact, deform, and break down, as seen in Fig. 12(a). Complex tribophysicochemical processes occur, which include local temperature increase, wear of local asperity to generate a fresh nascent surface, and triboemission (electrons, ions, photons, etc.). Boundary adsorption films can prevent direct contact of asperities (Fig. 12(b)). Flash temperature is generated at contacted asperities, and it is usually short lived. If the heat cannot be dissipated in time, it would lead to increased temperature that exposes lubricant molecules to thermal stress and speeds up a tribochemical reaction. As shown in Fig. 12(c), when asperities are worn off, a nascent surface is generated with dangling bonds, and it is far more reactive than the native surface to activated reactions [44]. Another tribophysical process is the triboemission, the emission of electrons, ions, photons, UV radiation, IR radiation, and acoustic emission, as a response to friction and wear processes [45]. The spontaneous emission of low-energy electrons (exoelectrons) from solid surfaces comes from plastic deformation, abrasion, fatigue cracking, or phase transformation. The positive charges or electron vacancies left on the frictional surface, though having only a minute life time, are sufficient to initiate chemical reactions with molecules of the environment. Triboplasma (Fig. 13) may be generated by discharges in the surrounding gas owing to triboelectrification [46–48]. In the vicinity of the sliding contact reactions, it can cause tribochemical reactions [47, 49].

3.1 Tribochemical reactions

Tribochemistry generally refers to the chemical reactions that occur between the lubricant and the rubbing surfaces under boundary lubrication conditions [51]. It may have harmful effects by accelerating the decomposition of lubricants or have beneficial effects by forming friction and wear reduction organic films. The protective films are usually formed at much lower temperatures than those at which lubricants normally show chemical activity, indicating a catalytic reaction by friction. Tribochemistry is a complex process, which is very difficult to fully understand, and could not always be explained with the traditional static reaction mechanisms of thermal and catalytic reactions, but also must be governed by those chemical reactions under the dynamic triboprocess. For example, zinc dialkyl dithiophosphates (ZDDPs), as very effective comprehensive additive in versatile base oils, have been used for dozens of years. However, the underlying mechanisms have not been fully disclosed so far, and thus, it is still a key topic. Beyond surface adsorption, tribochemical reaction is the main functioning way of friction reduction and antiwear additives.

Fig. 12 The contact complications in mixed and boundary lubrication

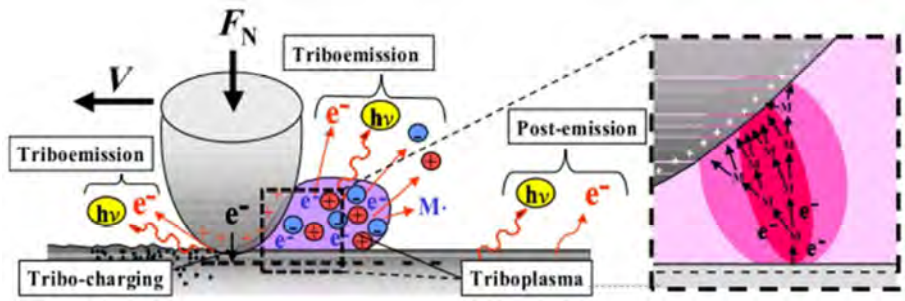

Fig. 13 Model of triboplasma generation through discharging of gas owing to triboelectrification [46, 47, 50].

3.2 DDPs based additives

ZDDP reacts with asperities to reduce the contact and when the load is high enough to collapse the oil film, it reacts with the entire metal surface to prevent welding and to reduce wear [51]. Most of the attention in recent years has been focused on the ability of ZDDP to form tribofilms on rubbing iron and steel surfaces under mild wear conditions and, in particular, on the chemical composition and properties of these films. They consist primarily of closely packed pads of glassy, zinc or tho- and pyrophosphate, typically 5 μm across and 100 nm thick [52]. The outermost layers of these pads contain a longer chain zinc polyphosphate. The lower layers next to the surface contain some iron cations in place of zinc. Between the pads there are fissures containing a bulk solution. Under more severe conditions, they also act as an extreme pressure additive to form metal sulphides and the phosphate glass to prevent cold welding. Mosey carried out a computer simulation of zinc dialkyl dithiophosphates under extreme conditions and concluded that pressure-induced cross-linking is a key mechanism in the formation and functionality of antiwear films [53]. Recently, Gosvami et al. monitored *in-situ* the growth and properties of the tribofilms in well-defined single-asperity sliding nanocontacts [54]. They found that the growth of ZDDP antiwear tribofilm increases exponentially with the applied pressure and temperature. This result is consistent with the stress-assisted reaction rate theory. The research provides a new way to study tribochemical phenomena and functionality at the molecular scale.

Following the application of ZDDPs, many analogue compounds have been developed. Among these compounds, molybdenum dithiophosphates (MoDTP) and molybdenum dithiocarbamate (MoDTC) have been extensively studied. Grossiord et al. have investigated the mechanisms of MoDTC for reducing friction under boundary lubrication using analytical tribometry [56]. The C-based tribofilm contains a few percent of highly dispersed MoS_2 in the form of individual sheets of length less than 10 nm. A mechanism of the breakdown of the MoDTC molecule from a chemical point of view was proposed, as shown in Fig. 14 [55, 56]. The initial step towards MoS_2 formation is via electron

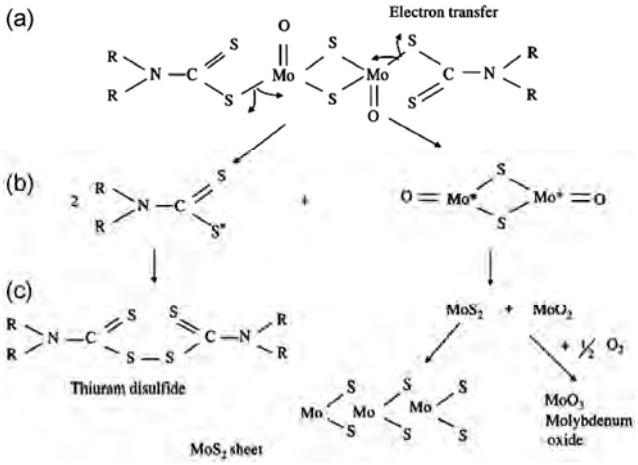

Fig. 14 Molybdenum dialkyl dithiocarbamate (MoDTC) decomposition chemical model [55, 56].

transfer at the Mo-S chemical bonding MoDTC (Fig. 14(a)), leading to the formation of three free radicals (Fig. 14(b)): two at the core of MoDTC and the other one at the chain end. The third step is core radical decomposition (Fig. 14(c)) into MoS_2 and MoO_2, which can be further oxidised, and the recombination of chain end radicals forming thiuram disulphides. The layer-lattice structure of the molybdenum disulphide makes it possible to achieve low friction. The thiuram disulphides form the interlayer, having weak van der Waals force, and is easy to shear resulting in a low coefficient of friction. Besides, the organic molybdenum additives (DDP based and DTC based) contain several polar atoms such as S, P, and N. These strong activity components can react with the substrate materials, such as steel, to form boundary friction reduction and antiwear films consisting of MoS_2, $FePO_4$, FeS, and FeO, which can prevent the substrate from cold welding. The effectiveness of MoDTC in reducing friction is strongly affected by synergistic or antagonistic effects with other additives [52, 53], especially ZDDP. When ZDDP is used with MoDTC, it helps to produce MoS_2 and benefits the lubrication performance.

With the growth in awareness of the environmental crisis, the pollution problem from lubricating oils is receiving increased attention. The possible solutions are to use environmentally friendly lubricants and additives. Therefore, there has been an increasing demand for developing environmentally friendly lubricants and additives with low-sulfur and low-

phosphorus have been of great interest in tribochemical research in the past decade. Novel zinc-free compounds, alkyl borate-dithiophosphates, with a low content of sulphur and phosphorus, are designed as additives for lubricants [57]. Their interfacial performance in steel-to-steel contacts in a mineral oil was studied in terms of friction and antiwear characteristics. This class combines two high-iron-affinity surface active groups, borate and dialkyl dithiophosphate, into a single molecule. The results show that alkyl borate-dithiophosphates, with substantially reduced amounts of sulphur and phosphorus compared with Zn-Bu DTP, have considerably better antiwear and friction performance. This is mainly because tribofilms, formed on the steel surfaces when the novel additives are admixed in the mineral oil, enhance steel-to-steel contact performance. Metal-, sulphur-, and phosphorous-free additives will be a long-term task.

3.3 Ionic liquids additives

For the above mentioned target, ILs represent a good choice to be considered. As mentioned before, ionic liquids, as the base oils, exhibit excellent tribological behavior from fluid lubrication to boundary lubrication [4, 58, 59]. Except for the polarity-induced surface absorption, under harsh sliding conditions, the active elements [N, F, P(B)] in ionic liquids offer sufficiently rich tribochemistry to form extreme pressure films of lower shearing strength by reacting with the fresh surface, which leads to lower friction coefficient and good wear resistance. It was found that ionic liquids as the additives in base oils also perform very well [60–75]. The tribochemical reactions of ILs have been extensively studied. Qu et al. [9] have characterized the boundary lubricating film formation of an ionic liquid (IL) trihexyltetradecylphosphoniumbis(2-ethylhexyl) phosphate as potential antiwear lubricant additive in polyalphaolefin oil. Figure 15(a) shows a cross-section of the near surface region underneath the wear scar lubricated by PAO+IL(5%). It clearly shows a two-layer structure including a top tribo-boundary film (120–180 nm) and a subsurface plastic deformation zone (0.5–0.8 μm) with a refined grain structure. This protective boundary film is responsible for the antiscuffing/antiwear functionality. The

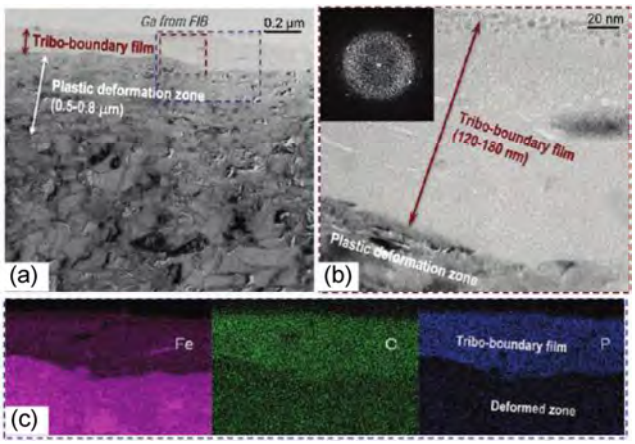

Fig. 15 TEM imaging and occurred EDS element mapping on the cross-section of the near surface zone of a cast iron worn surface lubricated by PAO+IL(5%). (b) and (c) correspond to the red dashed line box and blue dotted line box marked on (a), respectively [9].

higher-magnification image of the boundary film in Fig. 15(b) (corresponding to the red dashed box in Fig. 15(a)) reveals an amorphous matrix embedded with fine nanoparticles (1–10 nm in diameter), and the electron diffraction pattern (insert in Fig. 15(b)) confirms the nanocomposite phase structure. The EDS element mapping in Fig. 15(c) (corresponding to the blue dashed box in Fig. 15(a)) shows high concentrations of P, O, and Fe in the boundary film, because of interactions/reactions between the IL and the metal surface.

Despite of their exceptional tribological property, the thermo-oxidative stability is a more useful parameter of ILs for practical applications. When the imidazolium-based and ammonium-based ILs are kept at 200 °C for 1,000 h, the color of the samples will turn to black after long time thermal stress, probably owing to the Hofmann elimination reactions [76, 77]. Corrosion of ILs is primarily the result of the hydrolysis of perfluoro-anions such as BF_4^- and PF_6^-, or from impurities like halogens introduced during synthesis [58, 78]. Thus, thermal oxidization and corrosion are two problems of ILs lubricants in real applications. An effective way to enhance the anticorrosive and antioxidative properties of ILs is to introduce functional groups. As shown in Figs. 16(a)–16(c), by incorporating benzotriazole and sterically hindered phenol, or both, into imidazolium, the anticorrosion and antioxidation properties could be considerably enhanced when

these compounds were used as the anti-wear (AW) additives in polyether [79–81]. The molecular design is to introduce more tribochemical reactions that can inhibit oxidation and corrosion for better protection of base oils. It has been recently found that ionic liquids could be formed in base liquid *in-situ* by blending TFSILi with polyether and polyol ester [82–85]. Lithium bis(trifluoromethylsulfonyl)imide (LiTFSI) can form ILs with synthetic esters, [Li(synthetic ester)]TFSI, by the donation of lone pairs on carbonyl oxygen atoms of an ester molecule to a lithium ion to form a weakly Lewis-acidic complex cation $[Li(synthetic\ ester)]^+$ and the following interaction with the weakly Lewis-basic anion $TFSI^-$ to generate [Li(synthetic ester)]TFSI. LiTFSI interacts with polyether in a very similar way. The easy preparation, extremely good solubility, and excellent tribological properties of the *in-situ* formed ILs provide them with great advantages when compared with conventional ILs, which can hardly be used as lubricant additives in synthetic esters owing to their low solubility (Fig. 16(d)).

Both DDP type of additives, ILs, and many others have multiple active elements in molecules, which allows a rich tribochemical reaction to occur during friction. The tribochemical reaction products prevent direct contact between the sliding pairs, which is the basis of friction reduction and antiwear. The S, P, N, and F elements are mostly seen in these additives. There are strong demands to reduce their content owing to the increased environmental pressure. Therefore, one critical topic is whether we can find alternatives that are environmentally friendly, while maintaining enough reaction activities to form boundary protecting films through triboreaction. Potential solutions include (1) designing B, N based additives; (2) developing inorganic additives, as will be reviewed later; and (3) developing oiliness lubrication techniques.

3.4 Superlubricity owing to tribochemistry

The state in which friction between two solids is zero and the solids slide without resistance to motion is called "superlubricity" [87]. Because of the limits in measurement precision, in practical terms, the lubrication state can be considered as superlubricity when the friction coefficient is lower than 0.01 in a sliding system [1]. At present, superlubricity materials include solid lubricants (diamond like carbon (DLC), molybdenum disulfide (MoS_2), etc.) [88–90] and liquid lubricants [91–97]. The solid lubricants have been studied in detail by molecular dynamics simulations and experimental investigations. However, the investigation on liquid lubricants for superlubricity is still at the early stage. Li et al. found the novel superlubricity phenomenon of phosphoric acid (H_3PO_4) under ambient conditions [91, 98]. An ultralow friction coefficient of about 0.004 between glass/Si_3N_4 and sapphire/sapphire tribopairs was obtained under the lubrication of a phosphoric acid aqueous solution (pH 1.5) at high contact pressure (the maximum pressure can reach about 1.65 GPa), after a running-in period of about 600 s. The tribological results showed that the whole friction process could be divided into three stages according to the evolution of friction coefficient with time. The first stage, from 0 s to 160 s, corresponded to the process of friction rapidly decreasing. In this first stage, the mechanical action between the two surfaces plays the dominant role instead of the chemical reaction. A severe wear occurred on the friction surfaces, and as a result, the contact area increased rapidly and the contact pressure was

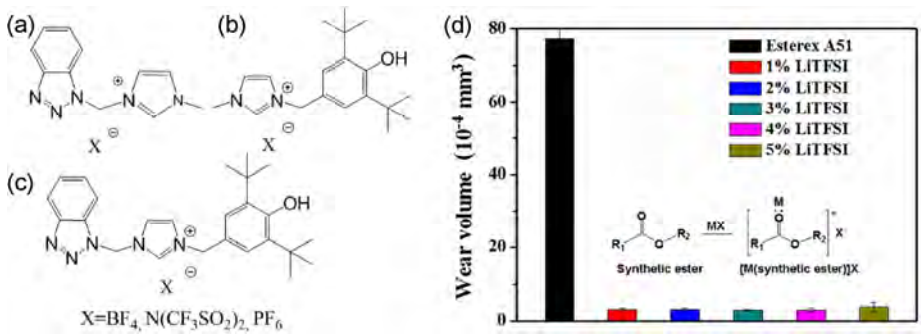

Fig. 16 Functionalized ionic liquids [79–81], and *in-situ* formed ionic liquids as the additive [86].

reduced consequently. In addition, the tribochemical reaction between hydrogen ions and friction surfaces occurred in the contact region ($SiOH + H^+ = SiOH_2^+$) during the first stage, which would make the surfaces to become positively charged. The surface charge can produce the stern layer, and the electrical double layer reduces their friction coefficient. The second stage, from 160 s to 520 s, was a slowly friction-reducing process. In this stage, no wear is occurring but the volume of solution is reduced to a limited amount to form the starvation state, and a hydrogen bond network among (H_3PO_4, $H_2PO_4^+$, and H_2O) is formed in the confined solution. The third stage, from 520 s to the end of the test, was the superlubricity process. In this stage, the superlubricity would keep constant if a thin film with hydrogen bond network among H_3PO_4, $H_2PO_4^+$, and H_2O is adsorbed on the track to bear the load. Therefore, the superlubricity mechanism of phosphoric acid is attributed to the hydrogen bond network between the phosphoric acid and water molecules formed on the stern layer that is induced by the attached hydrogen ions [91, 92, 98, 99].

Except the experimental investigations, reactive molecular dynamics simulations are conducted to investigate the superlubricity mechanism induced by tribochemical reactions in the silica/phosphoric acid system [100]. The friction coefficient is found to have strong positive correlation with the number of interfacial hydrogen bonds, which suggests that a weaker interfacial hydrogen bond network would favor a lower friction. The sliding friction behaviors and tribochemistry of phosphoric acid under solid confinement and shear have a strong temperature dependence in a wide temperature range. The friction reduction mechanisms have been analyzed in two temperature regimes. For $300 \le T \le 600$ K, no indication of tribochemical reaction is observed, and the friction coefficient decreases because of the accelerated molecular rotational and translational motion and the corresponding weakened hydrogen bond network. For $800 \text{ K} \le T \le 1{,}400$ K, the occurrence of tribochemical reactions leads to a clustering and polymerization of the phosphoric acid molecules and generation of a considerable quantity of water molecules, and formation of slip planes is also enhanced by the increasing temperature. It was observed the generation of water molecules and their accumulation at the sliding interface, which could lead to an even weaker interfacial hydrogen bond interaction, owing to the much faster dynamics of water molecules. Hence, it shows good lubricating properties with a friction coefficient as low as 0.02.

In 2008, Matta et al. observed a new superlubricity macrosystem of pure glycerol [1]. They found that the use of steel surfaces and/or ta-C coated surfaces, lubricated by selected polyhydric alcohol molecules, could give unsurpassed low friction values, below 0.01. This was attributed to the existence of a network of H-bond interactions in the confined interface zone. In addition to the formation of OH-terminated surfaces but at a lower temperature, that super low friction of polyhydric alcohols could also be associated with the triboinduced degradation of glycerol, producing a nanometer-thick film containing organic acids and water. An outstanding superlubricity of steel surfaces directly lubricated by a solution of myo-inositol (also called vitamin Bh) in glycerol at ambient temperature 25 °C could also be achieved. The mechanism could be associated with the friction-induced dissociation of glycerol and interaction of water-like species with the steel surface. This remarkable superlubricity behavior has also recently been seen with other glycerol solution, with acids, or polyhydric alcohol [101, 102].

4 Physicochemistry process of nanoparticular as lubricant additives

Nanoparticles have been explored as lubricant additives for about 20 years [103]. With respect to the bulk materials, the nano additives have low melting points (in case of metallic nanoparticles), high boundary adsorption ability, and high reactivity owing to the small size and interfacial effects. Thus, they easily form boundary layers of low shearing strength at the frictional surfaces, to reduce the friction coefficient and to repair the worn surface through deposition at more severe conditions [104]. Xue et al. have proposed the tribochemistry and antiwear mechanism of organic–inorganic nanoparticles, such as the dialkyldithiophosphate coated Cu, Ag, LaF_3, and the organic acid coated TiO_2 nanoparticles as lubricant additives at different lubricating regimes [105]. The schematic lubricating mechanisms are demonstrated

in Fig. 17 [106]. Under mild sliding conditions, dialkyldithiophosphate and the organic acid can become orientated perpendicular to the specimen surface, and thus, form a film to withstand the local contact pressure. When the lubricating film between the tribo-pairs becomes thinner, and mixed or boundary lubrication occurs, the nanoparticles may carry a proportion of load and separate the two surfaces to prevent adhesion, thus benefiting the antiwear properties. When the shearing is strong, the nanoparticles' core/shell structure may be destroyed and the surface capping layer desorbed and decomposed. The inorganic core may be melted and welded (inert metal nanoparticles such as silver) on the shearing surface, or attached on the surface (adherent, laminar material such as lanthanum trifluoride), or react with the specimen to form a protective layer, thus providing good antiwear and extreme pressure properties. Oil-soluble boron containing compounds are good friction-reducing additives and possess antirust and anticorrosive properties, but they are liable to hydrolyze. Hu et al. have synthesized amorphous lanthanum borate nanoparticles as a wear resistance additive in lubricating oil [107]. The wear resistance and load carrying capacity of base oil was significantly improved. The tribochemical reaction product of FeB plays a key role in antiwear at the boundary lubricating condition.

Layered inorganic nanoparticles such as colloidal molybdenum disulfide, graphite, and boron nitride, have high slip incidence between layers that are

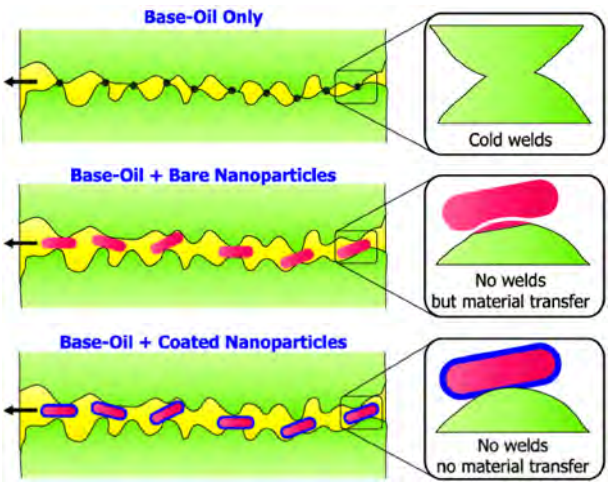

Fig. 17 Action mechanisms of nanoparticle additives [106].

good for lubrication. Tannous et al. investigated the tribological property of the fullerene-(IF)-likeMoS_2 nanoparticles for different rubbing surfaces (steel, alumina, and diamond-like carbon) [108]. The results indicated that IF-MoS_2 in PAO showed good friction reduction and antiwear properties for steel/steel contact. A tribofilm composed of 2H-MoS_2 layers was observed on steel surfaces. It was found that these MoS_2 sheets were not only incorporated in the native iron oxide layer present at the outer surface of the steel, but also a reaction occurred between MoS_2 and the iron atoms/iron oxide species. S–O, Mo–O, and Fe–S bonds were identified by X-ray photoelectron spectroscopy (XPS). WS_2 has a similar structure to MoS_2 and the WS_2 nanoparticles can reduce the friction coefficient by 30%–50% [109]. The addition of IF-WS_2 nanoparticles to the base oils results in up to 50% reduction in friction coefficient in the mixed lubrication regime.

Graphite has a layered structure and it has been used as lubricant owing to the interlayer slip. The single layer form of graphite, graphene, has received research interest recently, which can elucidate the lubricating mechanisms of graphite. Graphene itself can be used as a green nanoadditive. Eswaraiah et al. studied the tribological properties of graphene as additive in engine oil, and found that at concentration of 0.025 mg/mL, when compared with the base oil, the friction coefficient and wear scar diameter decreased by 80% and 33%, respectively. This can be attributed to the nanobearing mechanism of graphene in engine oil, and to the ultimate mechanical strength of graphene [110]. The tribological properties of oleic acid-modified graphene as PAO-9 oil additive was investigated by Zhang et al. [111]. The results showed that a lower concentration graphene (0.02–0.06 wt%) effectively improved the tribological properties of lubricating oils, with friction coefficient and wear scar diameter reduced by 17% and 14%, respectively. Graphene can form a protective layer on the surface of each steel ball at lower concentrations, which introduces the enhanced antiwear performance. However, as the graphene loading exceeds a critical value, the oil film becomes far more discontinuous, thus degrading the antiwear properties and finally leading to dry friction.

5 Conclusions and perspectives

This critical review deals with physicochemistry at frictional interfaces, and presents the frontier research of friction control and lubrication. It is very clear that interface friction depends on the interplay between lubricating media and substrates. The liquid lubrication section is organized around the traditional Stribeck curve, and points out how surface physicochemistry affects lubrication, and presents the research frontier in each regime. In liquid flow on a solid surface or in hydrodynamic lubrication of liquid film separating sliding contacts, large boundary slips are expected to result in apparent friction reduction by reducing the viscous drag. How the advance of surface science can be utilized to create a stable and large boundary slip is an issue to be further explored. In mixed and boundary lubrication, a condition in which the lubricant film becomes too thin to provide total separation, lubricating oils must completely wet a surface in order to form an effective lubricating film. One way to improve the load-carrying capacity is to strengthen the surface interaction. For rational design, high polarity oils are desirable. ILs represents such an ideal candidate. The application of ILs still faces some issues to be tackled, such as the presence of fluorine content that leads to corrosion, low temperature fluidity, and higher cost. Although there are fluorine-free ILs, it is uncertain whether the substitute ILs have comparable tribological properties, which is of importance because the appropriate triboreaction is a guarantee of good performance.

Surface adsorption is the key for the friction modifiers to assume their function. A pertinent question is whether the research progress of self-assembled monolayers can provide some new insights into designing novel additives. The novel additives must have strong enough adsorption strength (head anchors) and easy-to-shear tails. Another issue, which addresses environmental concerns, is whether we can find equivalent head anchors to replace sulphur/phosphorous containing anchors, such as by creating a multivalent interaction to enhance the interaction strength. The surface adsorption dynamics are another factor to be considered (which might vary for different additives on different substrates), but its correlation with tribological properties is rarely studied.

Biomimicking design of lubricants will be a research focus in the future. It is seemingly more helpful for aqueous lubrication. The question is whether we can find some clues to develop environmentally benign additives for oil lubrication. One apparent clue is that nature's realization of ultra-low lubrication and high load capacity depends not only on interface materials, but also on micro/nano structures. Surface ordered structures will play a key role in drag-reduction of fluid flow and in enhancing the elasto-hydrodynamic effect. Besides, how nature's self-healing capability could be used to design novel lubrication materials and techniques is another area for further research.

Under boundary lubrication condition, the tribology behavior is strongly affected by surface chemisorption and surface tribochemical reactions of additives. The reaction film product can interact with the native oxide layer and sometimes with the crystal structure of the substrate. Understanding the tribochemical reaction mechanism and the structure and composition of reaction products plays a crucial role in understanding the failure mechanism and enabling the industrial development of new lubricant systems. It is still rather difficult to carry out *in-situ* characterization at single asperity and dynamic surface adsorption at nanometer scale. Very excitingly, we have seen some progress regarding, for instance, the use of TEM and AFM to study the friction process of single asperity *in-situ*. It is supposed that more advanced surface characterization techniques will be implemented.

One final issue is the question of what to do if the entire liquid lubrication fails and dry friction comes into being. This actually happens very often when a component starts relative motion with very low speed and high load. The most feasible solution is to combine liquid and thin solid film lubrication, so that when liquid lubrication fails, the solid lubricating films will undertake the function of lubrication. It is well known that some soft metallic materials (such as Au, Ag, Cu, and their metal sulfides), polymers (polytetrafluoro-ethylene), and carbon materials have low shearing strength. Thus, thin solid films made of these materials can provide low friction coefficient and antiwear properties. By combining liquid and thin solid film lubrication, it is highly possible to realize lubrication at all regimes. The tribophysicochemistry

between liquid lubricants and thin film materials (rather than conventional steel, alloys, ceramics, etc.) will need more detailed investigation. This research will become increasingly important in the future.

Acknowledgement

The work is financially supported by the National Natural Science Foundation of China (NSFC) (Nos. 51675512 and 51705504), the National Key Basic Research and Development (973) Program of China (No. 2013CB632301), and Natural Science Foundation of Gansu Province (No. 1606RJZA051).

References

[1] Matta C, Joly-Pottuz L, De Barros Bouchet M, Martin J, Kano M, Zhang Q, Goddard W A III. Superlubricity and tribochemistry of polyhydric alcohols. *Phys Rev B* **78**: 085436 (2008)

[2] Cai M R, Guo R S, Zhou F, Liu W M. Lubricating a bright future: Lubrication contribution to energy saving and low carbon emission. *Sci China Technol Sci* **56**: 2888–2913 (2013)

[3] Zhou F, Wu Y. A novel insight into "lubrication". *Tribology* **36**: 132–136 (2016)

[4] Ye C F, Liu W M, Chen Y X, Yu L G. Room-temperature ionic liquids: A novel versatile lubricant. *Chem Comm* **21**: 2244–2245 (2001)

[5] Mu Z G, Liu W M, Zhang S. Functional room-temperature ionic liquids as lubricants for an aluminum-on-steel system. *Chem Lett* **33**: 524–525 (2004)

[6] Minami I, Inada T, Sasaki R, Nanao H. Tribo-chemistry of phosphonium-derived ionic liquids. *Tribol Lett* **40**: 225–235 (2010)

[7] Liu X Q, Zhou F, Liang Y M, Liu W M. Tribological performance of phosphonium based ionic liquids for an aluminum-on-steel system and opinions on lubrication mechanism. *Wear* **261**: 1174–1179 (2006)

[8] Shah F U, Glavatskih S, MacFarlane D R, Somers A, Forsyth M, Antzutkin O N. Novel halogen-free chelated orthoborate-phosphonium ionic liquids: Synthesis and tribophysical properties. *Phys Chem Chem Phys* **13**: 12865–12873 (2011)

[9] Qu J, Bansal D G, Yu B, Howe J Y, Luo H, Dai S, et al. Antiwear performance and mechanism of an oil-miscible ionic liquid as a lubricant additive. *ACS Appl Mater Interfaces* **4**: 997–1002 (2012)

[10] Forsyth M, Kemp T F, Howlett P C, Sun J Z, Smith M E. A potential novel rapid screening NMR approach to boundary film formation at solid interfaces in contact with ionic liquids. *J Phys Chem C* **112**: 13801–13804 (2008)

[11] Kajdas C. Importance of anionic reactive intermediates for lubricant component reactions with friction surfaces. *Lubr Sci* **6**: 203–228 (1994)

[12] Mezger M, Schröder H, Reichert H, Schramm S, Okasinski JS, Schöder S, et al. Molecular layering of fluorinated ionic liquids at a charged sapphire (0001) surface. *Science* **322**: 424–428 (2008)

[13] Li H, Wood R J, Rutland M W, Atkin R. An ionic liquid lubricant enables superlubricity to be "switched on" in situ using an electrical potential. *Chem Comm* **50**: 4368–4370 (2014)

[14] Spikes H. Friction modifier additives. *Tribol Lett* **60**: 5 (2015)

[15] Bowden F P, Gregory J N, Tabor D. Lubrication of metal surfaces by fatty acids. *Nature* **156**: 97–101 (1945)

[16] Minami I, Mori S. Concept of molecular design towards additive technology for advanced lubricants. *Lubr Sci* **19**: 127–149 (2007)

[17] Ulman A. Formation and structure of self-assembled monolayers. *Chem Rev* **96**: 1533–1554 (1996)

[18] Ye Q, Zhou F, Liu W M. Bioinspired catecholic chemistry for surface modification. *Chem Soc Rev* **40**: 4244–4258 (2011)

[19] Takahashi K, Shitara Y, Kaimai T, Kanno A, Mori S. Lubricating properties of TR Gel-lube—Influence of chemical structure and content of gel agent. *Tribol Int* **43**: 1577–1583 (2010)

[20] Ohno N, Mia S, Masuhara K, Sonoda K, Yamashita Y, Tamura Y, Morita S, Shitara Y. Tribological properties and film formation behavior of thermoreversible gel lubricants. *Tribol Trans* **53**: 722–730 (2010)

[21] Yu Q L, Fan M J, Li D M, Song Z H, Cai M R, Zhou F, Liu W M. Thermoreversible gel lubricants through universal supramolecular assembly of a nonionic surfactant in a variety of base lubricating liquids. *ACS Appl Mater Interfaces* **6**: 15783–15794 (2014)

[22] Huang G W, Yu Q L, Cai M R, Zhou F, Liu W M. Highlighting the effect of interfacial interaction on tribological

properties of supramolecular gel lubricants. *ACS Appl Mater Interfaces* **3** (2016)

[23] Yu Q L, Huang G W, Cai M R, Zhou F, Liu W M. In situ zwitterionic supramolecular gel lubricants for significantly improved tribological properties. *Tribol Int* **95**: 55–65 (2016)

[24] Yu Q L, Li D M, Cai M R, Zhou F, Liu W M. Supramolecular gel lubricants based on amino acid derivative gelators. *Tribol Lett* **61** (2016)

[25] Cai M R, Liang Y M, Zhou F, Liu W M. Functional ionic gels formed by supramolecular assembly of a novel low molecular weight anticorrosive/antioxidative gelator. *J Mater Chem* **21**: 13399 (2011)

[26] Yu Q L, Wu Y, Li D M, Cai M R, Zhou F, Liu W M. Supramolecular ionogel lubricants with imidazolium-based ionic liquids bearing the urea group as gelator. *J Colloid Interf Sci* **487**: 130–140 (2017)

[27] Wathier M, Lakin B A, Bansal P N, Stoddart S S, Snyder B D, Grinstaff M W. A large-molecular-weight polyanion, synthesized via ring-opening metathesis polymerization, as a lubricant for human articular cartilage. *J Am Chem Soc* **135**: 4930–4933 (2013)

[28] Briscoe W H, Titmuss S, Tiberg F, Thomas R K, McGillivray D J, Klein J. Boundary lubrication under water. *Nature* **444**: 191–194 (2006)

[29] Goldberg R, Schroeder A, Silbert G, Turjeman K, Barenholz Y, Klein J. Boundary lubricants with exceptionally low friction coefficients based on 2D close-packed phosphatidylcholine liposomes. *Adv Mater* **23**: 3517–3521 (2011)

[30] Klein J. Hydration lubrication. *Friction* **1**: 1–23 (2013)

[31] Raviv U, Giasson S, Kampf N, Gohy J F, Jerome R, Klein J. Lubrication by charged polymers. *Nature* **425**: 163–165 (2003)

[32] Lee S, Spencer N D. Materials science. Sweet, hairy, soft, and slippery. *Science* **319**: 575–576 (2008)

[33] Klein J. Repair or peplacement: A joint perspective. *Science* **323**: 47–48 (2009)

[34] Hartung W, Rossi A, Lee S, Spencer N D. Aqueous lubrication of SiC and Si_3N_4 ceramics aided by a brush-like copolymer additive, poly(l-lysine)-graft-poly(ethylene glycol). *Tribol Lett* **34**: 201–210 (2009)

[35] Perry S S, Yan X, Limpoco F T, Lee S, Muller M, Spencer N D. Tribological properties of poly(L-lysine)-graft-poly(ethylene glycol) films: Influence of polymer architecture and adsorbed conformation. *ACS Appl Mater Interfaces* **1**: 1224–1230 (2009)

[36] Heeb R, Bielecki R M, Lee S, Spencer N D. Room-temperature, aqueous-phase fabrication of poly(methacrylic acid) brushes by UV-LED-induced, controlled radical polymerization with high selectivity for surface-bound species. *Macromolecules* **42**: 9124–9132 (2009)

[37] Chen M, Briscoe W H, Armes S P, Klein J. Lubrication at physiological pressures by polyzwitterionic brushes. *Science* **323**: 1698–1701 (2009)

[38] Wei Q, Cai M, Zhou F, Liu W. Dramatically tuning friction using responsive polyelectrolyte brushes. *Macromolecules* **46**: 9368–9379 (2013)

[39] Nordgren N, Rutland M W. Tunable nanolubrication between dual-responsive polyionic grafts. *Nano Lett* **9**: 2984–2990 (2009)

[40] Zhang R, Ma S H, Wei Q B, Ye Q, Yu B, Gucht J V D, Zhou F. The weak interaction of surfactants with polymer brushes and its impact on lubricating behavior. *Macromolecules* **48**: 6186–6196 (2015)

[41] Kyomoto M, Moro T, Saiga K, Miyaji F, Kawaguchi H, Takatori Y, Nakamura K, Ishihara K. Lubricity and stability of poly(2-methacryloyloxyethylphosphorylcholine) polymer layer on Co-Cr-Mo surface for hemi-arthroplasty to prevent degeneration of articular cartilage. *Biomaterials* **31**: 658–668 (2010)

[42] Kyomoto M, Moro T, Saiga K, Hashimoto M, Ito H, Kawaguchi H, Takatori Y, Ishihara K. Biomimetic hydration lubrication with various polyelectrolyte layers on cross-linked polyethylene orthopedic bearing materials. *Biomaterials* **33**: 4451–4459 (2012)

[43] Kobayashi M, Terada M, Takahara A. Polyelectrolyte brushes: A novel stable lubrication system in aqueous conditions. *Faraday Discussions* **156**: 403–412 (2012)

[44] Philippon D, De Barros-Bouchet M I, Le Mogne T, Lerasle O, Bouffet A, Martin J M. Role of nascent metallic surfaces on the tribochemistry of phosphite lubricant additives. *Tribol Int* **44**: 684–691 (2011)

[45] Hsu S M, Zhang J, Yin Z F. The nature and origin of tribochemistry. *Tribol Lett* **13**: 131–139 (2002)

[46] Nakayama K. Triboemission of electrons, ions, and photons from diamondlike carbon films and generation of tribomicroplasma. *Surface & Coatings Technology* **188**: 599–604 (2004)

[47] Nakayama K. Effect of magnetic field on the plasma generated during a sliding contact. *J Phys: Conf Ser* 2011: 012069 (2011)

[48] Nakayama K. Mechanism of triboplasma generation in oil. *Tribol Lett* **41**: 345–351 (2011)

[49] Nakayama K, Hashimoto H. Triboemission, tribochemical reaction, and friction and wear in ceramics under various n-butane gas pressures. *Tribol Int* **29**: 385–393 (1996)

[50] Nakayama K, Martin J M. Tribochemical reactions at and in the vicinity of a sliding contact. *Wear* **261**: 235–240 (2006)

[51] Spikes H. The history and mechanisms of ZDDP. *Tribol Lett* **17**: 469–489 (2004)

[52] Topolovec-Miklozic K, Forbus T R, Spikes H A. Film thickness and roughness of ZDDP antiwear films. *Tribol Lett* **26**: 161–171 (2007)

[53] Mosey N J. Molecular mechanisms for the functionality of lubricant additives. *Science* **307**: 1612–1615 (2005)

[54] Gosvami N N, Bares J A, Mangolini F, Konicek A R, Yablon D G, Carpick R W. Mechanisms of antiwear tribofilm growth revealed in situ by single-asperity sliding contacts. *Science* **348**: 102–106 (2015)

[55] Morina A, Neville A, Priest M, Green J H. ZDDP and MoDTC interactions and their effect on tribological performance – tribofilm characteristics and its evolution. *Tribol Lett* **24**: 243–256 (2006)

[56] Grossiord C, Varlot K, Martin J-M, Th. Le Mogne C E, Inoue K. MoS_2 single sheet lubrication by molybdenum dithiocarbamate. *Tribol Int* **31**: 737–747 (1998)

[57] Shah F U, Glavatskih S, Höglund E, Lindberg M, Antzutkin O N. Interfacial antiwear and physicochemical properties of alkylborate-dithiophosphates. *ACS Appl Mater Interfaces* **3**: 956–968 (2011)

[58] Zhou F, Liang Y M, Liu W M. Ionic liquid lubricants: Designed chemistry for engineering applications. *Chem Soc Rev* **38**: 2590–2599 (2009)

[59] Huang G W, Yu Q L, Cai M R, Zhou F, Liu W M. Investigation of the lubricity and antiwear behavior of guanidinium ionic liquids at high temperature. *Tribol Int* **114**: 65–76 (2017)

[60] Zhang S W, Hu L T, Qiao D, Feng D P, Wang H Z. Vacuum tribological performance of phosphonium-based ionic liquids as lubricants and lubricant additives of multialkylated cyclopentanes. *Tribol Int* **66**: 289–295 (2013)

[61] Fan M J, Yang D S, Wang X L, Liu W M, Fu H Z. DOSS-based QAILs: As both neat lubricants and lubricant additives with excellent tribological properties and good detergency. *Ind Eng Chem Res* **53**: 17952–17960 (2014)

[62] Otero I, Lopez E R, Reichelt M, Villanueva M, Salgado J, Fernandez J. Ionic liquids based on phosphonium cations as neat lubricants or lubricant additives for a steel/steel contact. *ACS Appl Mater Interfaces* **6**: 13115–13128 (2014)

[63] Qiao D, Wang H Z, Feng D P. Tribological performance and mechanism of phosphate ionic liquids as additives in three base oils for steel-on-aluminum contact. *Tribol Lett* **55**: 517–531 (2014)

[64] Anand M, Hadfield M, Viesca J L, Thomas B, Battez A H, Austen S. Ionic liquids as tribological performance improving additive for in-service and used fully-formulated diesel engine lubricants. *Wear* **334**: 67–74 (2015)

[65] Fu X S, Sun L G, Zhou X G, Li Z P, Ren T H. Tribological study of oil-miscible quaternary ammonium phosphites ionic liquids as lubricant additives in PAO. *Tribol Lett* **60**: 23 (2015)

[66] Qu J, Barnhill W C, Luo H M, Meyer H M, 3rd, Leonard D N, Landauer A K, Kheireddin B, Gao H, Papke B L, Dai S. Synergistic effects between phosphonium-alkylphosphate ionic liquids and zinc dialkyldithiophosphate (ZDDP) as lubricant additives. *Adv Mater* **27**: 4767–4774 (2015)

[67] Qu J, Meyer H M, III, Cai Z B, Ma C, Luo H M. Characterization of ZDDP and ionic liquid tribofilms on non-metallic coatings providing insights of tribofilm formation mechanisms. *Wear* **332**: 1273–1285 (2015)

[68] Li H, Somers A E, Howlett P C, Rutland M W, Forsyth M, Atkin R. Addition of low concentrations of an ionic liquid to a base oil reduces friction over multiple length scales: A combined nano- and macrotribology investigation. *Phys Chem Chem Phys* **18**: 6541–6547 (2016)

[69] Huang G W, Yu Q L, Ma Z F, Cai M R, Liu W M. Probing the lubricating mechanism of oil-soluble ionic liquids additives. *Tribol Int* **107**: 152–162 (2017)

[70] Zhou Y, Qu J. Ionic liquids as lubricant additives: a review. *ACS Appl Mater Interfaces* **9**: 3209–3222 (2017)

[71] Gusain R, Gupta P, Saran S, Khatri O P. Halogen-free bis(imidazolium)/bis(ammonium)di bis(salicylato)borate ionic liquids as energy-efficient and environmentally friendly lubricant additives. *ACS Appl Mater Inter* **6**: 15318–15328 (2014)

[72] Gusain R, Singh R, Sivakumar K L N, Khatri O P. Halogen-free imidazolium/ammonium-bis(salicylato)borate ionic liquids as high performance lubricant additives. *RSC Adv* **4**: 1293–1301 (2014)

[73] Taher M, Shah F U, Filippov A, de Baets P, Glavatskih S, Antzutkin O N. Halogen-free pyrrolidinium bis(mandelato)borate ionic liquids: Some physicochemical properties and lubrication performance as additives to polyethylene glycol. *RSC Adv* **4**: 30617–30623 (2014)

[74] Khatri P K, Joshi C, Thakre G D, Jain S L. Halogen-free ammonium-organoborate ionic liquids as lubricating additives: The effect of alkyl chain lengths on the tribological performance. *New J Chem* **40**: 5294–5299 (2016)

[75] Gusain R, Bakshi P S, Panda S, Sharma O P, Gardas R, Khatri O P. Physicochemical and tribophysical properties of trioctylalkylammonium bis(salicylato)borate (N888n-BScB) ionic liquids: Effect of alkyl chain length. *Phys Chem Chem Phys* **19**: 6433–6442 (2017)

[76] Minami I, Kamimura H, Mori S. Thermo-oxidative stability of ionic liquids as lubricating fluids. *J Synth Lubr* **24**: 135–147 (2007)

[77] Minami I. Ionic liquids in tribology. *Molecules* **14**: 2286–2305 (2009)

[78] Cai M R, Liang Y M, Zhou F, Liu W M. Anticorrosion imidazolium ionic liquids as the additive in poly(ethylene glycol) for steel/Cu-Sn alloy contacts. *Faraday Discuss* **156**: 147–157 (2012)

[79] Cai M R, Liang Y M, Zhou F, Liu W M. Tribological properties of novel imidazolium ionic liquids bearing benzotriazole group as the antiwear/anticorrosion additive in poly(ethylene glycol) and polyurea grease for steel/steel Contacts. *ACS Appl Mater Interfaces* **3**: 4580–4592 (2011)

[80] Cai M R, Liang Y M, Yao M H, Xia Y Q, Zhou F, Liu W M. Imidazolium ionic liquids as antiwear and antioxidant additive in poly(ethylene glycol) for steel/steel contacts. *Acs Appl Mater Interfaces* **2**: 870–876 (2010)

[81] Cai M R, Liang Y M, Zhou F, Liu W M. A novel imidazolium salt with antioxidation and anticorrosion dual functionalities as the additive in poly(ethylene glycol) for steel/steel contacts. *Wear* **306**: 197–208 (2013)

[82] Song Z H, Cai M R, Liang Y M, Fan M J, Zhou F, Liu W M. In situ preparation of anti-corrosion ionic liquids as the lubricant additives in multiply-alkylated cyclopentanes. *Rsc Adv* **3**: 21715–21721 (2013)

[83] Song Z H, Liang Y M, Fan M J, Zhou F, Liu W M. Lithium-based ionic liquids as novel lubricant additives for multiply alkylated cyclopentanes (MACs). *Friction* **2**: 392 (2014)

[84] Fan M, Liang Y, Zhou F, Liu W. Dramatically improved friction reduction and wear resistance by in situ formed ionic liquids. *Rsc Adv* **2**: 6824–6830 (2012)

[85] Wang Y R, Yu Q L, Cai M R, Shi L, Zhou F, Liu W M. Synergy of lithium salt and non-ionic surfactant for significantly improved tribological properties of water-based fluids. *Tribol Int* **113**: 58–64 (2016)

[86] Fan M J, Song Z H, Liang Y M, Zhou F, Liu W M. In situ formed ionic liquids in synthetic esters for significantly improved lubrication. *ACS Appl Mater Interfaces* **4**: 6683–6689 (2012)

[87] Hirano M. Superlubricity: A state of vanishing friction. *Wear* **254**: 932–940 (2003)

[88] Chhowalla M, Amaratunga G A J. Thin films of fullerene-like MoS_2 nanoparticles with ultra-low friction and wear. *Nature* **407**: 164–167 (2000)

[89] Heimberg J A, Wahl K J, Singer I L, Erdemir A. Superlow friction behavior of diamond-like carbon coatings: time and speed effects. *Appl Phys Lett* **78**: 2449 (2001)

[90] Li H, Wang J, Gao S, Chen Q, Peng L, Liu K, Wei X. Superlubricity between MoS_2 monolayers. *Adv Mater* **29**: 1701474 (2017)

[91] Li J, Zhang C, Luo J. Superlubricity behavior with phosphoric acid-water network induced by rubbing. *Langmuir* **27**: 9413–9417 (2011)

[92] Li J, Luo J. Advancements in superlubricity. *Sci China Technol Sci* **56**: 2877–2887 (2013)

[93] Li J J, Zhang C H, Deng M M, Luo J B. Investigations of the superlubricity of sapphire against ruby under phosphoric acid lubrication, *Friction* **2**: 164–172 (2014)

[94] Zeng Q F, Dong G N, Martin J M. Green superlubricity of nitinol 60 alloy against steel in presence of castor oil. *Adv Mater Interfaces* **6**: 29992 (2016)

[95] Zhang C X, Liu Z F, Liu Y H, Cheng Q, Yang C B, Cai L G. Investigation of the mechanisms for stable superlubricity of poly(vinylphosphonic acid) (PVPA) coatings affected by lubricant. *Friction* **4**: 303–312 (2016)

[96] Zhang C-H, Ma Z-Z, Luo J-B, Lu X-C, Wen S-Z. Superlubricity of a mixed aqueous solution. *Chinese Phys Lett* **28**: 056201 (2011)

[97] Li J J, Zhang C H, Cheng P, Chen X C, Wang W Q, Luo J B. AFM Studies on liquid superlubricity between silica surfaces achieved with surfactant micelles. *Langmuir* **32**: 5593–5599 (2016)

[98] Li J, Ma L, Zhang S, Zhang C, Liu Y, Luo J. Investigations on the mechanism of superlubricity achieved with phosphoric acid solution by direct observation. *J Appl Phys* **114**: 114901 (2013)

[99] Li J, Zhang C, Sun L, Lu X, Luo J. Tribochemistry and superlubricity induced by hydrogen ions. *Langmuir* **28**: 15816–15823 (2012)

[100] Yue D-C, Ma T-B, Hu Y-Z, Yeon J, van Duin A C T, Wang H, Luo J B. Tribochemistry of phosphoric acid sheared between quartz surfaces: A reactive molecular dynamics study. *J Phys Chem C* **117**: 25604–25614 (2013)

[101] Li J, Zhang C, Luo J. Superlubricity achieved with mixtures of polyhydroxy alcohols and acids. *Langmuir* **29**: 5239 5245 (2013)

[102] Li J, Zhang C, Ma L, Liu Y, Luo J. Superlubricity achieved with mixtures of acids and glycerol. *Langmuir* **29**: 271–275 (2013)

[103] Zhang Z J, Zhang J, Xue Q J. Synthesis and characterization of a molybdenum disulfide nanoclustert. *J Phys Chem* **98**: 12973–12977 (1994)

[104] Liu W M, Wang X B. Nanolubricants made of metals. *In Nanolubricants.* Martinc J M, Ed. England: John Wiley & Sons, 2008: 175–201 (2008)

[105] Li B, Wang X, Liu W, Xue Q. Tribochemistry and antiwear mechanism of organic–inorganic nanoparticles as lubricant additives. *Tribol Lett* **22**: 79–84 (2006)

[106] Akbulut M. Nanoparticle-based lubrication systems. *J Powder MetallMin* **1**: 1000e1101 (2012)

[107] Hu Z S, Dong J X, Chen G X, He J Z. Preparation and tribological properties of nanoparticle lanthanum borate. *Wear* **243**: 43–47 (2000)

[108] Tannous J, Dassenoy F, Lahouij I, Mogne T, Vacher B, Bruhács A, Tremel W. Understanding the tribochemical mechanisms of IF-MoS_2 nanoparticles under boundary lubrication. *Tribol Lett* **41**: 55–64 (2010)

[109] Greenberg R, Halperin G, Etsion I, Tenne R. The effect of WS_2 nanoparticles on friction reduction in various lubrication regimes. *Tribol Lett* **17**: 179–186 (2004)

[110] Eswaraiah V, Sankaranarayanan V, Ramaprabhu S. Graphene-based engine oil nanofluids for tribological applications. *ACS Appl Mater Interfaces* **3**: 4221-4227 (2011)

[111] Zhang W, Zhou M, Zhu H, Tian Y, Wang K, Wei J, Ji F, Li X, Li Z, Zhang P, Wu D. Tribological properties of oleic acid-modified graphene as lubricant oil additives. *J Phys D: Appl Phys* **44**: 205303 (2011)

Meirong CAI. She got her PhD degree in 2012 at the Lanzhou Institute of Chemical Physics. She is an associate professor at the State Key Lab of Solid Lubrication in Lanzhou Institute of Chemical Physics, CAS. She has authored or co-authored more than 40 journal papers. Her research interests are ionic liquids lubricants and supramolecular gel lubricants.

Qiangliang YU. He got his PhD degree in 2016 at the Lanzhou Institute of Chemical Physics. He is an assistant at the State Key Lab of Solid Lubrication in Lanzhou Institute of Chemical Physics, CAS. His research interests are ionic liquids lubricants and anticorrosive additives.

Feng ZHOU. He is a full professor in Lanzhou Institute of Chemical Physics, CAS and deputy director of State Key Laboratory of Solid Lubrication. He gained PhD degree in 2004 and spent three years (2005—2008) in the Department of Chemistry, University of Cambridge as a research associate. He has published more than 300 journal papers that received more than 10,000 citations and has the H-index 60. His research interests include the bioninspired tribology, biomimic surfaces/interfaces of soft matters, drag-reduction and antibiofouling, and functional coatings. He has gained a number of awards including "Outstanding Youth Award" of International Society of Bionic Engineering, 2013. He serves as editorial board member of *Tribology International*, *Journal Fiber Bioengineering and Informatics*, etc.

Weimin LIU. He received his Ph.D. degree in lubricating materials and tribology from Lanzhou Institute of Chemical Physics (LICP) of the Chinese Academy of Sciences in 1990. After that, he joined the State Key Laboratory of Solid Lubrication (LSL) of the LICP. From June 1993 to June 1994, he worked as a visiting scholar at Pennsylvania State University, USA. In 2013, he was elected the Member of the Chinese Academy of Sciences. Currently, he is a professor of LICP and head of the State Key Laboratory of Solid Lubrication. Up to now, he has published more than 500 papers with citation over 20,000. He holds 80 Chinese patents and 1 US patent; won 2 National Awards for Technological Invention (second class) and 1 National Award for Natural Sciences (second class). Currently, his research interests mainly focus on space and aviation lubrication, high performance lubricating materials, and tribochemistry.

Friction **5**(4): 383–391 (2017)
DOI 10.1007/s40544-017-0150-1
ISSN 2223-7690
CN 10-1237/TH
RESEARCH ARTICLE

Effect of stick-slip on magneto-rheological elastomer with a magnetic field

Chenglong LIAN[1], Kwang-hee LEE[1], Jun-wook AN[2], Chul-hee LEE[1,*]

[1] *Department of Mechanical Engineering, Inha University, 100 Inharo, Nam-gu, Incheon 22212, Republic of Korea*

[2] *Department of Construction Machinery Engineering, Inha University, 100 Inharo, Nam-gu, Incheon 22212, Republic of Korea*

Received: 06 December 2016 / Revised: 13 January 2017 / Accepted: 17 January 2017

Abstract: This study investigated the stick-slip characteristics of a magneto-rheological elastomer (MRE) against an aluminum plate. Herein, the MRE was manufactured, and a stick-slip tester was employed to evaluate the stick-slip performance of the MRE under different velocities and load conditions with and without a magnetic field. The fast Fourier transform (FFT) of the friction force of the stick-slip and the roughness of the aluminum plate surface were calculated to confirm the stick-slip phenomenon. After the tests, the wear surfaces were observed to evaluate the wear properties of the MRE regarding the stick-slip. Results showed that the stick-slip was smaller at lower velocity. At higher velocity, the reduction of the stick-slip under a magnetic field was more clearly observed. Moreover, the wear reduced with reduced stick-slip under a magnetic field.

Keywords: stick-slip; friction; wear; magneto-rheological elastomer

1 Introduction

Magneto-rheological (MR) materials are intelligent materials with rheological properties that can be rapidly and reversibly controlled by the application of an external magnetic field. This effect was first studied by Jacob Rabinow [1]. The MR elastomer (MRE) is a type of MR material, and its hardness or shear modulus can be changed under a magnetic field [1, 2]. Compared to the MR fluid (MRF), the advantages of the MRE include the prevention of the carbonyl iron (CI) particles from settling on them over time; the need for their storage in a container is eliminated. Moreover, the response time of the MRE is relatively short. Because of these properties, the MR effect of MREs is widely studied, and they are applied in mechanical and automotive industries [2−10]. Owing to the wide use of elastomers for mechanical applications, such as tires and vibration reduction or absorption components, the MRE can also provide a wider range of study and application opportunities.

Numerous studies have been conducted on MREs to control vibration in mechanical systems. For example, the Ford Research Laboratory (US) developed variable stiffness suspension bushings using MREs. Gong developed a real-time tunable stiffness and damping vibration isolator based on MREs and other studies [2–5]. The tribology properties of MREs have been studied because the hardness of MRE can be changed by an applied magnetic field. Lee studied the tribological properties of MREs and showed that the friction coefficient of MREs can be changed under a magnetic field [6, 7].

Stick-slip is a special tribological phenomenon that can lead to vibration, noise, wear and reduce the lifetime of friction pairs [11−13]. Therefore, studies have been performed to reduce stick-slip. The relation between stick-slip and Schallamach waves has been studied to reduce the stick-slip and wear under various loads and velocity conditions [14−17]. The generation

* Corresponding author: Chul-hee LEE, E-mail: chulhee@inha.ac.kr

of stick-slip is mainly due to the difference between the static and dynamic friction forces [11−13]. Stick-slip can be reduced when the difference between the static and dynamic friction forces is reduced, which has been widely studied through various modeling methods [18, 19].

In previous studies, the friction properties of MREs have been confirmed to change under a magnetic field by changing the hardness. Moreover, it is possible to reduce the difference between the dynamic and static friction forces to reduce the stick-slip by changing the strength of the applied magnetic field. However, until now, the stick-slip properties of MREs have not been well studied, particularly through experiments. In this study, MREs were tested with various loads and velocities under a magnetic field. The friction force was measured to evaluate the stick-slip phenomenon, and the average friction force and its standard deviation (SD) were calculated. The fast Fourier transform (FFT) of stick-slip and the roughness of an aluminum plate were compared, and the wear surfaces of the MREs were observed using an optical microscope to evaluate the wear under different experimental conditions.

2 Preparation of the MRE sample

Based on previous studies that showed silicon-based MREs have the best MR effect, silicon was used as the matrix for the MREs in this study [1, 6, 7]. The fabrication process of the MRE comprises mixing, pre-configuration, solidification, and cooling. Before solidification, vacuum processing is conducted to eliminate any air bubbles in the MRE because air bubbles can affect the MR effect or durability. The thickness of the MRE specimen is set as 15 mm by considering the strength of the magnetic field, MR effect, and hardness. Figure 1 shows a photograph of the MRE. A circular plate with a diameter of 60 mm is designed to ensure the applied magnetic field is uniform.

Scanning electron microscope (SEM) images of the fabricated MRE are shown in Fig. 2. White CI particles are observed to be distributed in the black region, which is the silicon matrix. The average size and content by weight of the CI particles are about 10 μm and 79.8% ± 2.0%, respectively.

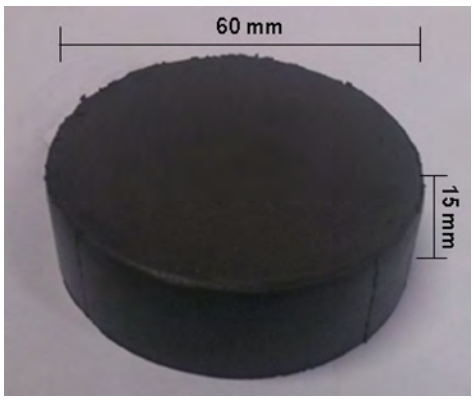

Fig. 1 Dimensions of MRE.

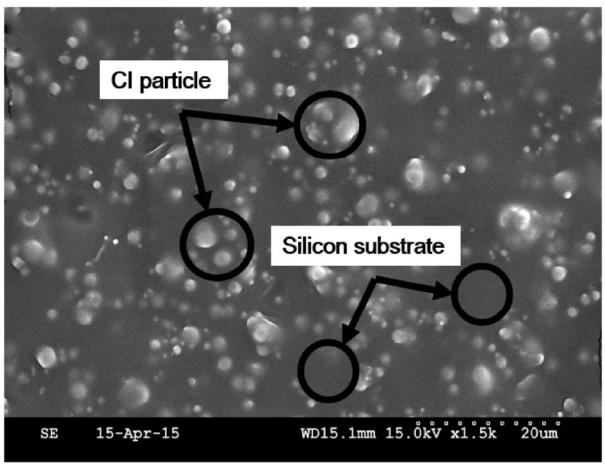

Fig. 2 SEM image of MRE.

3 Experimental setup and conditions

Figure 3 shows a schematic of the stick-slip tester for the MRE. The tester comprises a power supply, push-pull gauge (IMADA DS2-50N), slider, electromagnet, and the MRE. The MRE is placed below the electromagnet, where the load is applied. The electromagnet and MRE are fixed in the plastic case, which is connected to a slider. The slider is driven by LabVIEW, and the friction force is measured by a push-pull gauge. The measured friction forces are collected in real time by a personal computer, which also controls the current through a power supply to adjust the magnetic field of the electromagnet. Undesired magnetic fields due to magnetization make it difficult to compare the results of the stick-slip properties of the MRE; therefore, all the equipment was made of plastic or aluminum, which are widely used in various mechanical systems and are not affected by the

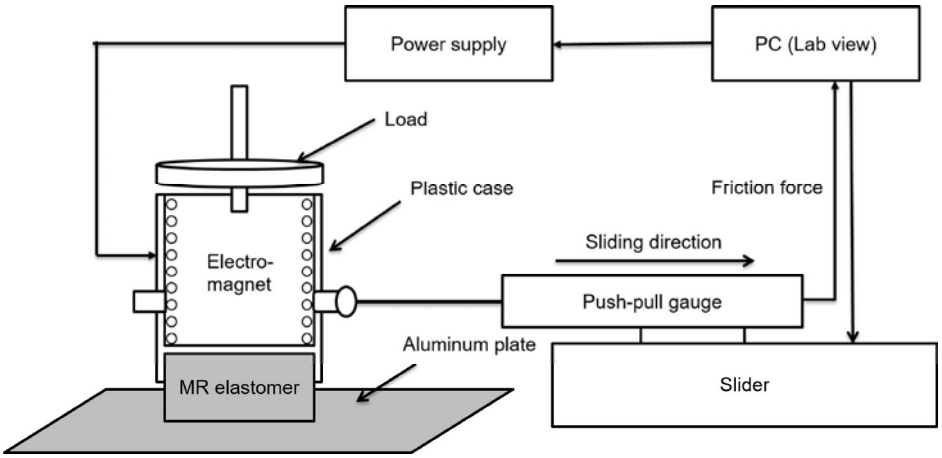

Fig. 3 Schematic diagram of stick-slip tester.

magnetic field. The friction force is related to the hardness, which was indirectly measured for each MRE before the tests, with and without a magnetic field, using a durometer (Mitutoyo HH-336-01 shore durometer).

The detailed test conditions are described in Table 1. The stick-slip is closely related to the applied velocity and load. Because the silicone-based MRE is a soft material, it is only suited for used under low-load test conditions to prevent excessive damage. The appropriate velocity was also chosen for reducing the temperature effect on the surface of the MRE, which can cause damage under high velocity. The effect of stick-slip was studied under different velocities of 20, 10, and 1 mm/s with a fixed load of 1.0 kgf, and then under different loads of 1.2, 1.5, and 2.0 kgf with a fixed velocity of 1 mm/s. Each test was performed both with and without a magnetic field. The wear surfaces of the MREs were observed using an optical microscope.

Table 1 Conditions of stick-slip test.

Test No.	Velocity (mm/s)	Load (kgf)	Magnetic field (80 mT)
a	20	1.0	OFF
b			ON
c	10		OFF
d			ON
e	1		OFF
f			ON
g		1.2	OFF
h			ON
i		1.5	OFF
j			ON
k		2.0	OFF
l			ON

In practical applications, MREs are mainly used in real-time control systems. By adjusting the external magnetic field, the required properties of MREs can be obtained. Real-time control tests are required to study the stick-slip characteristics of MREs when the magnetic field is varied. Tests were conducted under loads of 1.0 and 1.2 kgf with a fixed velocity of 1 mm/s or 5 mm/s. The magnetic field was applied at the middle time point of the experiment. Each test was conducted more than two times. The average friction force and SD were calculated to analyze the stick-slip.

4 Results and discussion

Before conducting the tests, the hardness of the MRE was measured with and without a magnetic field, and the results revealed that the hardness of the MRE increased to 12.5 HA under an 80-mT magnetic field, which is higher than the hardness measured when no magnetic field was applied (10.5 HA). Figures 4 and 5 show the stick-slip results of the MRE under different velocities and loads from tests a to l in Table 1.

Figures 4(a), 4(b), and 4(c) show the results of the friction force under a load of 1.0 kgf and velocities of 20, 10, and 1 mm/s without and with a magnetic field.

Figure 4(a) shows that the rate of frequency change of the friction force increased with the magnetic field. The hardness of the MRE increased and became more similar to the hardness of the aluminum plate. The difference between the hardness of friction pairs reduced, thus reducing the stick-slip. Figure 4(b) shows that the rate of frequency change of the friction force increased and the variation amplitude of the friction force decreased under the magnetic field. These results show that stick-slip can be reduced using a magnetic field under relatively high velocity conditions. Figure 4(c) shows the friction force results under a load of 1.0 kgf with a velocity of 1 mm/s. There is a small change in the frequency of the friction force but hardly any change in the amplitude with and without a magnetic field. It is assumed that the stick-slip was not affected by the magnetic field under a low velocity condition.

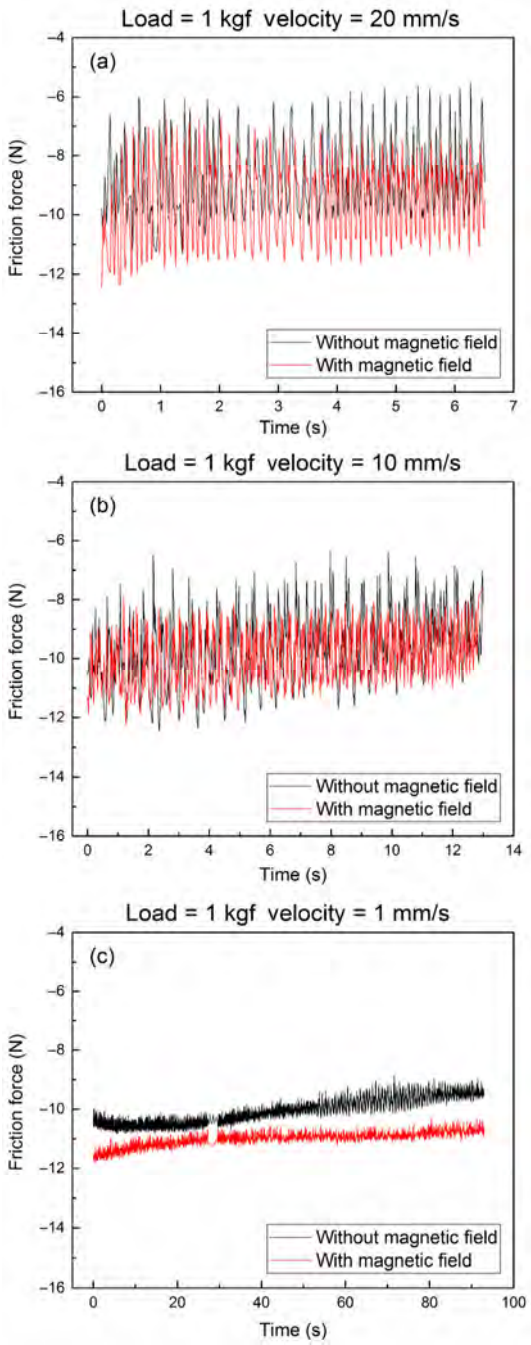

Fig. 4 Results of friction force tests under load of 1.0 kgf without and with a magnetic field: (a) velocity of 20 mm/s, (b) velocity of 10 mm/s, (c) velocity of 1 mm/s.

In theory, the dynamic friction force is not related to velocity because there is no change in the pressure and area due to the force [20]. However, the dynamic friction force was small when the velocity was increased because of the changes of the contact surface, which has been confirmed in previous studies [20–22]. It can be speculated that the dynamic friction force increases with decrease in velocity. The difference between the static and dynamic friction forces becomes small, and the stick-slip is also small.

The friction force test results under different load conditions are shown in Figs. 5(a), 5(b), and 5(c), which were obtained with a velocity of 1 mm/s and loads of 1.2, 1.5, and 2.0 kgf, without and with magnetic field. Results of the rate of frequency change of the friction force without and with the magnetic field show no differences in Fig. 5(a), which is also the case for Fig. 5(b). However, the variation amplitude of the friction force increased after 75 s during the test without a magnetic field, which was not shown in the test with a magnetic field in Fig. 5(b) and is the same as that in Fig. 5(c). A possible reason is that the surface deformation increased without the magnetic field when a high load was applied. When a high load was applied, the deformation of the MRE without a magnetic field was larger than that with a magnetic field because the hardness of the MRE without the magnetic field is lower. The larger surface deformation results in an irregular surface state, which may lead to a large change of friction force or a large stick slip.

In general, the hardness of MRE increases and the friction force decreases under a magnetic field, but the results in the figures show contradictory results. A possible reason for this is that the silicon-based MRE

is soft. The actual contact area of the MRE with the aluminum plate without a magnetic field is smaller than that with a magnetic field, which leads to a small friction force. When applying a magnetic field at the beginning of the test, the hardness of the MRE, contact area, and friction force increase compared to the case with no magnetic field. In addition, the friction force decreases with high velocity and increases with a high load, as shown in Fig. 5.

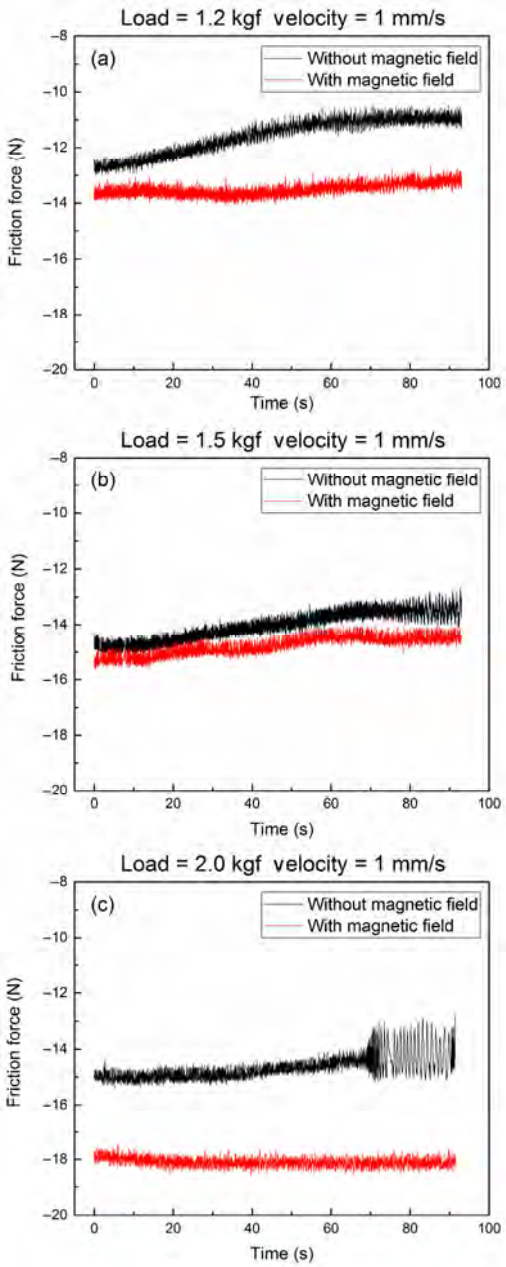

Fig. 5 Results of friction force tests under velocity of 1 mm/s without and with a magnetic field: (a) load of 1.2 kgf, (b) load of 1.5 kgf, (c) load of 2.0 kgf.

Figure 6 and Table 2 show the average friction force and the SD of tests a–l in Table 1. The friction force data were obtained from the stable friction force region. In general, the friction force with a magnetic field (tests b, d, f, h, j, and l) is larger than that without a magnetic field (tests a, c, e, g, i, and k). A possible reason for this phenomenon is the softness of the MRE (10.5–12.5 HA). The contact area and friction force under a magnetic field are larger than those without a magnetic field at the start of the tests, as previously mentioned.

The SD with a magnetic field is smaller than that without a magnetic field, except in tests a and b. The stick-slip reduces when a magnetic field is applied through the reduced SD since the difference between the static and dynamic friction forces decreases. However, tests a and b did not show the same result.

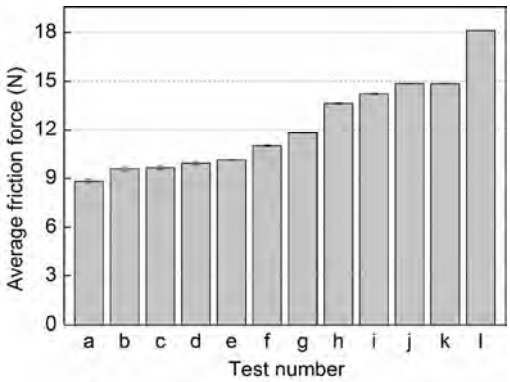

Fig. 6 Average friction force of tests.

Table 2 SD of tests (a)-(l) of Figs. 4 and 5.

Test No.	Standard deviation
a	1.179
b	1.288
c	1.155
d	0.942
e	0.439
f	0.226
g	0.562
h	0.173
i	0.446
j	0.325
k	0.219
l	0.158

A possible reason is the instability of the test system under high velocity. Under high velocity conditions, the MRE may show a little displacement perpendicular to the movement direction of the MRE. This unexpected tiny displacement is assumed to increase the experiment error.

The tests show that it is possible to change the stick-slip of the MRE with a magnetic field. Another test was performed to see if the stick-slip can be controlled in real-time with a magnetic field for use in an actual application. An 80-mT magnetic field was applied after passing about half the total test distance, and the results are shown in Figs. 7(a)–7(d). Figures 7(a) and 7(b) show the results obtained with a velocity of 1 mm/s and loads of 1.0 and 1.2 kgf, respectively. All the friction forces with the magnetic field decreased by 20% compared to those when the magnetic field was not applied, but the stick-slip did not show an obvious effect under the magnetic field regarding rate of frequency changes of the friction force. Figures 7(c) and 7(d) show the results for loads of 1.0 and 1.2 kgf with a velocity of 5 mm/s. The rate of frequency change of the friction force increased in both the results under a magnetic field. The variation amplitude of the friction force also increased, as shown in Fig. 7(d). The stick-slip decreased obviously under high velocity with a magnetic field.

Table 3 shows the average friction force and SD from the results in Fig. 7. The friction force is reduced by about 20% when the magnetic field is applied. The magnetic field is not applied at the start of the test, but is applied in the middle of the test. The contact area is constant and the hardness of the MRE increases in the later part of the tests. Therefore, the friction force is decreased when a magnetic field is applied. The SD with a magnetic field is similar to that without a magnetic field under the low velocity conditions. Under the high velocity conditions, the SD with a magnetic field is clearly smaller than that without a magnetic field. It is shown that the stick-slip is significantly reduced with a magnetic field under a high velocity condition.

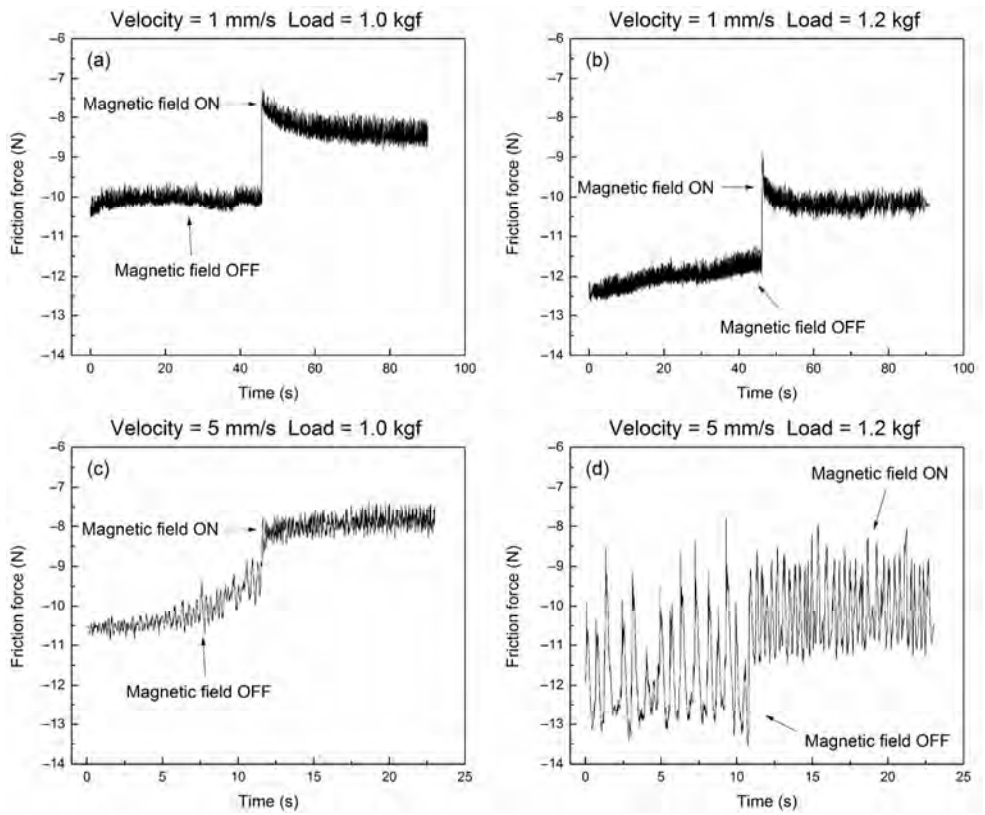

Fig. 7 Results of friction force tests: (a), (b) velocity 1 mm/s, load 1.0 and 1.2 kgf, respectively; (c), (d) velocity 5 mm/s, load 1.0 and 1.2 kgf, respectively.

Table 3 Average friction force and SD of tests a–d of Fig. 7.

Test No.	Average friction force (N)		Standard deviation	
	Magnetic field OFF	Magnetic field ON	Magnetic field OFF	Magnetic field ON
a	10.08	8.47	0.131	0.192
b	12.00	10.19	0.179	0.170
c	10.14	7.85	0.409	0.186
d	11.87	10.06	1.025	0.791

Figure 8 shows the FFT of the stick-slip and that of the aluminum plate surface roughness. The roughness is measured with a two-dimensional surface roughness measuring instrument (SV-3100S4 Mitutoyo). The results confirmed that the stick-slip result (Fig. 8(b)) is not directly related to the surface roughness of the aluminum plate (Fig. 8(a)). The surfaces of the MREs after the stick-slip tests were observed with an optical microscope to evaluate the wear with and without a magnetic field. Figures 9(a)–9(f) show surface images of the MREs for test conditions of 10 mm/s with 1.0 kgf, 1 mm/s with 1.0 kgf, and 1 mm/s with 1.2 kgf, respectively, whose SDs have relatively large gaps between the conditions with and without a magnetic field.

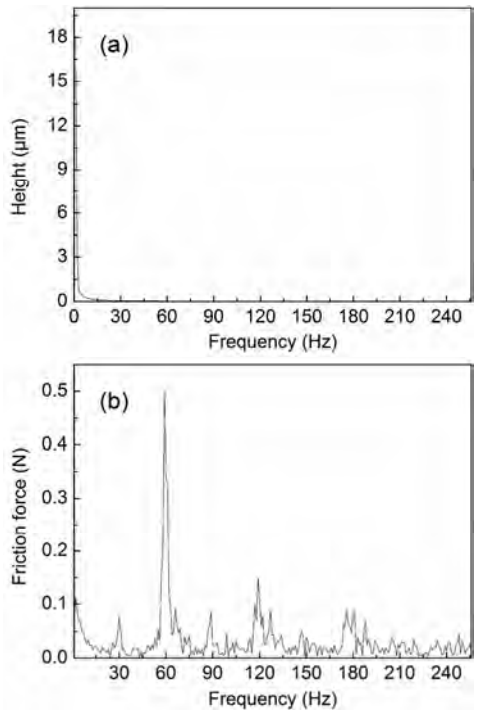

Fig. 8 (a) FFT of the aluminum plate surface roughness; (b) FFT of the stick-slip.

Figures 9(a) and 9(b) show surface images of the MRE under conditions of 10 mm/s and 1.0 kgf, without and with a magnetic field, respectively. The Schallamach waves [23–26] were more obvious without the magnetic field than those with the magnetic field. Figure 9(c) shows slightly heavy wear compared to Fig. 9(d), which was obtained with a magnetic field. A wear hole was found in Fig. 9(e), and the Schallamach waves were more obvious than those in Fig. 9(f), which was obtained with a magnetic field. In general, the wear of the elastomer is related to the friction force for the same material. More friction force corresponds to more wear as the surface temperature increases. The friction force increases under a magnetic field, and the wear should be more obvious than that without a magnetic field. However, the tests show the opposite results. It is assumed that the stick-slip results in wear and is reduced when a magnetic field is applied.

5 Conclusions

Stick-slip can lead to vibration, noise, wear, and reduce the lifetime of friction pairs. For this reason, the stick-slip should be reduced as much as possible. The MRE is a type of smart material that can change its properties under an external magnetic field. This property can be used to change the stick-slip to replace other materials.

In this paper, the MRE was manufactured, and a stick-slip tester was used to evaluate the stick-slip under different velocities and load conditions with and without a magnetic field. The results show that at lower velocity, the stick-slip was smaller, while at higher velocity, the reduction of the stick-slip under a magnetic field was more obvious. The change of the friction force was more stable under a magnetic field. The FFT of the friction force of stick-slip and the aluminum plate surface roughness were calculated to determine that the stick-slip phenomenon is not directly caused by the roughness of the aluminum plate under low velocity conditions. The wear surfaces were observed after the tests, and the results showed that the wear can be reduced when the stick-slip is reduced under a magnetic field. Based on this study, the MRE could potentially be applied to a wide range of various

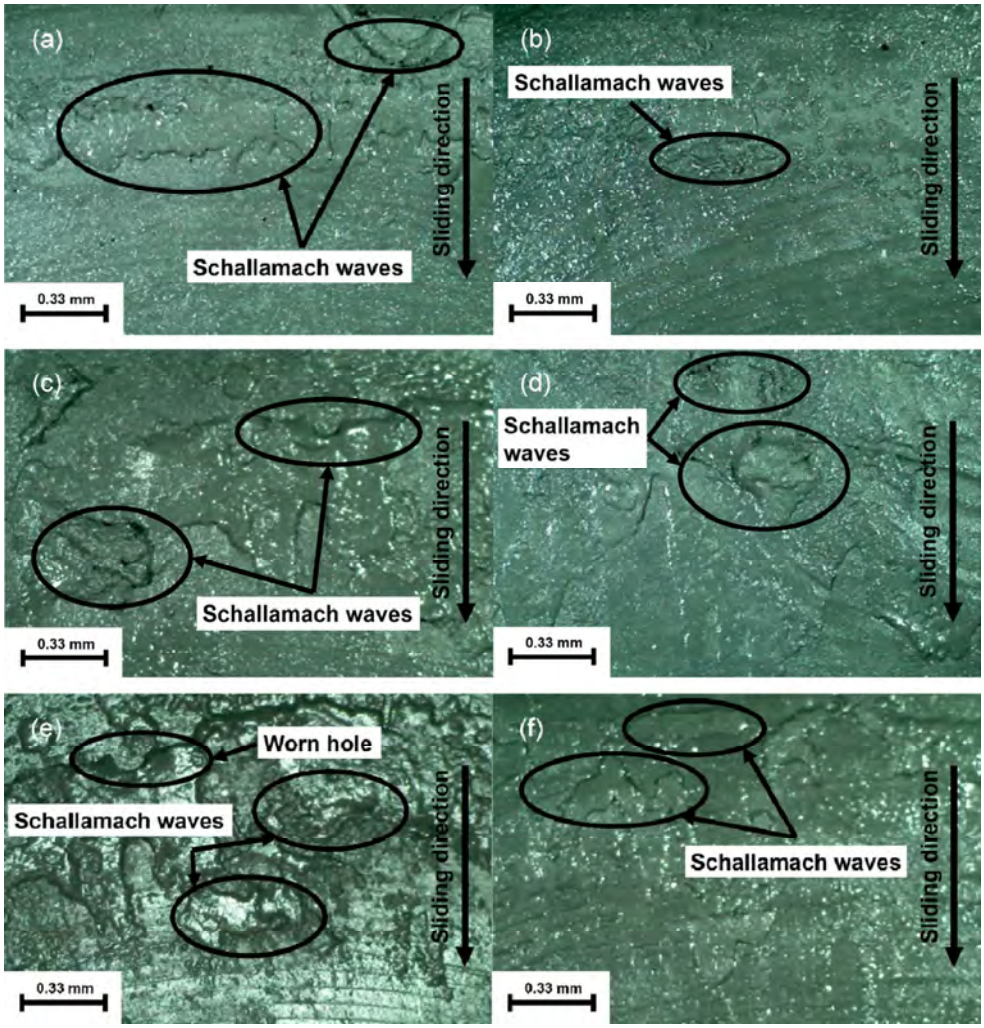

Fig. 9 Surface state images after tests: (a), (b) 10 mm/s, 1 kgf without and with a magnetic field; (c), (d) 1 mm/s, 1 kgf without and with a magnetic field; (e), (f) 1 mm/s, 1.2 kgf without and with a magnetic field.

industrial and automotive systems under realistic conditions in future work (e.g., taxiing distance control pad). This study may be used as a reference for the tribology studies of the MRE.

Acknowledgement

This research was supported by the Basic Science Research Program of the National Research Foundation of Korea (NRF) funded by the Ministry of Education, Science and Technology of the Korean government (Grant No. NRF-2015R1D1A1A09060901) and Ministry of Trade, Industry and Energy via FY 2015 Korea Institute for the Advancement of technology through Construction Machine R&D Expert Cultivation Program.

References

[1] Ginder J, Clark S, Schlotter W. Magnetostrictive phenomena in magnetorheological elastomers. *Int J Mod Phys B* **16**(17−18): 2412–2418 (2002)

[2] Deng H, Gong X. Application of magnetorheological elastomer to vibration absorber. *Community Nonlinear Sci Numer Simul* **13**(9): 1938–1947 (2008)

[3] Shen Y, Golnarachi M, Heppler G. Experimental research and modeling of Magnetorheological Elastomers. *J Intell Mater Syst Struct* **15**(1): 27–35 (2004)

[4] Wang Y, Wang G. Study on the mechanical properties of magnetorheological elastomers. *Adv Mater Res* **774**(1): 54–57 (2013)

[5] Liao G, Gong X, Xuan S, Kang C, Zong L. Development of a real-time tunable stiffness and damping vibration isolator based on magnetorheological elastomer. *J Intell Mater Syst Struct* **23**(1): 25–33 (2012)

[6] Lee D, Lee K, Lee C, Kim C, Cho W. A study on the tribological characteristics of a magneto-rheological elastomer. *Trans ASME, J Tribol* **135**(1): 014501–1 (2013)
[7] Lian C, Lee K, LEE C. Friction and wear characteristics of magneto-rheological elastomers based on silicone/polyurethane hybrid. *Trans ASME, J Tribol* **137**(3): 031607 (2015)
[8] Bica I, Anitas E, Averis L. Influence of magnetic field on dispersion and dissipation of electric field of low and medium frequencies in hybrid magnetorheological suspensions. *J Ind Eng Chem* **27**: 334–340 (2015)
[9] Bunoiu M, Bica I. Magnetorheological elastomer based on silicone rubber, carbonyl iron and Rochelle salt: Effects of alternating electric and static magnetic fields intensities. *J Ind Eng Chem* **37**: 312–318 (2016)
[10] Balasoiu M, Bica I. Composite magnetorheological elastomers as dielectrics for plane capacitors: Effects of magnetic field intensity. *Results in Physics* **6**: 199–202 (2016)
[11] Karnopp D. Computer simulation of stick-slip friction in mechanical dynamic systems. *J Dyn Syst Meas Control* **107**(1): 100–103 (1985)
[12] Dieterich J. Time-dependent friction and the mechanics of stick-slip. *Pure and Applied Geophysics* **116**(4): 790–806 (1978)
[13] Mora P, David P. Simulation of the frictional stick-slip instability. *Pure and Applied Geophysics* **143**(1): 61–87 (1994)
[14] Maegawa S, Ken N, Mechanism of stick-slip associated with Schallamach waves. *Wear* **268**(7): 924–930 (2010)
[15] Fukahori Y, Gabriel P, Busfield J. How does rubber truly slide between Schallamach waves and stick–slip motion? *Wear* **269**(11): 854–866 (2010)
[16] Tristan B, Caroli C. Solid friction from stick–slip down to pinning and aging. *Adv Phys* **55**(3): 279–348 (2006)
[17] Owen W S, Croft E A. The reduction of stick-slip friction in hydraulic actuators. Mechatronics. *IEEE/ASME Trans* **8**(3): 362–371 (2003)
[18] Marton L, Lantos B. Modeling, identification, and compensation of stick-slip friction. *Ind Electron, IEEE Trans* **54**(1): 511–521 (2007)
[19] Leine R, Van campen D, Keultjes W. Stick-slip whirl interaction in drillstring dynamics. *J Vib Acoust* **124**(2): 209–220 (2002)
[20] Wen S, Huang P. *Principles of Tribology*. Tsinghua University Press, 2008.
[21] Bose H. Viscoelastic properties of silicone-based magnetorheological elastomers. *Int J Mod Phys B* **21**(28): 4790–4797 (2007)
[22] Persson B. Theory of rubber friction and contact mechanics. *J Chem Phys* **115** (8): 3840–3861 (2004)
[23] Schallamach A. The velocity and temperature dependence of rubber friction. *Proc Phys Soc* **66**(5): 386 (1953)
[24] Maegawa S, Nakano K. Mechanism of stick slip associated with Schallamach waves. *Wear* **268**(7): 924–930 (2010)
[25] Heise R. Friction between a temperature dependent viscoelastic body and a rough surface. *Friction* **4**(1): 50–64 (2016)
[26] Liu M, Wu L, Zhang F, Fu J. Influence of molecular weight of modified ultrahigh-molecular-weight polyethylene with Cu(II) chelate of bissalicylaldehydeethylenediamine on wear-resistant materials. *Friction* 4(2): 116–123 (2016)

Chenglong LIAN. He received his bachelor degree in mechanical engineering in 2011 from Howon University, Korea. Now, he is a Ph.D. student in the Advanced Vehicle Design and Control Laboratory of Inha University, Korea. His research interests include tribology of smart material and friction control.

Chul-hee LEE. He received his bachelor and master degrees in mechanical engineering from Inha University, Korea, in 1994 and 1996, respectively. After then, he received his Ph.D. degree from Mechanical and Industrial Engineering of University of Illinois at Urbana-Champaign, USA, in 2006. His current position is a professor and the director of Advanced Vehicle Design and Control Laboratory. His research area covers the transportation vehicle components design and controls, tribology, structural FE analysis and optimization, vehicle dynamic and vibration analysis, and smart system design and control.

Friction **5**(4): 392–401 (2017)
DOI 10.1007/s40544-017-0153-y
ISSN 2223-7690
CN 10-1237/TH
RESEARCH ARTICLE

Surface roughness characteristics effects on fluid load capability of tilt pad thrust bearings with water lubrication

Yuechang WANG, Ying LIU*, Zhanchao WANG, Yuming WANG
State Key Laboratory of Tribology, Tsinghua University, Beijing 100084, China
Received: 15 November 2016 / Revised: 15 January 2017 / Accepted: 10 February 2017

Abstract: The effects of surface roughness characteristics on the fluid load capacity of tilt pad thrust bearings with water lubrication were studied by the average flow model. The flow factors utilized in the average flow model were simulated with various surface roughness parameters including skewness, kurtosis and the roughness directional pattern. The results indicated that the fluid load capacity was not only affected by the RMS roughness but also by the surface roughness characteristics. The fluid load capacity was dramatically affected by the roughness directional pattern. The skewness had a lower effect than the roughness directional pattern. The kurtosis had no notable effect on the fluid load capacity. It was possible for the fluid load capacity of the tilt pad thrust bearings to be improved by the skewness and roughness direction pattern control.

Keywords: tilt pad thrust bearings; characteristics of surface roughness; average flow model; water lubrication

1 Introduction

The tilt pad thrust bearings lubricated by oil are widely utilized. The high viscosity of oil is beneficial for the fluid load capacity of bearings improvement. Besides, the non-renewable resource and environmental pollution of oil received a lot of attention. These problems could be solved by water utilization which is an environment friendly lubricant. In contrast, the viscosity of water is lower than oil, which would reduce the fluid load capacity. As the lubrication film is reduced, the surface roughness effect could not be ignored.

Two typical methods exist, which could be utilized for the evaluation of surface roughness effects on lubrication. The first method is the stochastic method. Tzeng and Saibel [1] introduced the stochastic method by the surface roughness treatment as a random variable characterized by a probability distribution function. The one-dimensional surface roughness was considered by a high amount of works based on the stochastic method [2–5]. Patir and Cheng [6–8] derived an average flow model, where the Reynolds equation was modified by coefficients called flow factors for the effects of two-dimensional surface roughness introduction. The average flow model was utilized for the average film thickness distribution and average pressure distribution predictions. This model was also labeled as the PC average flow model and has been widely adopted [9–11]. The flow factors utilized in these works were calculated by the fitting formula of the isotropic Gaussian surface provided by Patir and Cheng, where the effects of skewness, kurtosis and roughness directional pattern were ignored [6, 7]. Besides, the skewness, kurtosis and roughness directional pattern are changeable according to the different manufacture methods and wear of the surface. These parameters might affect the performance of water lubrication.

The second method is the deterministic. The surface roughness data are directly utilized in the Reynolds equation solution. Both the specific pressure and thickness distributions of lubrication films are simulated by the deterministic method. The deterministic method

* Corresponding author: Ying LIU, E-mail: liuying@mail.tsinghua.edu.cn

List of symbols

ϕ_x, ϕ_y	pressure flow factor	(R_p, θ_p)	Position of the tilt pad pivot
ϕ_s	shear flow factor	k_r	Radial support ratio
μ	viscosity of water	k_θ	Circumferential support ratio
h	nominal gap	α	Circumferential inclination of the tilt pad
$\bar{h}_T$	average gap considering surface roughness	β	radial inclination of the tilt pad
$\bar{p}$	average film pressure	h_0	Film thickness at the pivot position
U_1, U_2	velocity of moving part	n	Rotational velocity of the thrust collar
σ	combined roughness variance	W	load of one tilt pad
Sk	rough surface skewness	p_0	Reference pressure
Ku	rough surface kurtosis	F_{film}	Force generated by the film
γ	roughness directional pattern parameter	ε_F	Convergence index of the force
R_i	Inner radius of the tilt pad	M	Moment of the pressure distribution on the pivot
R_o	Outer radius of the tilt pad		
θ_s	Wrap angle of the tilt pad		

is often utilized for the lubrication problems solution with well-defined geometrical features [12, 13] or the point and line contact condition [14–16]. In contrast, the deterministic method utilization for surface contact problems solution, such as in the case of bearings is rare [17].

The researches regarding the effects of roughness on bearings were often focused on fixed pad bearings [17, 18]. The effects of roughness on tilt pad bearings are rare. In this paper, the PC average flow model was utilized for the surface roughness effects study on tilt pad thrust bearings. The effects of surface parameters, skewness, kurtosis and roughness directional pattern, were also considered. The corresponding flow factors were computed by the numerical model and fitted by the cubic spline interpolation. Finally, the fluid load capacity of tilt pad thrust bearing provided with various surface roughness parameters were discussed.

2 Experimental procedure

2.1 Computation of flow factors

The key point of the numerical simulation method proposed by Patir [6, 7] was the flow factors utilization with consideration to the surface roughness effects. The modified Reynolds equation proposed by Patir and Cheng [6] is:

$$\frac{\partial}{\partial x}\left(\phi_x \frac{h^3}{12\mu}\frac{\partial \bar{p}}{\partial x}\right)+\frac{\partial}{\partial y}\left(\phi_y \frac{h^3}{12\mu}\frac{\partial \bar{p}}{\partial y}\right)=\frac{U_1+U_2}{2}\frac{\partial \bar{h}_T}{\partial x}+\frac{U_1-U_2}{2}\sigma\frac{\partial \phi_s}{\partial x}+\frac{\partial \bar{h}_T}{\partial t} \quad (1)$$

where, ϕ_x and ϕ_y are the pressure flow factors representing the effects of roughness on the pressure flow in both perpendicular directions x and y. Also, ϕ_s is the shear flow factor representing the effects of roughness on the shear flow produced by the relative motion. In Eq. (1), x is the direction of relative motion. μ is the viscosity of the lubricant. h is the nominal gap and $\bar{h}_T$ is the average gap considering surface roughness. $\bar{p}$ is the average film pressure. U_1 and U_2 are the velocities of the two parts respectively. σ is the comprehensive roughness of the two rough surfaces defined as:

$$\sigma^2=\sigma_1^2+\sigma_2^2 \quad (2)$$

where, σ_1 and σ_2 are the RMS roughness of the two surfaces respectively.

In order for the ϕ_x, ϕ_y and ϕ_s to be evaluated, a bearing model with a roughness was proposed (Fig. 1). The area of the bearing was low enough for the nominal film thickness to be assumed as constant, whereas it was high enough for a high number of asperities to be included. The pressure and shear flow factors were simulated respectively by this model [6, 7].

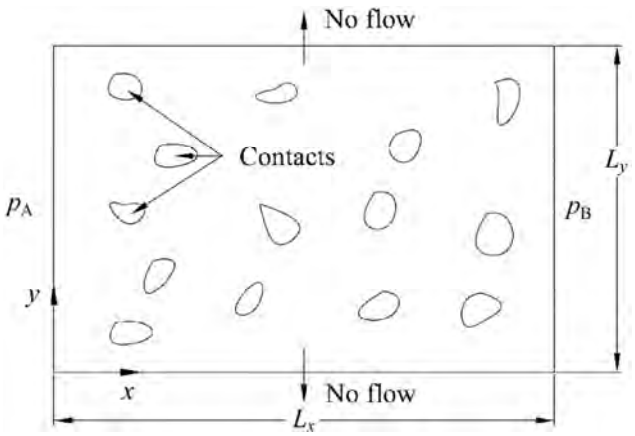

Fig. 1 Bearing model for flow factors simulation.

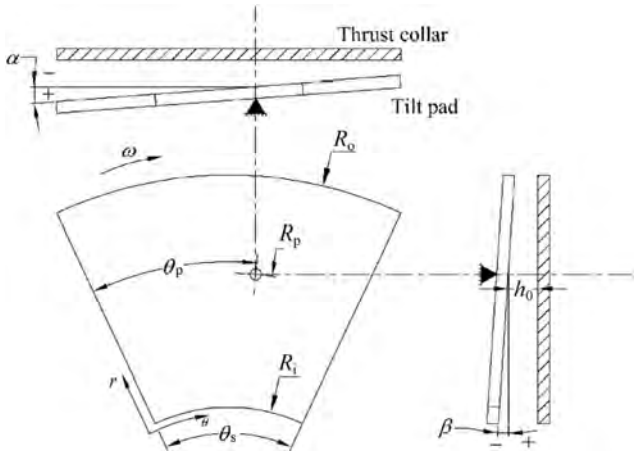

Fig. 2 Geometry model of the tilt pad.

Patir [6, 7] reported that both the pressure and shear flow factors were a function of the h/σ and γ. γ is the parameter of the roughness directional pattern, associated with the decay lengths of the surface autocorrelation function. When $\gamma > 1$, roughness occurs along the fluid flow direction, possibly enhancing the flow. When $\gamma < 1$ was opposite, roughness occurs along the perpendicular direction of flow, which could hinder the flow. When $\gamma = 1$, roughness was isotropic.

The rough surface utilized for the flow factors computation was generated numerically. The quality of the generated rough surfaces determined the validation of the flow factors. Patir [19] utilized a one order moving average (MA) model for surface roughness generation. This method was good at Gaussian surfaces generation, whereas not convenient for non-Gaussian surfaces simulation. The modified MA model proposed by Minet [20] was utilized here for the required surface roughness generation.

2.2 Performance analysis of tilt pad thrust bearings

Geometry model

The geometry model of a tilt pad is presented in Fig. 2. The tilt pad was the offset support and the pivot position was (R_p, θ_p). h_0 is the film thickness at the position of pivot. The attitude of the tilt pad was determined by the tilt angles α and β in the circumferential and radial directions. The film thickness distribution is:

$$h = h_0 + r\sin(\theta_p - \theta)\tan\alpha + (r - R_i - R_p)\cos(\theta_p - \theta)\tan\beta \tag{3}$$

Kinematic model

The PC average flow Reynolds equation in the cylindrical coordinate system was utilized. The squeeze effect of lubrication film was ignored:

$$\frac{\partial}{r\partial r}\left(r\phi_r h^3 \frac{\partial \bar{p}}{\partial r}\right) + \frac{1}{r^2}\frac{\partial}{\partial \theta}\left(\phi_\theta h^3 \frac{\partial \bar{p}}{\partial \theta}\right) = 6\mu\omega\frac{\partial \bar{h}_T}{\partial \theta} + 6\mu\omega\sigma\frac{\partial \phi_s}{\partial \theta} \tag{4}$$

where, ω is the angular velocity.

Boundary conditions

In order for the computation to be simplified, the surface of the thrust collar was assumed to be smooth. The tilt pad surface was rough and the corresponding RMS roughness is σ. The load on one tilt pad was constant represented by the W. The pressure boundaries of the four edges of tilt pad were assumed as $p_0 = 0$.

Computational scheme

The flow chart of the simulation is presented in Fig. 3. The flow factors were calculated parametrically and fitted by the cubic spline interpolation. The average flow Reynolds equation was discretized by the finite difference method. The grid size was 50 × 50. The discrete equation was solved by the Gauss elimination. The pivot film thickness and tilt angles were adjusted for the force and moment balance.

The film force generated by the film between the thrust collar and one tilt pad is:

$$F_{film} = \int_A \bar{p}\mathrm{d}A \tag{5}$$

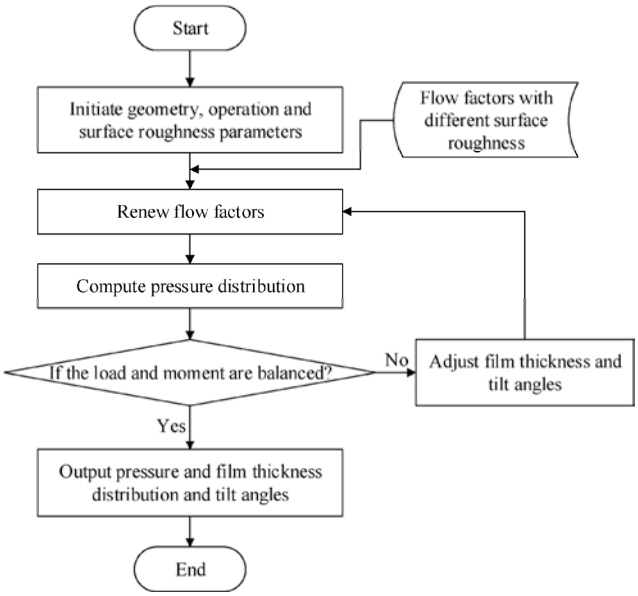

Fig. 3 Flow chart of the tilt pad thrust bearing simulation.

where, F_{film} is the film force, A is the area of the tilt pad surface. The F_{film} should be equal to the load W. The convergence index of force is presented in Eq. (6). If the force is not converged, the pivot film thickness (h_0) is updated by the relaxation method. When the force is balanced, the pivot film thickness (h_0) provides mainly the fluid load capacity of the tilt pad thrust bearing:

$$\varepsilon_F = \left| \frac{F_{film} - W}{W} \right| < 1\times10^{-4} \tag{6}$$

The pressure center of the film pressure distribution should be at the pivot position. Therefore, the moment of the pressure distribution on the pivot (Eq. (7)) should be equal to zero:

$$\boldsymbol{M} = \int_A \overline{p} \times (\boldsymbol{r} - \boldsymbol{r}_p) \mathrm{d}A \tag{7}$$

where, $\boldsymbol{M}$ is the moment vector, $\boldsymbol{r}$ is the position vector of pressure distribution, $\boldsymbol{r}_p$ is the position vector of the pivot. The convergence index of the moment is presented in Eq. (8). If the moment is not converged, the attitude of the tilt pad (α and β) is updated by the Newton-Raphson method. The initial value of $\boldsymbol{r}$ affects the value of both α and β. If the moment is balanced, the attitude of the tilt pad (α and β) mainly provides the value of the $\boldsymbol{r}$ determined by the initial input parameters.

$$\left\| \boldsymbol{M} \right\| < 1\times10^{-4} \tag{8}$$

3 Results and discussion

The surface roughness parameters utilized for the calculation of the flow factors are presented in Table 1. The roughness directional pattern characteristic γ was set to 1/9, 1/6, 1/3, 1, 3, 6, 9 for each group of parameters in Table 1, respectively. The geometric parameters of the tilt pad thrust bearing and operation parameters are presented in Table 2.

Table 1 Surface roughness parameters for flow factors calculation.

Group number	Surface skewness (Sk)	Surface kurtosis (Ku)
1	0.5	4.83
2	1	4.83
3	1.5	4.83
4	1	6
5	1	25

Table 2 Geometric parameters of the tilt pad thrust bearing and operation parameters.

Item	Value
Outer radius R_o (mm)	70
Inner radius R_i (mm)	30
Tilt pad wrap anlge q_s (°)	50
Pivot radius R_p (mm)	53
Radial support ratio k_r	0.575
Pivot wrap angle q_p (°)	30
Circumferential support ratio k_q	0.6
Viscosity of water m (Pa·s)	549.4×10^{-6}
Rotational velocity of thrust collar n (rpm)	100
Load W (N)	60
Reference pressure p_0 (MPa)	0

3.1 Flow factors

In order for the program utilized in this paper to be verified, the flow factors of the Gaussian roughness (Sk = 0, Ku = 3) with the γ = 1 were computed. It was noted that the twenty-surfaces with the same roughness characteristic were utilized for the flow factors calculation and each flow factor value was the average of these solutions. The results were compared to the results of Patir's formula (Fig. 4). Both the ϕ_x and ϕ_s computed in this paper had the same tendency,

whereas differed at the specific values with Patir's results. The maximum relative error of ϕ_x was 43% at the $h/\sigma = 0.5$. When the h/σ was low, the deviation between the current ϕ_x and Patir's value might have occurred due to the inherent fluctuation of the numerical simulation of the ϕ_x [21]. The maximum relative error of the ϕ_s was 5.5% at the $h/\sigma = 4$.

3.2 Fluid load capacity analysis of the tilt pad bearing

3.2.1 The surface skewness effects

The tilt angles, α and β, the pivot film thickness, h_0, with various Sk and constant Ku and γ, are presented in Fig. 5.

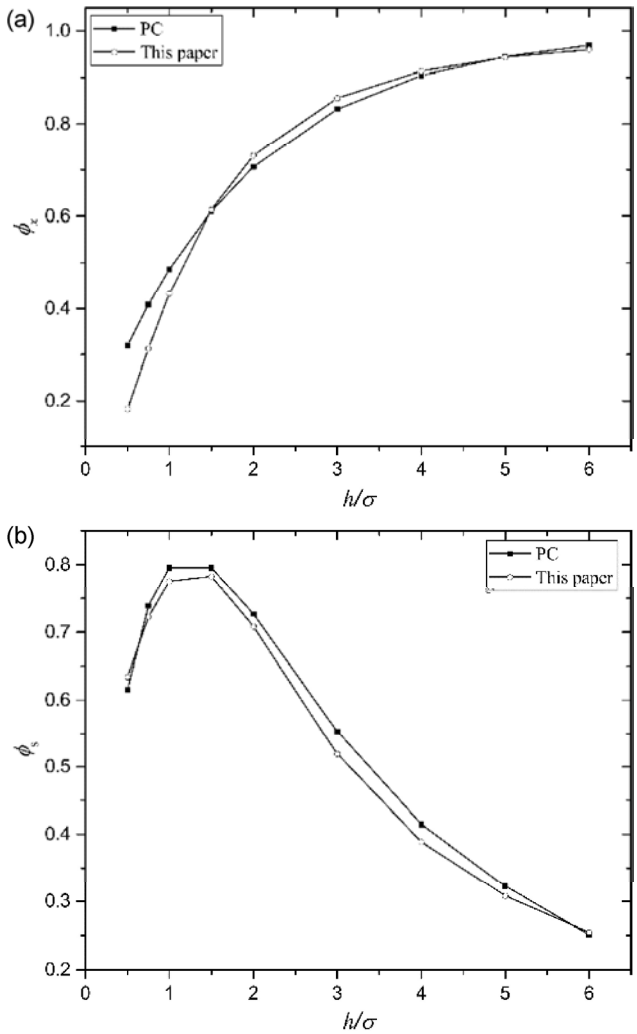

Fig. 4 Comparison of computed flow factors and Patir's results Sk = 1, Ku = 3, $\gamma = 1$. (a) Pressure flow factors, (b) shear flow factors.

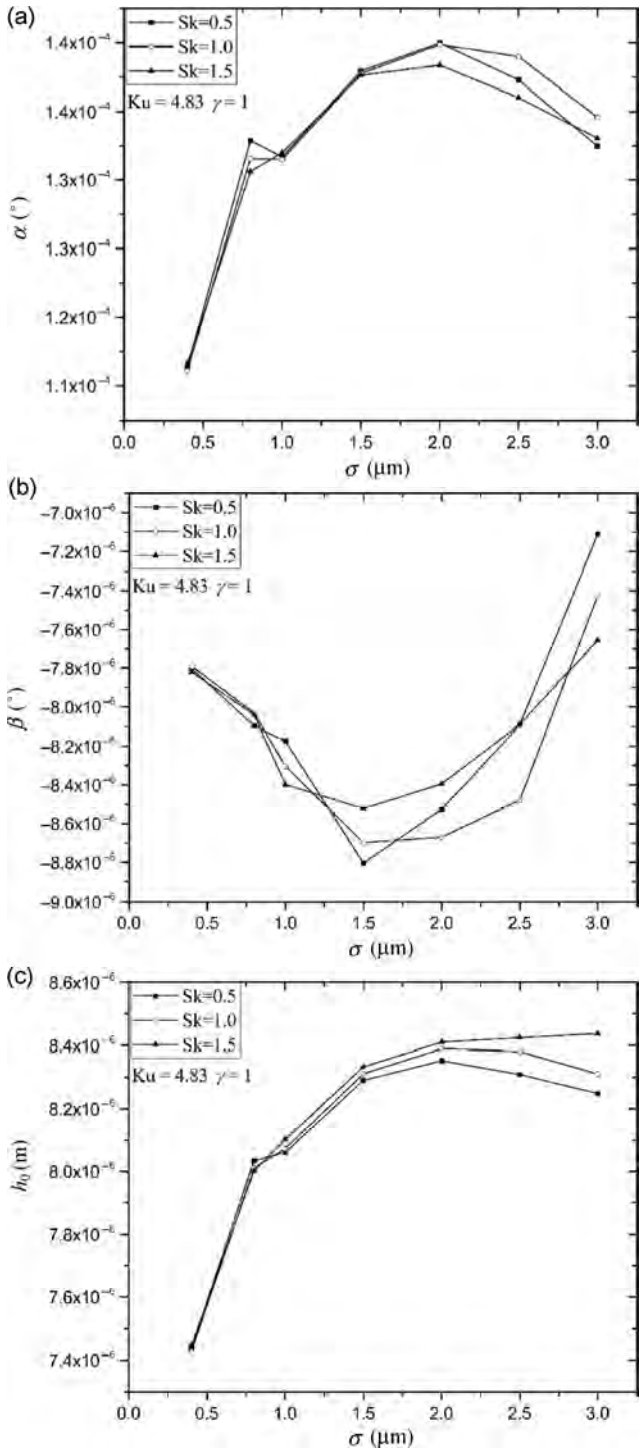

Fig. 5 Tilt angles, α and β, and pivot film thickness, h_0, with various Sk. Ku = 4.83 $\gamma = 1$ (a) α v.s. σ, (b) β v.s. σ, (c) h_0 v.s. σ.

As the σ increased from 0.4 to 3, the h_0 increased first and following decreased (Fig. 5(c)), indicating that the fluid load capacity increased first and consequently decreased. Therefore, a proper σ existed which could improve the fluid load capability mostly.

Along with the increase of σ, the α increased first and following decreased, whereas β decreased first and following increased. This demonstrated that the initial pressure center position shifted away firstly from the pivot position and consequently shifted towards the pivot position in the positive direction of the both radial and circumferential axes, as the σ increased.

As the Sk increased from 0.5 to 1.5, the effects of skewness on the α (β or h_0) changed based on various σ. The effects were stronger when the σ was higher. A unified relation between the skewness and α and β with various σ did not exist. Besides, as the Sk increased, the h_0 increased, indicating that the fluid load capacity was improved by the skewness increase, because the skewness indicated the peaks and valleys distribution of a rough surface. When the skewness became higher, the number of the roughness deep valleys became higher, which augmented the flow and improved the fluid load capacity.

The result of average fluid pressure distributions with various skewness values indicated that the skewness had no significant effect on the average fluid pressure distribution (Fig. 6). This occurred because the force and moment were balanced by the tilt pad under the same load.

3.2.2 *Surface kurtosis effects*

The tilt angles, α and β and the pivot film thickness, h_0, with various Ku and constant Sk and γ, are presented in Fig. 7.

As the Ku varied, the effects of kurtosis on the α (β or h_0) were also changed along with various σ. The effects were stronger when the σ was higher, whereas the effects were lower than the effects of skewness with the same σ. A unified relation between the kurtosis and the α (β or h_0) with various σ did not exist. The alteration of the h_0 was low when various kurtosis values were considered. Therefore, a low effect of kurtosis existed on fluid load capacity. The kurtosis measured the spikiness of a rough surface height distribution, which had lower effects on the flow condition than the skewness. The average fluid pressure distributions are not influenced by kurtosis either (Fig. 8).

3.2.3 *γ effects*

The tilt angles, α and β, and the pivot film thickness, h_0, with various γ and constant Sk and Ku, are presented in Fig. 9.

When the $\sigma \geqslant 1.5$, the α (β or h_0) increased as the γ increased. The flow in the circumferential direction was gradually enhanced along with the increase of γ. The initial pressure center position shifted away from the pivot position in the positive direction of the circumferential axis and in the negative direction of the radial axis, as the γ increased. The fluid load capacity was improved by γ increase when the $\sigma\varepsilon \geq 1.5$.

When the $\sigma < 1.5$, α (β or h_0) increased as the γ

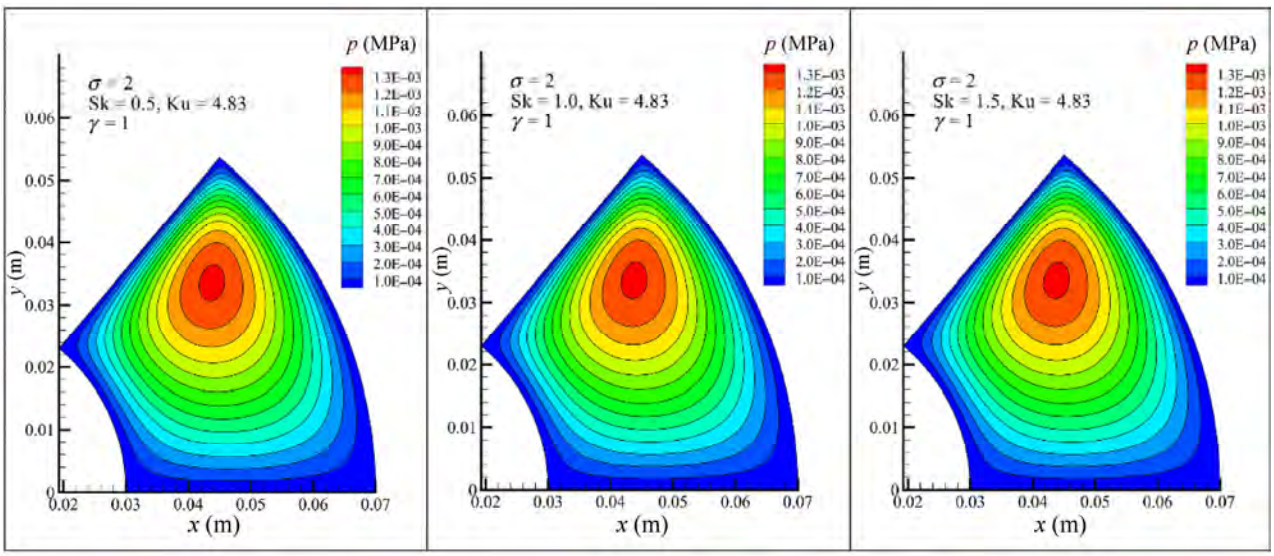

Fig. 6 Average fluid pressure distributions with various Sk. Ku = 4.83, $\gamma = 1$.

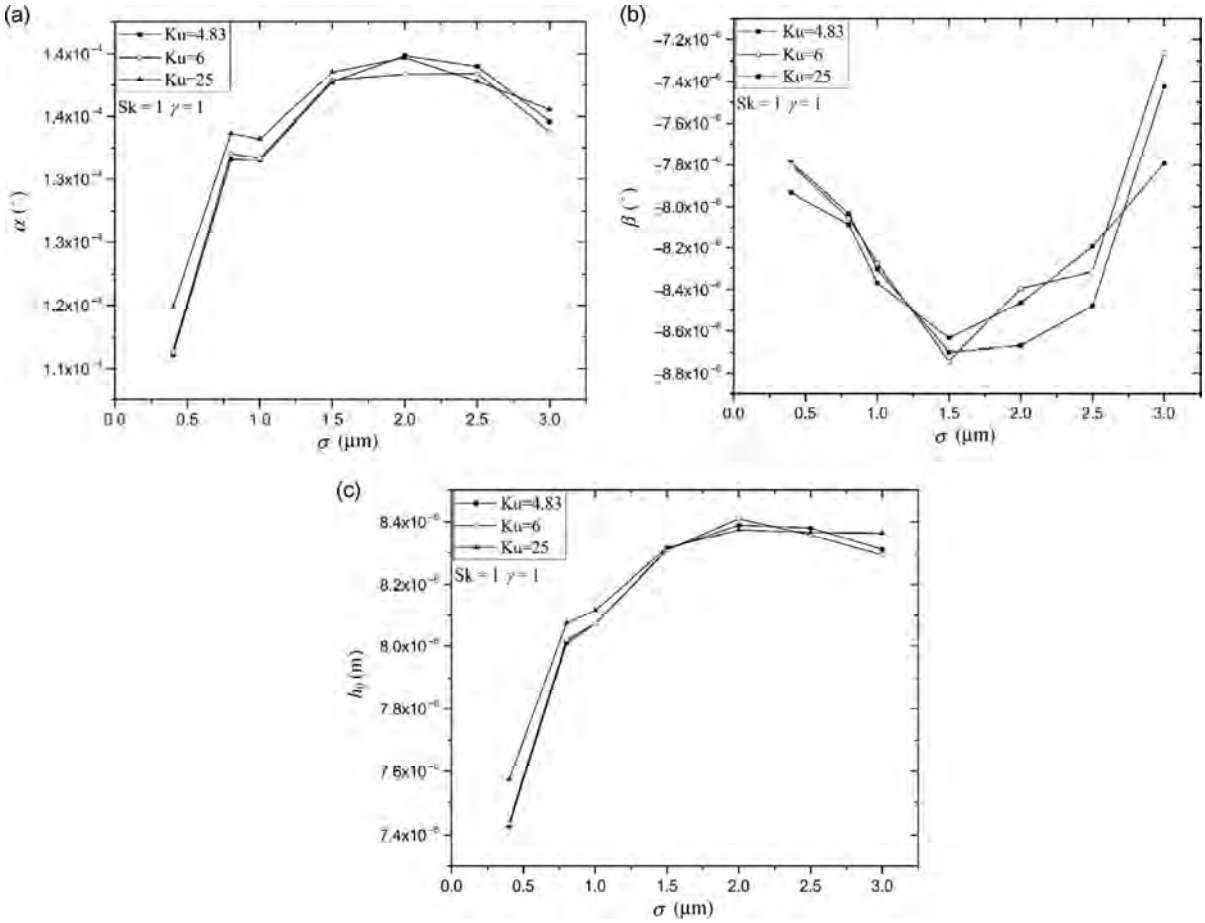

Fig. 7 Tilt angles, α and β, and pivot film thickness, h_0, with various Ku. (a) α v.s. σ; (b) β v.s. σ; (c) h_0 v.s. σ. Sk = 1, γ = 1

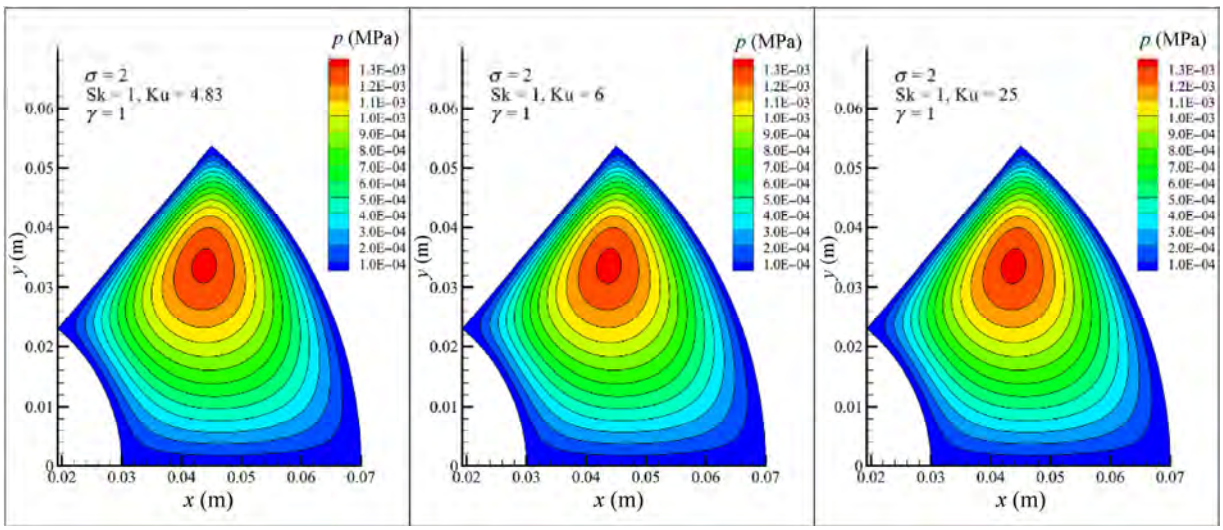

Fig. 8 Average fluid pressure distributions with various Ku. Sk = 1, γ = 1.

decreased. The surface roughness with a low γ was equal to the "waviness" in the circumferential direction when the $\sigma < 1.5$. The flow in the circumferential direction was enhanced by the hydrodynamic effect of the "waviness". Therefore, the fluid load capacity was improved by the decrease of γ when the $\sigma < 1.5$. The average fluid pressure distributions were not affected by the γ either (Fig. 10).

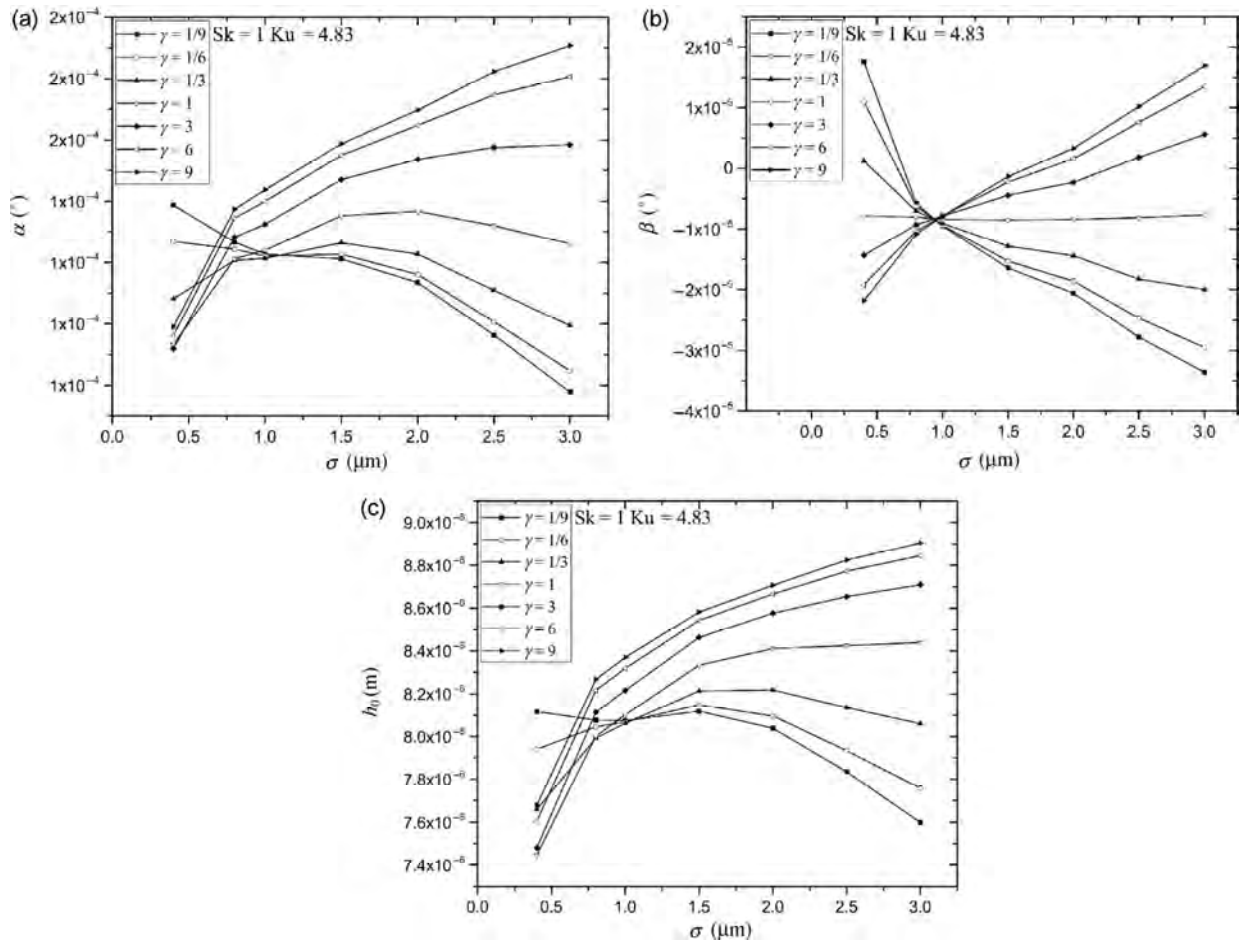

Fig. 9 Tilt angles, α and β, and pivot film thickness, h_0, with various γ. (a) α v.s. σ; (b) β v.s. σ; (c) h_0 v.s. σ. Sk = 1, Ku = 4.83

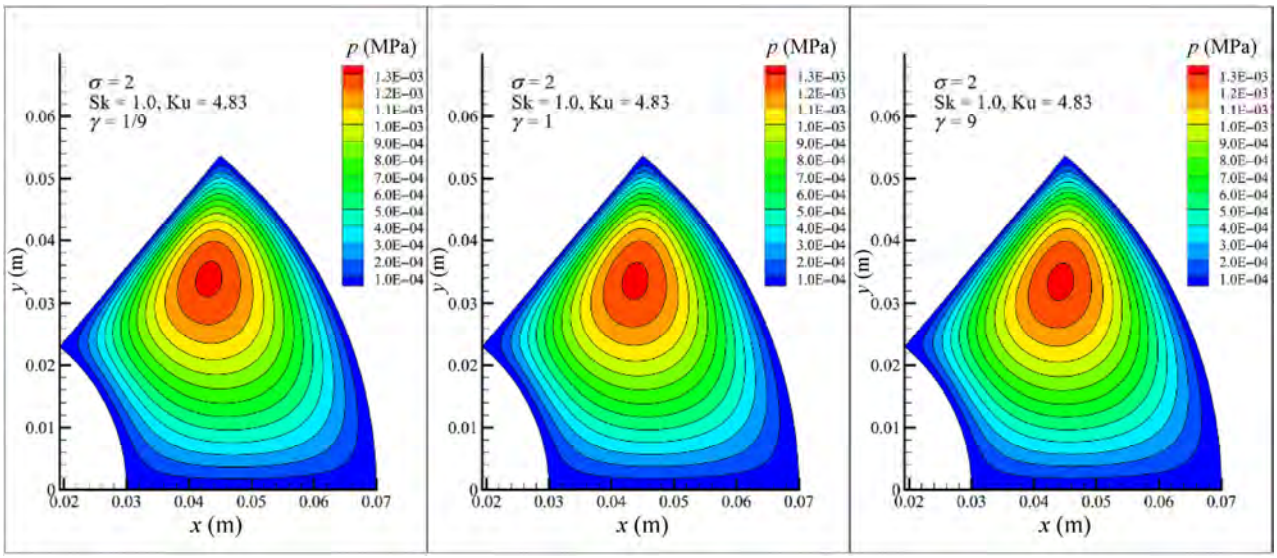

Fig. 10 Average fluid pressure distributions with various γ. Sk = 1, Ku = 4.83.

4 Conclusions

The surface roughness characteristics effects on the fluid load capability of tilt pad thrust bearings during water lubrication were studied by the PC average Reynolds equation. The flow factors were computed based on the skewness, kurtosis and roughness directional pattern with various roughness surfaces. It could be concluded that:

(1) The fluid load capacity was not only affected by the RMS roughness, whereas also by the surface roughness characteristics.

(2) The roughness directional pattern had a significant effect on the fluid load capacity of the tilt pad thrust bearing. The fluid load capacity was improved by the increase of γ when the $\sigma \geqslant 1.5$ and by the decrease of γ when the $\sigma < 1.5$.

(3) The skewness had a lower effect than the roughness directional pattern. The fluid load capacity was improved by the skewness increase. The kurtosis had no notable effect on the fluid load capacity.

(4) Under the same load, the average fluid pressure distribution on tilt pad did not appear to be affected by the skewness, kurtosis and roughness directional pattern.

Acknowledgements

This work was supported by the National Basic Research Program of China (973) (No. 2015CB057303) and the National Natural Science Foundation of China (No. 51275268).

References

[1] Tzeng S T, Saibel E. Surface roughness effect on slider lubrication. *ASLE Trans* **10**: 334–348 (1967)

[2] Christensen H, Tonder K. The hydrodynamic lubrication of rough bearing surfaces of finite width. *Journal of Tribology* **93**(3): 324–329 (1971)

[3] Christensen H, Tonder K. The hydrodynamic lubrication of rough journal bearings. *Journal of Tribology* **95**(2): 166–172 (1973)

[4] Chow L S H, Cheng H S. Influence of surface roughness and waviness on film thickness and pressure distribution in elastohydrodynamic contacts. NASA Contractor Report CR-2670, 1976.

[5] Chow L S H, Cheng H S. The effect of surface roughness on the average film thickness between lubricated rollers. *Journal of Tribology* **98**(1): 117–124 (1976)

[6] Patir N, Cheng H S. Average flow model for determining effects of 3-dimensinal roughness on partial hydrodynamic lubrication. *Journal of Lubrication Technology-Transactions of The ASME* **100**(1): 12–17 (1978)

[7] Patir N, Cheng H S. Application of average flow model to lubrication between rough sliding surfaces. *Journal of Lubrication Technology-Transactions of The ASME*, **101**(2): 220–230 (1979)

[8] Patir N, Cheng H S. Effect of surface roughness orientation on the central film thickness in EHD contacts. In *Proceedings-Society of Photo-Optical Instrumentation Engineers*, 1979: 15–21.

[9] Guo F, Jia X, Suo S, Salant R F, Wang Y. A mixed lubrication model of a rotary lip seal using flow factors. *Tribology International* **57**: 195–201 (2013)

[10] Zhao X Y, Liu Y, Huang W F, Liu X-F, Wang Y-M. Mechanism of second stage mechanical seal in hydrostatic seal system of nuclear coolant pumps. *Tribology* **4**: 459–467 (2014)

[11] Wen Q, Liu Y, Huang W, Suo S, Wang Y. The effect of surface roughness on thermal-elasto-hydrodynamic model of contact mechanical seals. *Science China-Physics Mechanics & Astronomy* **56**(10): 1920–1929 (2013)

[12] Burton R A. Effect of two-dimensional, sinusoidal roughness on the load support characteristics of a lubricant film. *J Bas Eng* **85**(Series D): 258–262 (1963)

[13] Davies M G. The generation of pressure between rough, fluid lubricated, moving, deformable surfaces. *Lub Eng* **19**: 246 (1963)

[14] Goglia P R, Conry T F, Cusano C. The effects of surface irregularities on the elastohydrodynamic lubrication of sliding line contacts.1.single irregularities. *Journal of Tribology-Transactions of the ASME* **106**(1): 104-112 (1984)

[15] Goglia P R, Cusano C, Conry T F. The effects of surface irregularities on the elastohydrodynamic lubrication of sliding line contacts. 2. Wavy surfaces. *Journal of Tribology-Transactions of the ASME* **106**(1): 113–119 (1984)

[16] Kweh C C, Evans H P, Snidle R W. Micro-elastohydrodynamic lubrication of an elliptical contact with transverse and three-dimensional sinusoidal roughness. *Journal of Tribology* **111**(4): 577–584 (1989)

[17] Félix Quiñonez A, Morales-Espejel G E. Surface roughness effects in hydrodynamic bearings. *Tribology International* **98**: 212-219 (2016)

[18] Li J, Zhang G, Huang Y, Chen R, Yan S, Cao H. Influence of non-Gaussian-distributed surface roughness on the static performance of slider bearings. *Tribology Transactions* in press, DOI 10.1080/10402004.2016.1208311 (2016)

[19] Patir N. Numerical procedure for random generation of rough surfaces. Wear **47**(2): 263–277 (1978)

[20] Minet C, Brunetiere N, Tournerie B, Fribourg D. Analysis and modeling of the topography of mechanical seal faces. *Tribology Transactions* **53**(6): 799–815 (2010)

[21] Patir N. Effects of surface roughness on partial film lubrication using an average flow model based on numerical simulation. Northwestern University, Evanston, 1978.

Yuechang WANG. He received his bachelor degree in mechanical engineering in 2014 from Tsinghua University, Beijing, China. After then, he is a master student in the Institute of Design Engineering (the Branch of the State Key Laboratory of Tribology) of Mechanical Engineering Department at Tsinghua University. His research interests include mixed lubrication in seals and bearings and characterization and simulation of surface topography.

Ying LIU. She received her M.S. and Ph.D degrees in mechanical engineering from Tsinghua University, China, in 1991 and 2003, respectively. She joined the Institute of Design Engineering (the Branch of the State Key Laboratory of Tribology) of Mechanical Engineering Department at Tsinghua University from 1991. Her current position is an associate professor. Her research interesting covers the design of mechanical seal system and study of water lubrication mechanism of bearings.

Friction **5**(4): 402–413 (2017)
DOI 10.1007/s40544-017-0154-x
ISSN 2223-7690
CN 10-1237/TH
RESEARCH ARTICLE

Tribological behavior of N-doped ZnO thin films by metal organic chemical vapor deposition under lubricated contacts

Bolutife OLOFINJANA[1,3,*], Uchenna Sydney MBAMARA[2], Oyelayo AJAYI[3], Cinta LORENZO-MARTIN[3], Eusebius Ikechukwu OBIAJUUWA[4], Ezekiel Oladele Bolarinwa AJAYI[1]

[1] *Department of Physics and Engineering Physics, Obafemi Awolowo University, Ile-Ife 220005, Nigeria*

[2] *Department of Physics, Federal University of Technology, Owerri, Nigeria*

[3] *Tribology Section, Energy System Division, Argonne National Laboratory, Argonne, IL 60439, USA*

[4] *Center for Energy Research and Development, Obafemi Awolowo University, Ile-Ife 220005, Nigeria*

Received: 30 July 2016 / Revised: 16 October 2016 / Accepted: 14 February 2017

Abstract: N-doped ZnO thin films were deposited on 304L stainless steel through the pyrolysis of zinc acetate and ammonium acetate in different ratios at a temperature of 420 ℃ using metal organic chemical vapor deposition. Compositional and structural analyzes of the films were performed by using Rutherford backscattering spectroscopy and X-ray diffraction. The frictional behavior of the thin films and 304L stainless steel substrate was evaluated using a ball-on-flat configuration with reciprocating sliding under marginally lubricated and fully flooded conditions. Al alloy (2017) was used as ball counterface, while basestock synthetic polyalfaolefin oil (PAO10) without additives was used as lubricant. The flat and ball counterface surfaces were examined to assess the wear dimension and failure mechanism. Under marginally lubricated condition, N-doped ZnO thin films provided significant reduction in friction, whereas the films have minimal or no effect in friction under fully flooded condition. N-doped ZnO thin films showed a significant effect in protecting the ball counterface as wear volume was reduced compared with that of the substrate under the marginally lubricated condition. Under the fully flooded condition, with the exception of one of the films, the wear volume of the N-doped ZnO thin films ball reduced compared with that of the substrate. In all the ball counterfaces for N-doped ZnO thin films under both conditions, wear occurred through abrasive mechanism of various degrees or mild polishing. Thus, superfluous lubrication of N-doped ZnO thin films is not necessary to reduce friction and wear.

Keywords: ZnO film; metal organic chemical vapor deposition; friction; wear; optical microscopy

1 Introduction

The most common friction and wear reduction approach is lubrication, which involves the application of lubricants between moving surfaces to partially or fully separate contacting surface asperities. Adequate lubrication can be achieved by the use of liquid (oils and greases), solid (thin film coatings), or gas (air bearing). Most oil lubricants used for friction and wear reduction are usually formulated with additives to improve performance [1]. Such oils normally consist of a basestock (which can be synthetic or mineral based) and additive packages. Nanoparticles and submicron particles are also good lubricant additives to improve tribological properties [2–6]. Most works on lubricant formulations are devoted to formulating the proper combination of base stock and additives for a particular or desirable function.

Thin film coatings have been considerably utilized as solid lubricants for high-precision systems such as data storage systems, semiconductor devices, MEMS, space application devices, bio-components, machining

* Corresponding author: Bolutife OLOFINJANA, E-mail: olofinb@oauife.edu.ng

tools, and bearing gears. To achieve adequate lubrication, solid lubricants in the form of thin films need to possess low shear strength to effectively carry the pressure generated between opposing surfaces, thereby reducing friction and wear. Examples of thin films used as solid lubricants are diamond-like carbon; h-BN; metal nitrides such as TiN, CrN, TiCN, and AlTiN; layered materials with covalent bonding within layers but weak bonding between layers such as MoS_2, WS_2, and TaS_2; and submicron or nanocrystalline metal oxides.

Generally, lubricious metal oxides are attractive because they typically do not form strong adhesive bonds in tribological contacts and also because they are thermodynamically stable and environmentally friendly. A typical example of these oxides is ZnO. The primary driving force behind the interest in ZnO thin films is their utility in a variety of technological applications. Their electrical, optical, and electrochemical properties, as well as their thermodynamically stable hexagonal wurtzite structure make them useful in UV-light emitting diodes, solar cells, lasers, surface acoustic wave devices, gas sensor, and photocatalytic activities, among others. In addition, several researchers have demonstrated the possible use of ZnO thin film coatings in tribological applications [7–11]. The coefficient of friction of such films is in the range of 0.15 to 0.25 with good wear life over a long cycle. Such enhanced tribological properties were attributed to the nanocrystalline nature of the ZnO films. ZnO nanoparticles have also been used as lubricant additives [12, 13]. Such ZnO nanoparticles showed excellent friction properties because of their submicrometer-scale spherical nature, which changes the contact configuration from sliding to rolling. However, because of the low hardness of such nanoparticles, their antiwear property was poor [12].

The open structure and favorable coordination number of ZnO allow ZnO to be easily doped with external atoms as zinc or oxygen substitutes, thereby permitting the formation of defects that can alter the structure and ultimately lead to improved properties. In some cases, such defects can cause the formation of slip systems that can alter the electronic structure and lower the shear strength, which can improve tribological performance. For instance, alumina-doped ZnO thin film coatings have lower friction and better wear performance than pure ZnO films [14]. The friction and wear mechanism of such doped ZnO thin films was attributed to nanocrystalline features such as the grain population and substoichiometry of the layer. The friction behavior of carbon-ZnO composite coatings was also studied by Penkov et al. [15]. They pointed out that the C–ZnO coatings demonstrated better tribological behavior compared with pure ZnO. Improvement in tribological properties was attributed to better mechanical properties. Compositing ZnO and organic polymers has also been shown to improve tribological performance and thermal stability, as well as nanochemical properties [14–19]. Furthermore, in terms of lubricant additives, compositing ZnO submicrospheres with Al_2O_3 nanoparticles had been shown to notably improve both the friction reduction and antiwear properties [20]. Such improved tribological properties were attributed to the fact that rolling friction became dominant instead of sliding friction, while the micro/nanoparticles squeezed into the grooves on the rubbing surfaces to reduce wear.

Nitrogen is considered the best candidate for doping ZnO [21]. Aside from having the smallest ionization energy among the group V elements, it also has a similar ionic radius as oxygen. Nanosized nitrigen-doped ZnO was prepared through a variety of techniques in the past. Such techniques include sol-gel method [22], microwave synthesis [23], pulsed laser deposition [24, 25], and microemulsion method [26]. Some of these techniques have different deficiencies, ranging from non-uniformity to reproducibility in composition. Techniques such as pulsed laser deposition also require a vacuum system. Over the years, metal organic chemical vapor deposition (MOCVD) has become an important technique for preparing thin films and coatings of various materials essential to advance technology because the technique requires minimum to no post-deposition processing to prepare high-quality films. Another feature of MOCVD is its versatility in coating both simple and complex components with relative ease even at low temperature.

Our group had deposited nitrogen-doped ZnO thin films on 304L stainless steel using MOCVD and explored their tribological behavior under dry contact condition [27]. However, for completeness, an evaluation

of nitrogen-doped ZnO thin films under lubricated contact is necessary because some mechanical components use oil lubrication. For effective integration of oil lubricants and nitrigen-doped ZnO thin films, an adequate understanding of interaction between the oil and the thin film is necessary. The interaction could be synergistic, antagonistic, or have no effect at all. Hence, this study seeks to assess the tribological behavior of nitrogen-doped ZnO thin films under lubricated contacts. The films were deposited on 304L stainless steel using MOCVD from combinations of zinc acetate and ammonium acetate precursor. Contacts were lubricated with basestock polyalpha-olefin (PAO10) without additives. The quantity of oil can affect tribological behavior. Thus, tests were conducted under both marginally lubricated and fully flooded conditions.

2 Experimental details

Nitrogen-doped ZnO thin films were prepared by using the pyrolytic method of MOCVD. The schematic diagram of the MOCVD apparatus was used is shown in Fig. 1. The MOCVD setup is a locally adapted design that had been used in previous studies [28–34]. It is simple, cost effective, and suitable for large-scale production of various thin films for different applications. 304L stainless steel is commonly used for tribological application where corrosion resistance is important and was therefore used as the substrate. A mixture of zinc acetate and ammonium acetate (which serve as the source of nitrogen) was used as the precursor. These two precursors were mixed together in different proportions and grounded thoroughly in a mortar. The fine powder of the precursor was poured into an unheated receptacle, and compressed air was blown through the precursor at a rate of 2.5 dm^3/min. The airborne precursor was transported into the working chamber, which was maintained at 420 °C by an electrically heated furnace. The deposition time was 2 h. Five sets of films, using different ratios of the two precursors, were produced. Table 1 shows the different ratios of the precursor that was used.

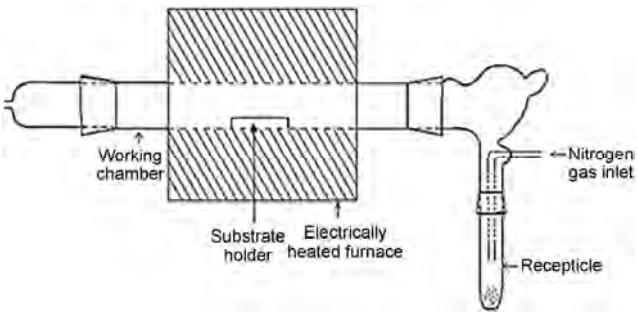

Fig. 1 Schematic diagram of MOCVD apparatus.

The elemental composition, stoichiometry, and thickness of the thin films were determined using Rutherford backscattering spectroscopy (RBS). This procedure was performed by using a 1.7 MeV Tandem accelerator, which involves the use of 1.5 MeV $^4He^+$. The detector scattering angle was 147.7°. The spectrum was obtained under normal condition (angle of incidence $\theta_1 = 0°$ and angle of emergence $\theta_2 = 180°$) with a beam current of 3.8 nA and a nominal beam size of 1 mm. SIMNRA was used to analyze the spectrum that was extracted from the accelerator detector. The X-ray diffraction pattern of the nitrogen-doped ZnO thin films was obtained using MD-10 mini diffractometer with CuK_α radiation. The applied voltage was 25 kV with an exposure time of 1,200 seconds. The intensity data were collected over a diffraction angle, 2θ range of 15° to 50°.

Oil-lubricated friction and wear tests were conducted with a ball-on-flat configuration in reciprocating sliding by using a high-frequency reciprocating rig. The ball

Table 1 Precursor combination, 3-D roughness parameter and thickness of thin films.

Thin Film	Precursor	3-D roughness parameter (nm)	Thickness (nm)
ZO	100% zinc acetate	259.46	185
NZO1	90% zinc acetate + 10% ammonium acetate	162.85	424
NZO2	80% zinc acetate + 20% ammonium acetate	195.66	331
NZO3	70% zinc acetate + 30% ammonium acetate	196.90	253
NZO4	60% zinc acetate + 40% ammonium acetate	157.52	172

counterface was Al alloy (2017) with a diameter of 12.7 mm. The ball's 3D surface roughness parameter (S_a) and hardness are 798 nm and 6.7 GPa ($62R_C$), respectively. The surface statistical properties of nitrogen-doped ZnO thin films were reported earlier [35]. The surface roughness parameters of the films are listed in Table 1. The 304L stainless steel substrate with an isotropic finish similar to that of the thin films (which serves as the baseline) and nitrogen-doped ZnO thin films deposited on 304L stainless steel were tested against the Al alloy (2017) ball. Pure ZnO thin film from 100% zinc acetate, which serves as a control film, was also tested.

The tests were conducted by applying a dead weight of 10 N, which imposes a Hertzian contact pressure of 0.35 GPa. Contacts were lubricated in two ways: marginally lubricated, in which one drop of oil was added at the start of each test, and fully flooded lubrication condition, in which an adequate amount of lubricant was applied to cover the flat surface completely for the entire duration of the test. Basestock synthetic polyalfaolefin oil (PAO10) without additives was used as lubricant. It has a viscosity of 71.1 cSt at 40 ℃ and a specific gravity of 0.837. The reciprocating frequency was 1 Hz with a stroke length of 20 mm, equivalent to a linear sliding speed of 2 cm/s. All tests were run for 30 minutes in ambient room air (temperature of 25 ℃ and relative humidity of 65%).

Frictional force was continuously measured during each test from which the coefficient of friction, defined as the ratio of the frictional force to the normal force, was calculated. Wear on flats and ball counterface material was evaluated at the conclusion of each test by using 3D profilometry with an ADE-Phaseshift MicroXam white light optical profilometer. The surface of the flats and the ball counterface were also examined by using an optical microscope to assess the wear and surface damage mechanism.

3 Result and discussion

3.1 Thin films and characterization

Films of good uniformity and adherence were obtained at the deposition temperature of 420 ℃. In the hot chamber, the precursor first sublimed before the thermal decomposition, resulting in the coating of the substrate. In the MOCVD process, the deposition involves homogeneous gas phase reactions, which occur in the gas phase, and (or) heterogeneous chemical reaction, which occurs on or near the vicinity of a heated surface, thereby leading to the formation of films.

A typical RBS spectrum of the films is shown in Fig. 2. The spectrum depicts two sections, namely, the substrate section and the coating section, which is around 1,450 keV. The expected elements were detected, with the presence of N, Zn, and O clearly manifested. The stoichiometric ratio of N:Zn:O in all the films was estimated to be 1:5:4, while the thickness ranged between 172 and 424 nm. More detailed analysis of stoichiometry and thickness had been reported earlier [27, 36]. The standard calowear test was also used to measure the thickness of the films. This process involves the creation of a crater by a rotating ball of a known diameter through the film into the substrate. An average value of six different points at different places on the film was taken. The thickness measured by this technique is consistent with that of RBS.

A typical X-ray diffraction pattern of the thin films is shown in Fig. 3. Diffraction peaks occur at various diffraction angles, which correspond to (100), (002), and (101) plane. All the obtained peaks were assigned to the standard hexagonal wurtzite ZnO crystal structure (JCPDS 36-1451). No other peaks that correspond to nitrogen were observed. The presence of these peaks shows that all the films are polycrystalline. The

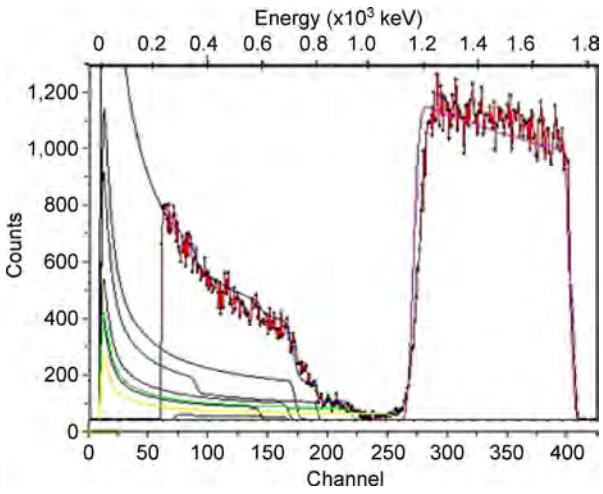

Fig. 2 RBS spectrum of nitrogen-doped ZnO thin film.

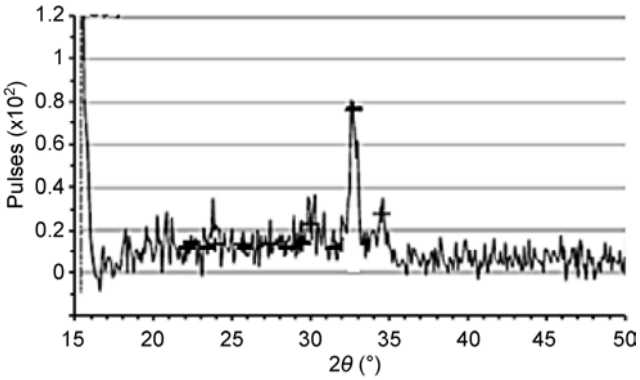

Fig. 3 Typical XRD pattern of nitrogen-doped ZnO thin film.

(002) peak has the highest intensity. The dominance of the (002) peak suggest a highly textured structure in which the *c* axis preferentially aligned perpendicular to the substrate normal. The (002) texture is commonly observed in ZnO films because the *c*-plane perpendicular to the substrate normal is the most densely packed and thermodynamically preferred in the wurtzite structure. The average crystal size of the films based on full width at half maximum (FWHM) of diffraction peaks calculated using Debye–Scherrer equation was 52 and 30 nm for the ZnO thin film and all N-doped ZnO thin films, respectively. The decrease in grain size can be linked to peak broadening, which causes the broadening of FWHM and eventually leads to a decrease in crystallinity. Such peak broadening may be a result of a defect brought about by the incorporation of nitrogen into the ZnO lattice. This result successfully demonstrated that nitrogen can be incorporated into the ZnO thin film lattice by using a combination of zinc acetate and ammonium acetate precursors. The tendency of decreasing grain size and crystallinity with the incorporation of nitrogen in ZnO lattice is similar to that in some previously reported works [26, 37, 38].

3.2 Friction and wear result

The friction behavior of the thin films and the 304L stainless steel substrate (baseline) with reciprocating sliding under both marginally lubricated and fully flooded conditions is shown in Fig. 4. In both the marginally lubricated and fully flooded conditions, a range of friction behaviors were observed. Under the marginally lubricated condition, the substrate showed a friction behavior that is oscillatory in nature, rising and falling at various intervals. The coefficient of friction first increased rapidly at the start of the test to a value of approximately 0.18, followed by a gradual decrease to a value of approximately 0.14 within the first 140 s. Thereafter, the rise and fall continued, which ranged between 0.15 and 0.22. Such frictional behavior can be attributed to the build-up and collapse of the transfer layer [39]. Although this is a lubricated test, the amount of lubricant is marginal, thereby making the operating lubrication regime boundary. Hence, extensive material interaction will still be dominant between the contacting materials through the lubricant film. The contact first produces a high coefficient of friction as a result of the plowing effect, which results in the roughening of the softer material, thereby generating wear debris that can be entrapped. The wear debris accumulates to build up a transfer layer that may become thicker and unstable and eventually collapse. This cycle of buildup and collapse of the transfer layer continued throughout the test, thereby leading to the rise and fall of the coefficient of friction. ZO and NZO1 films showed a similar frictional behavior. The run-in period followed by a fairly stable friction coefficient value that ranges between 0.10 and 0.12 was observed, after which both films showed a transition to unstable higher values (between 0.13 and 0.19) that occurred around 1,300 s. This behavior is mostly likely a result of the wearing-through of films. Similar trends were also observed for the remaining three NZO films (NZO2, NZO3, and NZO4): a run-in period followed by steady-state friction coefficient values between 0.11 and 0.12. Thus, the thin films can evidently provide friction reduction under marginal lubrication. For both ZO and NZO films, such reduction occurred before 1,300 s. The friction reduction in the films can be attributed to the thin films carrying some of the contact load, thus allowing easier sliding between the opposing surfaces. This condition may be a result of the nanocrystalline nature of the films as calculated by the Debye–Scherrer equation [12, 13]. Our result is comparable to that obtained by using sub-microsphere ZnO particles and compositing sub-microsphere ZnO with Al_2O_3 nanoparticles as lubricant additives studied by other authors [12, 13, 20]. Those authors also suggested

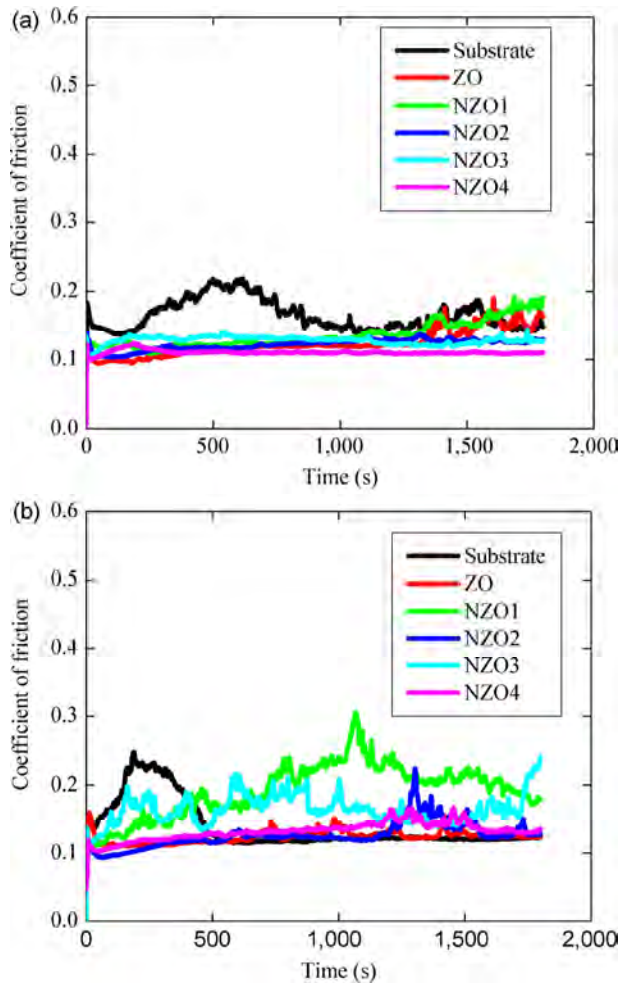

Fig. 4 Coefficient of Friction variation with time under (a) marginally lubricated and (b) fully flooded contact.

that rolling friction became dominant instead of sliding friction, thereby causing the composite micro/nanoparticles to squeeze into the grooves on the rubbing surfaces and reducing friction and wear.

In the fully flooded condition, the coefficient of friction for the substrate increased rapidly to a value of 0.15 at the start of the test, after which it increased gradually to a maximum value of approximately 0.25. After this initial response, the coefficient of friction decreased to a steady-state value of 0.12 in the last 1,200 s of the test. The initial increase in the coefficient of friction is a result of the run-in process. The steady-state coefficient of friction can be attributed to the extensive formation of a transfer layer on the 304L stainless steel flat, such that after the run-in period, the contacting interface may consist of a sliding aluminum transfer film on the aluminum alloy ball. This type of friction behavior, that is, an initial increase in the coefficient of friction followed by a slow decrease to a constant value, was also observed for aluminum in contact with other materials [40, 41]. During the run-in period, high asperities may be worn down, surface films may be removed, or new films may form [42]. After this period, new changes may occur at the interface of the two sliding surfaces, thereby leading to the formation of a new layer, which may cause a decrease in the coefficient of friction to a new steady-state value. These changes may also include oxidation at the tribocontact interface, thereby resulting in the formation of oxides. Wear debris from the ball may also become trapped at the contact interface. In general, tribolayers consist of a complex mixture of both material pairs in contact, as well as specie from the environment [43]. A steady-state friction coefficient value of 0.11 occurred in ZO within 75 and 650 s. The friction coefficient value then ranged between 0.12 and 0.15 with a stable value of 0.12 in the last 300 s of the test. NZO1 exhibited an unstable friction coefficient ranging between 0.13 and 0.31 throughout the entire duration of the test. For NZO2 film, the steady-state friction coefficient value was approximately 0.11 up to around 1,145 s, after which it showed a noisy pattern followed by a constant value of 0.12 in the last 100 s. NZO3 showed an unstable coefficient of friction, reaching a maximum of 0.24 at the end of the test. The coefficient of friction for NZO4 thin film was similar to that of NZO2. The steady-state value was 0.12 until 1,200 s. The friction showed a slight perturbation between 1,200 and 1,500 s, after which it remained nearly constant at a value of 0.12 within the last 300 s. The perturbation observed in ZO, NZO2, and NZO4 may be a result of some localized damage in the film (as shown in Figs. 8(b) and 13(b)), which can be caused by abrasion. However, after such damage, tribolayer quickly built up on the damage, thereby causing the coefficient of friction to return to a steady state that was observed in the last 100 s and 300 s as the case may be. With this condition, the thin films can provide friction reduction only during the run-in period. Indeed, after the run-in period, during which the tribolayer formed on the substrate, the coefficient of friction for the substrate became lower than that for some of the thin films. Unlike in the

marginally lubricated condition, superfluous lubrication of N-doped ZnO thin film is not needed to reduce friction.

At the conclusion of each test, the wear track on both the Al alloy ball counterface and the flat surfaces were characterized by 3D profilometry and optical microscopy. Figures 5–8 show the typical 3D optical profile for flat and ball counterface pairs in marginally lubricated and fully flooded conditions. Most of the wear was produced in the softer counterface (Al alloy ball), and wear on the flats was minimal coupled with evidence of material transfer from the ball counterface. Thus, wear assessment was performed by measuring the wear on the ball counterface for each test. A summary of the wear volume in the balls at the conclusion of the tests for the marginally lubricated (plotted on a log-scale) and fully flooded conditions is shown in Fig. 9. Although no accurate relationship between friction and wear producing realistic result has been defined [44], friction plays an important role in wear volume within a given system. Consequently, the wear behavior of the ball counterface in this study is strongly related to the friction behavior for each flat and ball pair. The wear volume in the ball tested against the thin films is lower than that tested against the substrate under marginally lubricated contact. The thin film-ball pairs also showed lower friction than the substrate-ball pair under the marginally lubricated condition. Under the fully flooded condition, with the exception of NZO1, a reduction in the ball wear volume of the films was observed compared with that of the ball wear volume of the substrate. This result is expected as the friction coefficient of ZNO1 showed unstable behavior, reaching the highest value of 0.31. Thus, the thin films actually protected the ball counterface to a certain extent. The wear reduction could be due to the reduction of shear stress and resultant tensile stresses on the Al alloy ball surface.

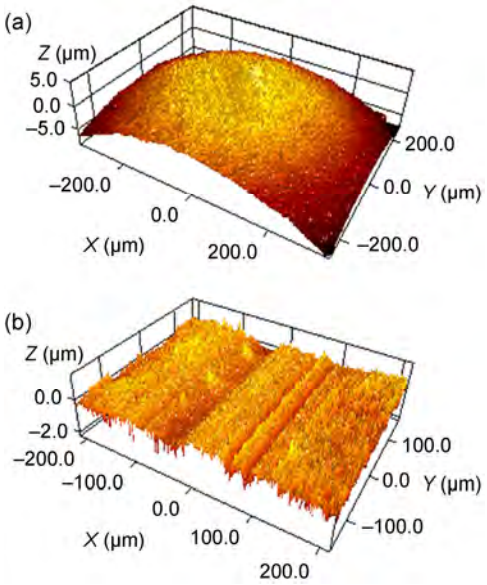

Fig. 6 Typical 3D optical profile of (a) ball counterface and (b) nitrogen-doped ZnO thin film for marginally lubricated condition.

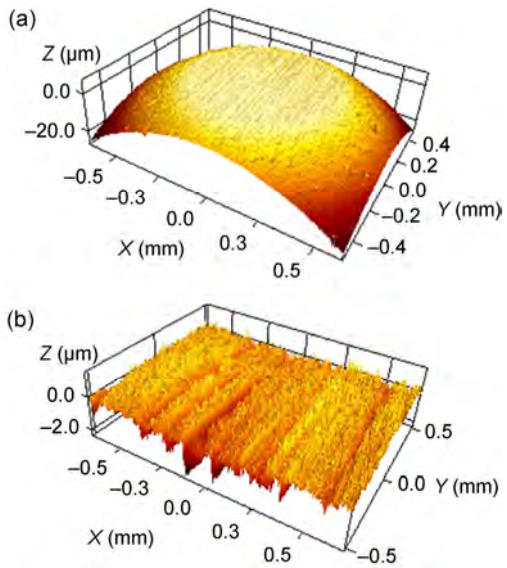

Fig. 5 Typical 3D optical profile of (a) ball counterface and (b) substrate for marginally lubricated condition.

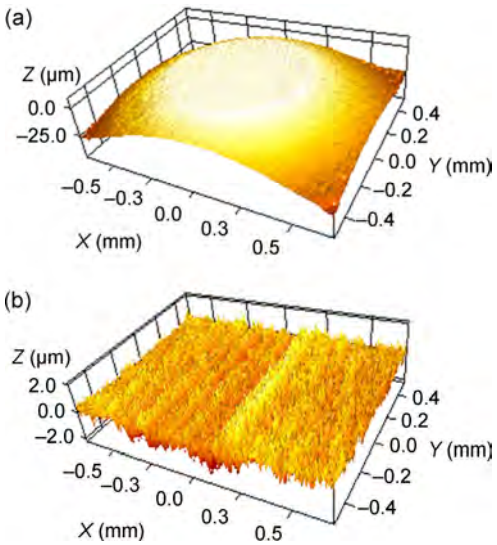

Fig. 7 Typical 3D optical profile of (a) ball counterface and (b) substrate for fully flooded condition.

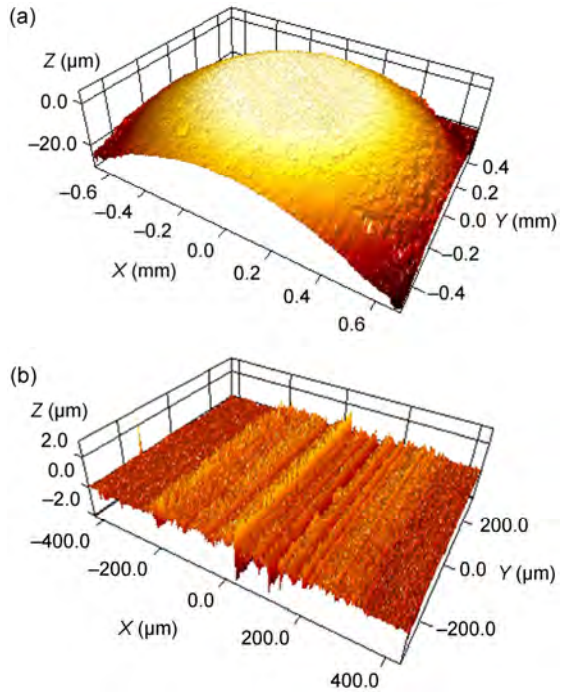

Fig. 8 Typical 3D optical profile of (a) ball counterface and (b) nitrogen-doped ZnO thin film for fully flooded condition.

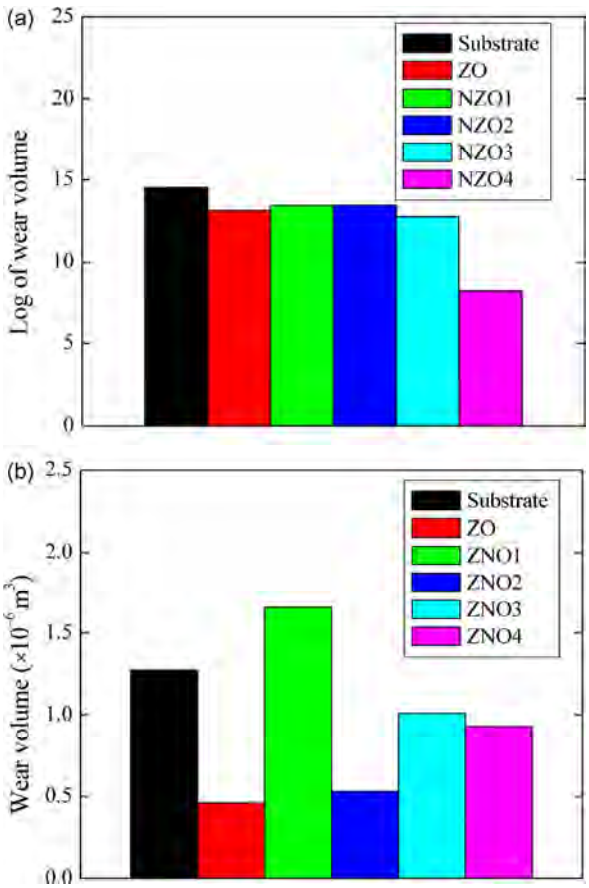

Fig. 9 Ball wear volume after friction test for (a) marginal and (b) flooded condition.

Figures 10–13 show the optical micrographs of wear in the ball and flat pairs under both marginally lubricated and fully flooded conditions. Features observed in the micrographs were similar to those observed in the 3D optical profiles. For substrates tested under both conditions, although wear track is evident, it is for the most part covered by surface films. Such surface films build up and collapse, leading to the rise and fall of the friction coefficient observed in the marginally lubricated test. However, for the fully flooded test, the surface films remain stable, thereby leading to the stable friction coefficient observed in the last 1,200 s of the test. For the thin films tested under both under marginally and fully flooded conditions, evidence of material transfer from the ball exists.

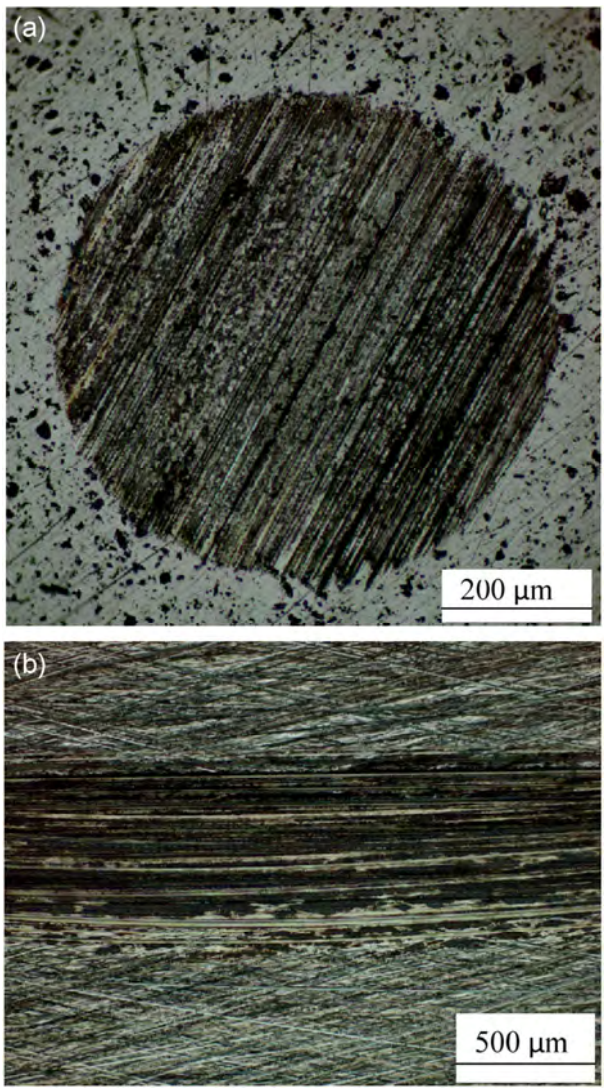

Fig. 10 Optical micrograph of (a) ball counterface and (b) substrate under marginally lubricated condition.

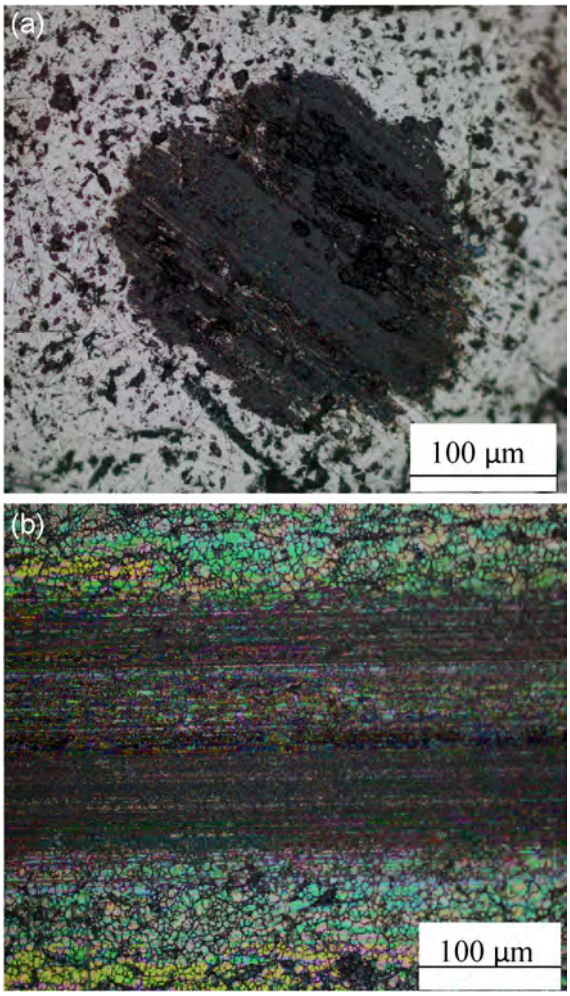

Fig. 11 Typical optical micrograph of (a) ball counterface and (b) nitrogen-doped ZnO thin film under marginally lubricated condition.

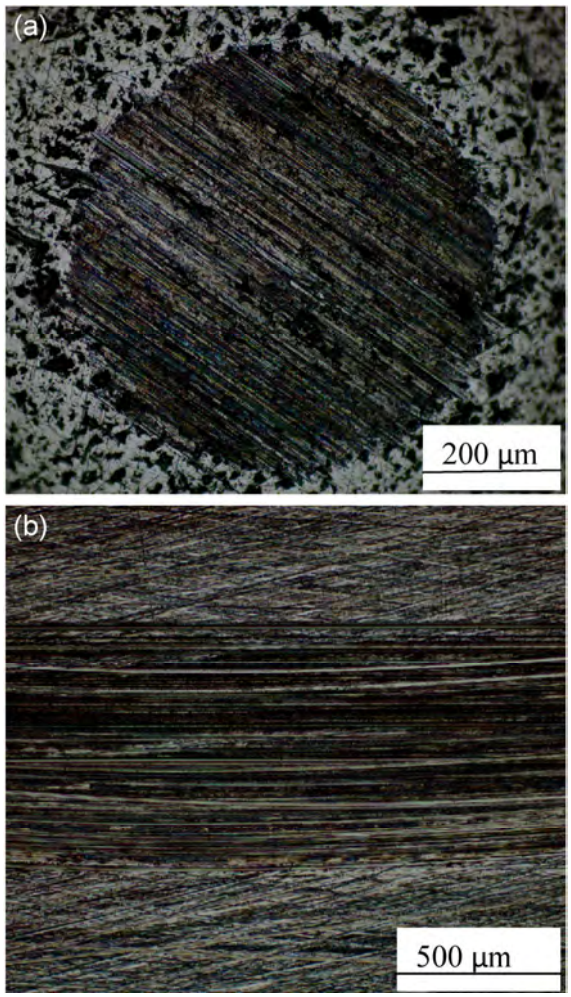

Fig. 12 Optical micrograph of (a) ball counterface and (b) substrate under fully flooded condition.

Some localized damage, which can occur either by abrasion (as indicated by scratches in the direction of sliding) or mild polishing, can also be seen. Different mechanisms and kinetics of material transfer from the ball counterface that occurred during sliding could lead to material build-up on the flats. For instance, after the films had been worn through, the ball comes in contact with the substrate, thereby causing substantial damage and material removal from the ball, which can then be re-deposited on the substrate. The removal of the film coincided with the increase in the coefficient of friction observed in some of the friction behavior because the ball is now sliding against the 304L stainless at this point. A transfer layer may then build up, which accounts for the steady-state coefficient of friction observed in the last 100 or 300 s of the fully flooded test. With the exception of the ball counterface for NZO4 under marginally lubricated contact, all the balls under both conditions undergo abrasive wear, as indicated by scratches of various sizes in the sliding direction. For the ball counterface of NZO4 under marginally lubricated contact, wear occurred by mild polishing, thereby showing the lowest wear volume, as can be seen in Fig. 9.

4 Conclusion

Nitrogen-doped ZnO thin films were deposited on 304L stainless steel substrate using MOCVD through the pyrolysis of zinc acetate and ammonium acetate in different ratios at a temperature of 420 °C. RBS indicated that the expected elements were present in the thin film, and the stoichiometric ratio of N:Zn:O was estimated to be 1:5:4 in all the films. The XRD

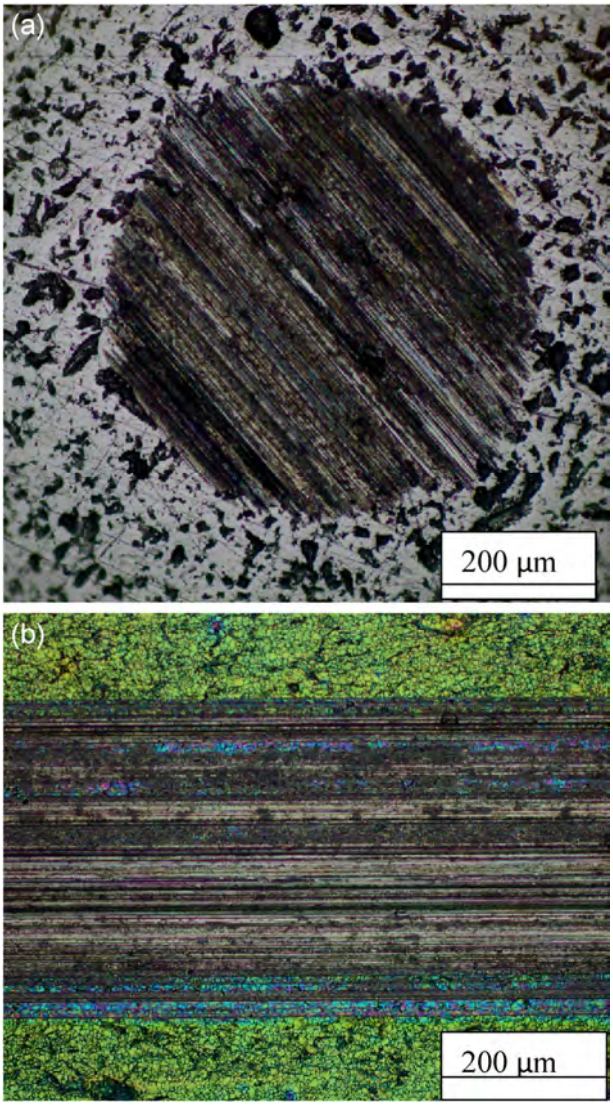

Fig. 13 Typical optical micrographs of (a) ball counterface and (b) nitrogen-doped ZnO thin film under fully flooded condition.

result demonstrated the nanocrystalline nature of the films with a hexagonal structure, which mirrored that of hexagonal wurtzite ZnO, in which *c* axis-oriented (002) plane perpendicular to the substrate dominated.

The friction and wear behaviors of 304L stainless steel and nitrogen-doped ZnO thin films were studied by using high-frequency reciprocating rig, sliding under marginally lubricated, and fully flooded conditions. The tests were conducted with unformulated synthetic PAO10 as lubricant. Nitrogen-doped ZnO thin films were able to provide friction reduction compared with the substrate under marginal lubrication, although the film was worn through in two samples (ZO and ZNO1) of the films. Under the fully flooded condition, three of the N-doped ZnO thin films (ZO, NZO2, and NZO4) were able to provide friction reduction only during the run-in period. After the run-in period, the coefficient of friction for the substrate became lower (after a good transfer layer had formed) than that of the nitrogen-doped ZnO thin films.

Most of the wear was produced in the Al alloy ball counterface as the wear on the flats was minimal coupled with material transfer from the ball counterface. The wear behavior of the ball counterface was strongly related to the friction behavior. Under the marginally lubricated condition, nitrogen-doped ZnO thin films showed a significant effect in protecting the ball counterface. Indeed, wear volume was reduced compared with that of the substrate. Under the fully flooded condition, with the exception of one of the films (NZO1), a reduction in the ball wear volume of the nitrogen-doped ZnO thin films was also observed compared with that of the substrate. In all the ball counterfaces for nitrogen-doped ZnO thin films under both marginally lubricated and fully flooded conditions, wear occurred through the abrasive mechanism of various degrees or mild polishing. Thus, superfluous lubrication of nitrogen-doped ZnO thin films is not necessary to reduce friction and wear.

Acknowledgements

This work was supported by U.S. Department of Energy, Energy Efficiency and Renewable Energy, Office of Vehicle Technologies, under contract DE-AC02-06CH11357. The authors are also grateful to Center for Research and Development, Obafemi Awolowo University, Ile-Ife, Nigeria, for RBS and XRD analyses.

References

[1] Khorramain B A, Iyer G R, Kodali S, Natarajan P, Tupil R. Review of antiwear additives for cranckcase oils. *Wear* **169**: 87–95 (1993)

[2] Zhou X D, Wu D M, Shi H Q, Fu X, Hu Z S, Wang X B, Yan F Y. Study on the tribological properties of surfactant-modified MoS_2 micrometer spheres as an additive in liquid paraffin. *Tribol Int* **40**: 863–868 (2007)

[3] Song X, Qiu Z, Yang X, Gong H, Zheng S, Cao B, Wang H, Möhwald H, Schukin D. Submicron-lubricant based on crystalline Fe_3O_4 spheres for enhanced tribology performance. *Chem Mater* **26**: 5113–5119 (2014)

[4] Harnandez-Battez A, Gonzàlez R, Viesca J L, Fernandez J E, Fernandez J M D, Machado A, Chou R, Riba J. CuO, ZrO_2 and ZnO nanoparticles as antiwear additive in oil lubricants. *Wear* **265**: 422–428 (2008)

[5] Radice S, Mischler S. Effect of electrochemical and mechanical parameters on the lubrication behavior of Al_2O_3 nanoparticles in aqueous suspension. *Wear* **261**: 1032–1041 (2006)

[6] Hu X, Gong H, Wang Y, Chen Q, Zhang J, Zheng S, Yang X, Cao B. Laser induced reshaping of particles aiming at energy saving applications. *J Mater Chem* **22**: 15947–15952 (2012)

[7] Zabinski J S, Corneille J, Prasad S V, Mc Devitt N T, Bultman J B. Lubricious zinc oxide films: Synthesis, characterization and tribological behavior. *J Mater Sci* **32**: 5313–5319 (1997)

[8] Prasad S V, Zabinski J S. Tribological behavior of nano-crystalline zinc oxide films. *Wear* **203**–**204**: 498–506 (1997)

[9] Prasad S V, Walck S D, Zabinski J S. Microstructural evolution in lubricious ZnO films grown by pulsed laser deposition. *Thin Solid Films* **360**: 107–117 (2000)

[10] Zabinski J S, Sanders J H, Nainaparampil J, Prasad S V. Lubrication using a microstructurally engineered oxide: Performance and mechanism. *Tribol Lett* **8**: 103–116 (2000)

[11] Chai C, Lu X, He D. Atomic layer deposition of zinc oxide films: Effects of nanocrystalline characteristics on tribological performance. *Surf Coat Technol* **207**: 361–366 (2012)

[12] Hu X, Gong H, Wang Y, Chen Q, Zhang J, Zheng S, Yang X, Cao B. Laser induced reshaping of particles aiming at energy saving applications. *J Mater Chem* **22**: 15947–15952 (2012)

[13] Li W, Zheng S, Wang P, Chen Q, Song X, Cao B. Preparation of ZnO nanoparticles with enhanced antifriction properties. *Asian J Chem* **24**: 2753–2756 (2012)

[14] Prasad S V, Nainaparampil J J, Zabinski J S. Tribological behavior of alumina doped zinc oxide films grown by pulsed laser deposition. *J Vac Sci Technol A* **20**: 1738–1743 (2002)

[15] Penkov O V, Lee D H, Kim H, Kim D E. Frictional behavior of atmospheric plasma jet deposited carbon-ZnO composite coatings. *Composite Sci Technol* **77**: 60–66 (2013)

[16] Wang S, Ge S, Zhang D. Comparison of tribological behavior of nylon composite filled with zinc oxide particles and whiskers. *Wear* **266**: 248–254 (2009)

[17] Liu B, Yang Z, Zhou J. Tribological behavior of polyimide zinc oxide hybrid films. *Adv Mater Res* **106**: 438–445 (2010)

[18] Chakraborty H, Sinha A, Mukherjee N, Ray D, Chattopadhyay P P. A study of nanocrystalline and tribological behavior of multifunctional ZnO/PMMA nanocomposite. *Mater Lett* **93**: 137–140 (2013)

[19] Chang B P, Akil H M, Nasir R B M. Composite study of micro- and nano-ZnO reinforced UHMWPE composites under dry sliding. *Wear* **297**: 1120–1127 (2013)

[20] Duan G, Hu X, Song X, Qiu Z, Gong H, Cao B. Morphology evolution of ZnO submicron particles induced by laser irradiation and their enhanced tribology properties by compositing with Al_2O_3 nanoparticles. *Adv Eng Mater* **17**: 341–348 (2015)

[21] Qin H, Li W, Xia Y, He T. Photocatalytic activity of heterostructures based on ZnO and N-doped ZnO. *ACS Appl Mater Interfaces* **3**: 3152–3156 (2011)

[22] Macias-Sanchez J J, Hinojosa-Reyes L, Caballero-Quintero A, de la Cruz W, Ruiz-Ruiz E, Hernandez-Ramireza A, Guzman-Mar J L. Synthesis of nitrogen-doped ZnO by sol gel method: Characterization and its application on visible photocatalytic degradation of 2, 4-D and picloram herbicides. *Photochem Photobiol Sci* **14**: 536–542 (2015)

[23] Herring N P, Panchakarla L S, El-Shall M S. P-type nitrogen-doped ZnO nanostructures with controlled shape and doping level by facile microwave synthesis. *Langmuir* **30**: 2230–2240 (2014)

[24] Naouar M, Ka I, Gaidi M, Alawadhi H, Bessais B, El Khakani M A. Growth structure and optoelectronic properties tuning of nitrogen-doped ZnO thin films synthesized by means of reactive pulse laser deposition. *Mater Res Bull* **57**: 47–51 (2014)

[25] Allenic A, Guo W, Chen Y B, Zhao G Y, Pan X Q, Che Y, Hu Z D, Liu B. Synthesis and properties of p-type nitrogen-doped ZnO thin films by pulsed laser ablation of a Zn-rich Zn_3N_2 target. *J Mater Res* **22**: 2339–2344 (2007)

[26] Lavand A B, Malghe Y S. Synthesis, characterization and visible light photocatalytic activity of nitrogen-doped zinc oxide nanospheres. *J Asian Ceramic Soc* **3**: 305–310 (2015)

[27] Mbamara U S, Olofinjana B, Ajayi O O, Lorenzo-Martin C, Obiajunwa E I, Ajayi E O B. Friction and wear behavior of nitrogen-doped ZnO thin films deposited *via* MOCVD under dry contact. *Eng Sci Technol* **19**: 956–963 (2016)

[28] Ajayi O B, Akanni M S, Lambi J N, Jeynes C, Watt J F. Compositional studies of various metal oxide coatings on glass. *Thin Solid Films* **185**: 123–136 (1990)

[29] Ajayi O B, Ojo I A, Jeynes C. Preparation and characterization of MOCVD thin films of cadmium sulphide. *Thin Solid Films* **248**: 57–62 (1994)

[30] Adedeji A V, Eleruja M A, Ojo I A O, Djebah A, Osasona O, Olowolafe J O, Aladekomo J B, Ajayi E O B. Preparation and characterization of MOCVD ZnCdInS thin films. *Opt Mater* **14**: 345–349 (2000)

[31] Adedeji A V, Egharevba G O, Jeynes C, Ajayi E O B. Preparation and characterization of pyrolytically deposited (CO-V-O and Cr-V-O) thin films. *Thin Solid Films* **402**: 49–54 (2002)

[32] Ilori O O, Osasona O, Eleruja M A, Egharevba G O, Adegboyega G A, Chiodeli G, Boudreault G, Jeynes C, Ajayi E O B. Preparation and characterization of metallorganic chemical vapor deposited $Li_xMo_yO_z$ using a single source solid precursor. *Ionics* **11**: 387–391 (2005)

[33] Olofinjana B, Egharevba G O, Eleruja M A, Jeynes C, Adedeji A V, Akinwunmi O O, Taleatu B A, Mordi C U, Ajayi E O B. Synthesis and some properties of metal organic chemical vapor deposited molybdenum oxysulphide thin films. *J Mater Sci Technol* **26**: 552–557 (2010)

[34] Olofinjana B, Egharevba G, Teleatu B, Akinwunmi O, Ajayi E O. MOCVD of molybdenum sulphide thin film *via* single solid source precursor Bis-(Morpholinodithioato-S,S')-Mo. *J Mod Phys* **2** 341–349 (2011)

[35] Mbamara U S, Olofinjana B, Lorenzo-Martin C, Ajayi O O, Obiajunwa E I, Ajayi E O B. Surface statistical topographical properties of ZnO:N thin films deposited by MOCVD. *J NanoSci NanoEng* **1**: 18–22 (2015)

[36] Mbamara U S, Akinwunmi O O, Obiajunwa E I, Ojo I A O, Ajayi E O B. Deposition and characterization nitrogen-doped zinc oxide thin films by MOCVD using zinc acetate-ammonium acetate precursor. *J Mod Phys* **3**: 652–659 (2012)

[37] Xu W, Ye Z, Zhou T, Zhao B, Zhu L, Huang J. Low pressure MOCVD growth of p-type ZnO thin films by using NO as the dopant source. *J Cryst Growth* **265**: 133–136 (2004)

[38] Tan S T, Chen B J, Sun X W, Yu M B, Zhang X H, Chua S J. Realization of intrinsic p-type ZnO thin films by metal organic vapor deposition. *J Electron Mater* **34**: 1172–1176 (2005)

[39] Qu J, Blau P J, Zhang L, Xu H. Effect of multiple treatment of low-temperature colossal supersaturation on tribological characteristic of austenitic stainless steel. *Wear* **265**: 1909–1913 (2008)

[40] Schön J. Coefficient of friction for aluminum in contact with a carbon fiber epoxy composite. *Tribol* **137**: 395–404 (2004)

[41] Schön J. Coefficient of friction of composite delamination surfaces. *Wear* **237**: 77–89 (2000)

[42] Qu J, Blau P J, Jolly B C. Tribological properties of stainless steel treated by colossal carbon supersaturation. *Wear* **263**: 719–726 (2007)

[43] Lorenzo-Martin C, Ajayi O, Erdemir A, Fenske G R, Wei R. Effect of microstructure and thickness on the friction and wear behavior of CrN coatings. *Wear* **302**: 963–971 (2013)

[44] Budinski K G, Budinski M K. *Engineering Materials, Properties and Selection.* New Jersey (USA): Prentice Hall, 2002.

Bolutife OLOFINJANA. He received his bachelor, M.Sc., and Ph.D. degrees in enigineering physics from Obafemi Awolowo University, Ile-Ife, Nigeria in 1999, 2005, and 2011, respectively. He joined Obafemi Awolowo University as an assistant lecturer in the department of Physics and Engineering Physics. He is currently a senior lecturer in the same department. His research interests include surface modification for active control of friction and wear, and preparation and characterization of nano-structured materials for various applications.

Friction **5**(4): 414–428 (2017)
DOI 10.1007/s40544-017-0155-9
ISSN 2223-7690
CN 10-1237/TH
RESEARCH ARTICLE

Aqueous lubrication and surface microstructures of engineering polymer materials (PEEK and PI) when sliding against Si_3N_4

Anying WANG, Shuai YAN, Bin LIN*, Xiaofeng ZHANG, Xiaoxue ZHOU

Key Laboratory of Advanced Ceramics and Machining Technology of Ministry of Education, Tianjin University, Tianjin 300350, China

Received: 11 October 2016 / Revised: 25 December 2016 / Accepted: 14 February 2017

Abstract: Polyether-ether-ketone (PEEK) and polyimide (PI) are two kinds of engineering polymer materials widely used as roller bearing cages and rings under extreme environment because of their noise reduction and corrosion resistance properties. The Si_3N_4 ceramic is the most common ball bearing material. Many current engineering applications of ball bearings require aqueous lubrication. Therefore, this study presents the aqueous lubrication of tribopairs formed by PEEK and PI material sliding against Si_3N_4 ceramic. Experimental results show that two tribopairs exhibited the similar tribological properties under the dry condition. Water as a lubricant for the PI–Si_3N_4 tribopair pairs effectively reduces both friction coefficients by 35.5% and wear rates by 32%. The water absorption of PI induces better tribological properties by changing the tribopair surface properties. In addition, the dimples appearing on the PI tribopair surface under water generate additional hydrodynamic lubrication and further improve the friction properties of surface. The PEEK–Si_3N_4 tribopair shows similar friction coefficients under two kinds of environments. The wear rates under water are approximately more than two times of that under dry sliding. However, water inhibits the appearance of the crush phenomenon and enhances the carrying capacity of the tribopair. Energy dispersive spectroscopy and X-ray diffraction spectra demonstrate no chemical corrosion. The 3D profiler and SEM morphologies illustrate that the transfer film would be formed from the surface of PEEK under water but hindered under dry friction. Overall, the PI–Si_3N_4 tribopair exhibits better properties than PEEK under water and is promising for future applications in the bearing industry.

Keywords: PEEK; PI; aqueous lubrication; dry friction; tribological properties; ceramic bearing

1 Introduction

Engineering plastic with excellent properties of mechanics and tribology and outstanding resistance to high temperature, chemical corrosion, and radiation is a kind of potential bearing material. PEEK and PI [1–5] are two kinds of widely used engineering polymer materials as roller bearing cages and rings in ceramic bearings [6–8]. Ceramic bearings are developed for industrial applications under extreme and special operating conditions in water.

The molecular structure of PEEK makes it not only own a high fracture toughness, high strength, superior corrosion, and excellent resistance to high temperature hydrolysis, but also possesses excellent biocompatibility and tribology properties [9–10]. Zalaznik et al. [13] investigated the influence of different processing temperatures on the properties of pure PEEK. The results of the dry-sliding tribological tests, hardness measurements, and X-ray diffraction (XRD) analyses show that the processing temperature greatly influences the hardness and the crystallinity of PEEK, which in turn affects the tribological behavior. Koike et al. [14] investigated the wear of the PEEK radial ball bearing

* Corresponding author: Bin LIN, E-mail: linbin@tju.edu.cn

composed of a PEEK ring, a PTFE composite retainer, and alumina balls. They found that the PEEK–PTFE adhesion film dramatically improved the wear and rotational performance of the bearing. Greco et al. [15] focused on the effect of the reinforcement morphology on the high-speed sliding friction and wear of PEEK polymers. Meanwhile, Theiler et al. [16] investigated the sliding performance of the PEEK composites in a vacuum environment.

PI shows excellent tribological properties, especially under conditions of high pressure, high temperature, high speed, and other extreme environments [11–12]. Guo et al. [17] studied the structural and chemical properties of polyimide ablated by a femtosecond laser. Liu et al. [18] concluded that the wear rate increased with the increase of the proton and combined radiation time and decreased with the electron radiation conditions. Samyn et al. [19] studied the effect of the processing method on the dry sliding performance of polyimides at high load/high velocity conditions. Jia et al. [20] conducted a comparative investigation of the friction and wear behavior of polyimide composites under dry sliding and water-lubricated condition.

During the past decades, different additives, except the modification of surface properties [21–30], were added into PEEK or PI to improve tribological properties. Many researchers conducted various experiments to investigate the friction coefficient and wear rate of various conditions, providing comprehensive mechanisms of friction and wear at different conditions. Yang and Dong [31] studied the tribological behavior and mechanical properties of PEEK-filled PTFE composites, which were investigated using a scanning electron microscope (SEM). Huang et al. [32–34] studied the friction and wear properties of the PI composites filled with PTFE and MoS_2 sliding against 45 steel, nickel–chromium alloy, copper, and aluminum under the dry sliding friction condition. The PI-based composites filled with various solid lubricants and reinforced with carbon fiber prepared by compression molding sliding against stainless steel registered lower friction coefficients and wear rates in water than in air. Samyn et al. [35] comprehensively investigated the tribological behaviors of a polymer–metal friction pair at different sliding velocities and loads.

Notably, tribological properties and wear mechanisms are closely related to material properties and external condition. The abovementioned researches mainly focused on the composite–steel triobopair [36–38], but there is little knowledge about the wear and friction behaviors of the trio-couple comprising composite materials and Si_3N_4 ceramic [39]. Hence, the tribological properties of triobopairs formed by PEEK and PI composite materials with the Si_3N_4 ceramic material will be studied in this paper. Water is used as a green lubricant to replace mineral oil and vegetable oil because of its low cost, flame retardancy, easy availability, and environmental friendliness [40]. Some friction and wear experiments of different composite materials under water lubrication have been conducted [41–48]. Tomizawa and Fisher [49] found that the friction coefficient between the Si_3N_4 ceramics with water lubrication became less than 0.002 after a running-in process, making it the first study to see that water used as a lubricant could achieve superlubricity [50]. Chen et al. [51] first introduced nanoparticles into the field of water-based superlubricity. Furthermore, the study of friction reduction and improvement of the mechanical efficiency and life in bearings under water lubrication are a major significant research.

Above all, this study focuses on the influence of a water-lubricated condition on the tribological properties of polymer–ceramics tribopairs to guide the application and popularization of ceramic bearings.

2 Procedure and specimens

2.1 Principle and procedure

The lubrication condition, normal load, and sliding velocity were the main variables considered [52]. The ball-on-disk form [53–56] was adopted on a ball-on-disk tribometer (MMW-200). The test lubricant was deionized water. The ball-on-disk tests were conducted in dry lubrication to set the contrast lubricating tests. A Si_3N_4 ball under a settable normal load F was placed on the surface of the rotating disk specimen under a certain ω. The test conditions were selected based on a series of low-load experiments of the effect of load on wear for the lubrication environment. The

results of these wear-in tests showed that the wear rate was too small to be almost impossible to measure under a lower load. The wear rate correspondingly increased as the load increased. A load of 30 N was considered in our experiment to be the conventional condition, whereas a load of 120 N was the extreme condition. Extreme load was chosen to test the polymers' performance in extreme conditions and more comprehensively reflect their performance. Hence, the normal load value was set as 30 N, 75 N, and 120 N. The relative sliding distance was generally kept at 1,800 m to ensure that the tribopairs achieve a stable lubrication state. Therefore, the running time will be set according to linear speeds of 0.25 m/s (7,200 s), 0.5 m/s (3,600 s), and 1 m/s (1,800 s) to explore the effect of velocity. The test settings were shown in the test schedule (Table 1).

2.2 Specimens and theory

The specimens used in the tests were provided by China National Machinery Industry Corporation. The initial surface roughness was 0.03 μm, and the Si_3N_4 ball diameter was 9.525 mm. Tables 2 and 3 show the specimen properties.

Table 1 Test schedule.

Test No.	Experimental factors		
	Load (N)	Sliding velocity (m/s)	Lubricant
1	30	0.25	Dry
2			Water
3		0.5	Dry
4			Water
5		1	Dry
6			Water
7	75	0.25	Dry
8			Water
9		0.5	Dry
10			Water
11		1	Dry
12			Water
13	120	0.25	Dry
14			Water
15		0.5	Dry
16			Water
17		1	Dry
18			Water

Table 2 Properties of Si_3N_4 ball.

Properties	Si_3N_4 ball
Vickers hardness (HV)	1,580
Fracture toughness (MPa·m$^{1/2}$)	6.0
Bending strength (MPa)	900
Density (g/cm^3)	3.5
Initial roughness (μm)	0.014

Table 3 Properties of PEEK and PI composite materials.

Properties	PEEK	PI
Vickers hardness (HV)	144	122
Tensile strength (MPa)	17	16
Compressive strength (MPa)	38	40
Distortion temperature (°C)	102	350

Energy dispersive spectroscopy (EDS) was performed at different locations to ascertain the elemental constituents of the different phases presented in the microstructure. The typical EDS spectrum of the disks observed in Figs. 1 and 2 further verified the presence

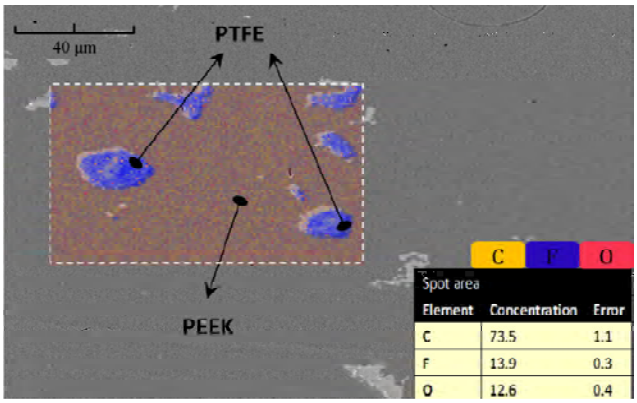

Fig. 1 Typical EDS spectra of PEEK disk at different locations.

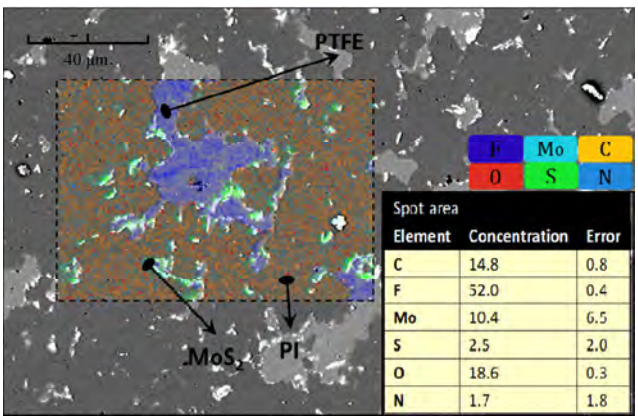

Fig. 2 Typical EDS spectra of PI disk at different locations.

of the specimens. As shown in the figures, the PEEK composite materials used in this test were modified by self-lubricating PTFE particles and the PI modified by a certain percentage of PTFE and MoS_2.

The specimens were ultrasonically cleaned in industrial alcohol for 15 min before every experiment, then ultrasonically cleaned again in acetone for 15 min before thoroughly washing with deionized water and drying in an oven.

The friction coefficient curves were automatically recorded by a tribometer. The wear rate (w) was determined using the following volume method [57]. The wear volume of the ball and the disk was expressed using the two following equations:

$$V_b = \frac{\pi \times D_s^4}{32 D_b} \quad (1)$$

where V_b (mm^3), D_s (mm), and D_b (mm) stand for the wear volume, wear scar diameter of the ball, and ball diameter, respectively.

$$V_d = 2\pi R \times \left(\frac{S_1 + S_2 + S_3 + S_4}{4} \right) \quad (2)$$

where V_d (mm^3) and R (mm) are the wear volume and the sliding radius of the disks respectively, and S_1, S_2, S_3, and S_4 are the cross-section areas of the disk wear scar in four measurements.

The wear rate (w) was determined by the following equation:

$$w = \frac{V}{Fd} \quad (3)$$

where V (mm^3), d (m), and F (N) are the wear volume of the ball or disk, sliding distance, and normal load, respectively.

3 Results and discussions

3.1 Real-time friction coefficients

The ball and disk relatively slid when the motor rotated. The friction coefficient was automatically recorded with a real-time data acquiring system linked to the tribometer. The friction coefficients during the whole test were plotted as a function of the sliding distance in Figs. 3 and 4 for different lubrications when the sliding velocity was set as constant (0.5 m/s). The steady-state friction coefficient under all test conditions mostly ranged from 0.114 to 0.03.

Notably, the friction coefficients of the PI–Si_3N_4 tribopair under water in the following figures had an obvious reduction before a sliding distance of 600 m, then approximately trended to be stable. The PI–Si_3N_4 tribopair showed significant lower friction coefficients in water than that under the dry friction. Taking 120 N as an example, PI obtained the minimum value of the friction coefficient (i.e., 0.026) in water. Compared with PI, water generated little influence on the PEEK–Si_3N_4 tribopair. The minimum value of the friction coefficient was 0.0425.

3.2 Steady-state friction coefficients

Figures 5 and 6 show the steady-state friction coefficients of PEEK and PI as a function of the load and the sliding velocity in different lubrications, respectively.

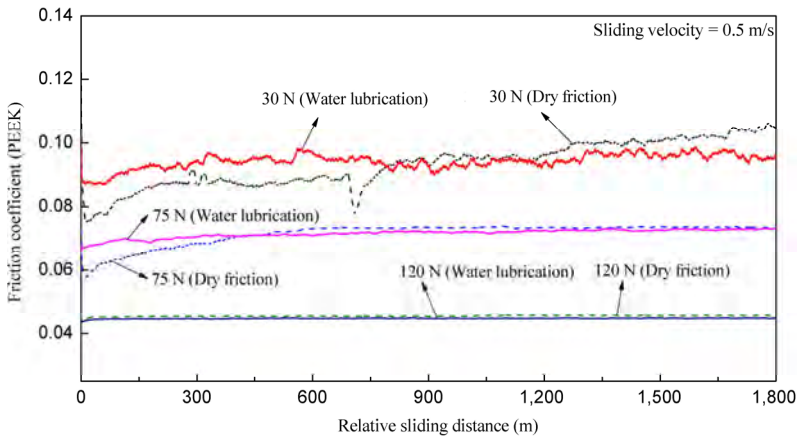

Fig. 3 Friction coefficient of PEEK as a function of relative sliding distance for different conditions.

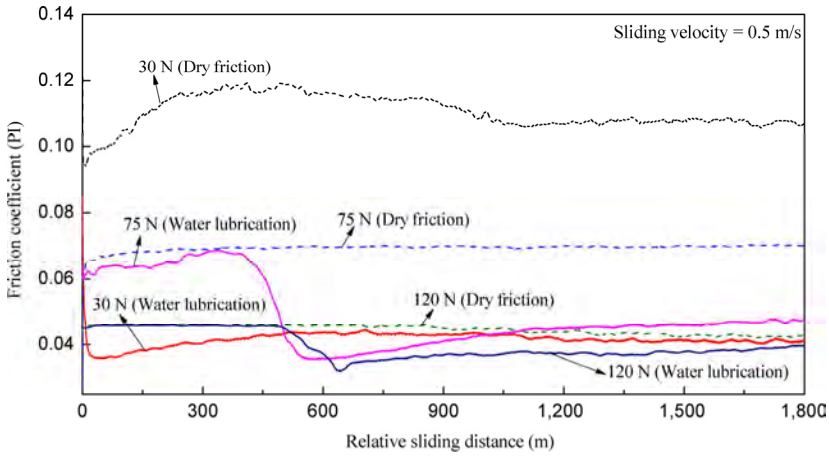

Fig. 4 Friction coefficient of PI as a function of relative sliding distance for different conditions.

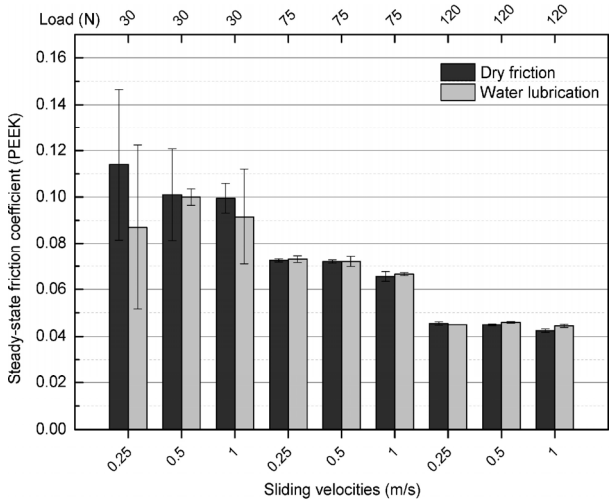

Fig. 5 The steady-state friction coefficients of PEEK–Si_3N_4 tribopair at dry-friction and water-lubricated conditions under different loads and sliding velocities.

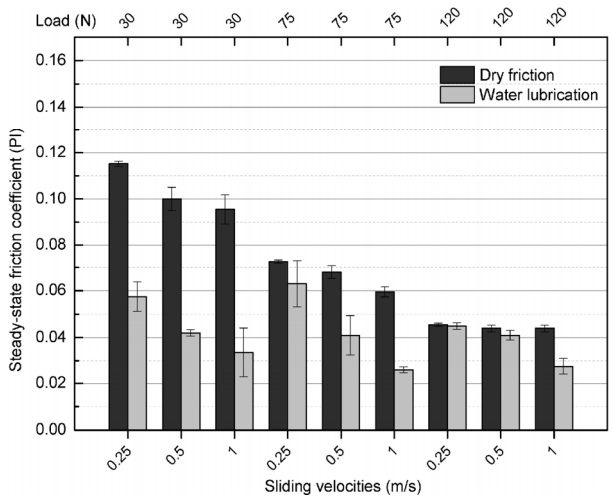

Fig. 6 The steady-state friction coefficients of PI–Si_3N_4 tribopair at dry-friction and water-lubricated conditions under different loads and sliding velocities.

Figure 5 shows that the PEEK coefficients under water were almost equal to those under dry friction. The results indicated that the tribological performance of the PEEK–Si_3N_4 tribopair was not improved under water. Moreover, the friction coefficients of PEEK exhibited a tendency to decrease with the increasing loads. The sliding velocity at medium and high loads exhibited a slighter effect on the friction coefficients compared to the load. These findings showed that the load became the main factor of the friction coefficients instead of the speed, thereby agreeing with the results of the regression analysis from Satapathy [58].

Figure 6 illustrates the typical friction coefficient values of PI under different lubrications. A comparison of all the conditions showed that the friction coefficients under water were smaller than those under dry friction, indicating that the tribological performance of the PI–Si_3N_4 tribopair could be improved under water.

The load for the PI tribopair was the main factor of the friction coefficients instead of the speed under dry friction. This result was similar to that of the PEEK tribopair. However, the coefficients were almost unaffected by the loads and decreased with the increase of the sliding velocities under water. In other words, water could weaken the effect of the load on friction while enhancing that of the sliding velocity.

3.3 Wear rates

The hardness of the Si_3N_4 ball was far greater than that of the PEEK and PI disks. Hence, the wear volume losses of the ball were too little to be measured. So in this paper only wear rates of disks are analyzed and

discussed under the influence of different conditions.

Figure 7 shows the specific wear rates of the PEEK–Si_3N_4 tribopair varying with the setting conditions. Please note that the substrate irregular wear occurred on the PEEK disk surface at 120 N and 1 m/s. Hence, the wear rates were not measured. The wear under water was much more severe than that under dry friction, which was pretty consistent with Mens [59]. He also found that these effects may well be caused by the water penetration into the surface zones of the polymers, causing a corresponding decrease in the "strength" of the polymer surface zone under combined normal and tangential loading conditions. Taking 0.5 m/s from Fig. 7 as examples, the values of the wear rates were 24.8×10^{-6} and 57.8×10^{-6} mm^3/(N·m) at 30 N under dry and water, respectively, showing an increase of 2.3 times. Similarly, the values increased for approximately 2.9 and 2.7 times at 60 N and 120 N, respectively.

The wear rates of PEEK increased with the increasing loads under dry friction. Salant [60] found the same phenomenon. The adhesive wear at a low load occupied the main position. We may learn from Unal [61] that the deformation of the material caused damage when the load increased. The wear rate then increased. The same tendency occurred under water. The wear rates slowly descended with the velocity increase, which was attributed to the plastic flow acceleration caused by softening and melting on the composite surface proposed by Jia [62].

Figure 8 shows the specific wear rates of the PI–Si_3N_4 tribopair. The obvious difference from the PEEK–Si_3N_4 tribopair was that the PI–Si_3N_4 tribopair under water acquired less wear rates than under dry friction. From the nine experiment samples, we could calculate that the wear rates in the water reduced by 32% on average. The minimal wear rate 26.6×10^{-6} mm^3/(N·m) occurred at 30 N and 1 m/s under water. A reasonable interpretation could be that water reduced the friction surface temperature and further reduced the wear caused by the material softening due to heat, which was supported by Unal [61]. Similar to the PEEK tribopair, the wear rates of the PI tribopair exhibited a tendency to decrease with the decreasing loads or the increasing sliding velocities under dry friction. The same tendency occurred under water lubrication. As is also known from Unal [61], fatigue wear was the main wear mechanism under dry condition, and the tribological performance was improved evidently in water.

From the numerical point of view, the wear property of the PEEK tribopair could be slightly better than PI under "no water" condition. However, water exacerbated the PEEK tribopair wear, but relieved the PI. Taking 0.5 m/s as an example, the wear rate values were 227.6×10^{-6} and 85.9×10^{-6} mm^3/(N·m) at 30 N for the PEEK and PI tribopairs, respectively. These values showed a reduction of 2.6 times for PI tribopairs. Similarly, the values reduced by 1.7 and 3.9 times at 30 N and 120 N in water, respectively.

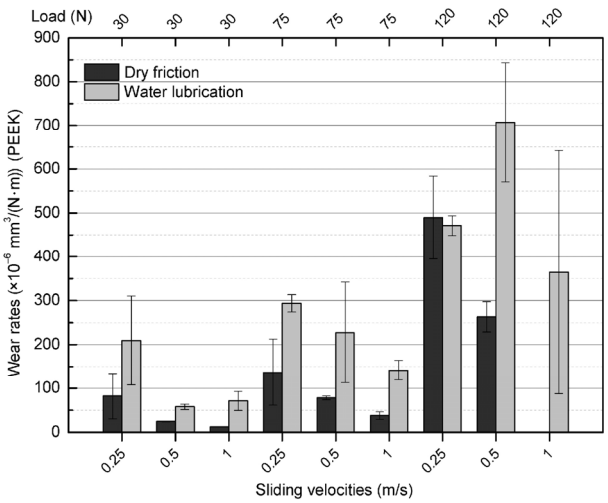

Fig. 7 The wear rates of PEEK at dry-friction and water-lubricated conditions under different applied loads and sliding velocities.

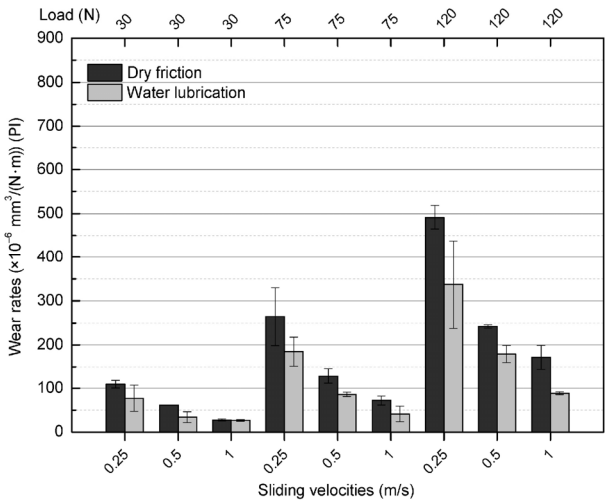

Fig. 8 The wear rates of PI at dry-friction and water-lubricated conditions under different applied loads and sliding velocities.

3.4 3D profiler micrograph analysis of wear surfaces

Figures 9 and 11 show the 3D micrographs of the wear surfaces of the PEEK and PI composite materials after the experiments. Figures 10 and 12 show the 2D cross-sectional profiles of the wear tracks from PEEK and PI surface. The wear losses for the PEEK tribopair increased, and the grinding crack widened and deepened under water. The wear was the main failure form at the normal working load of 30 N. The

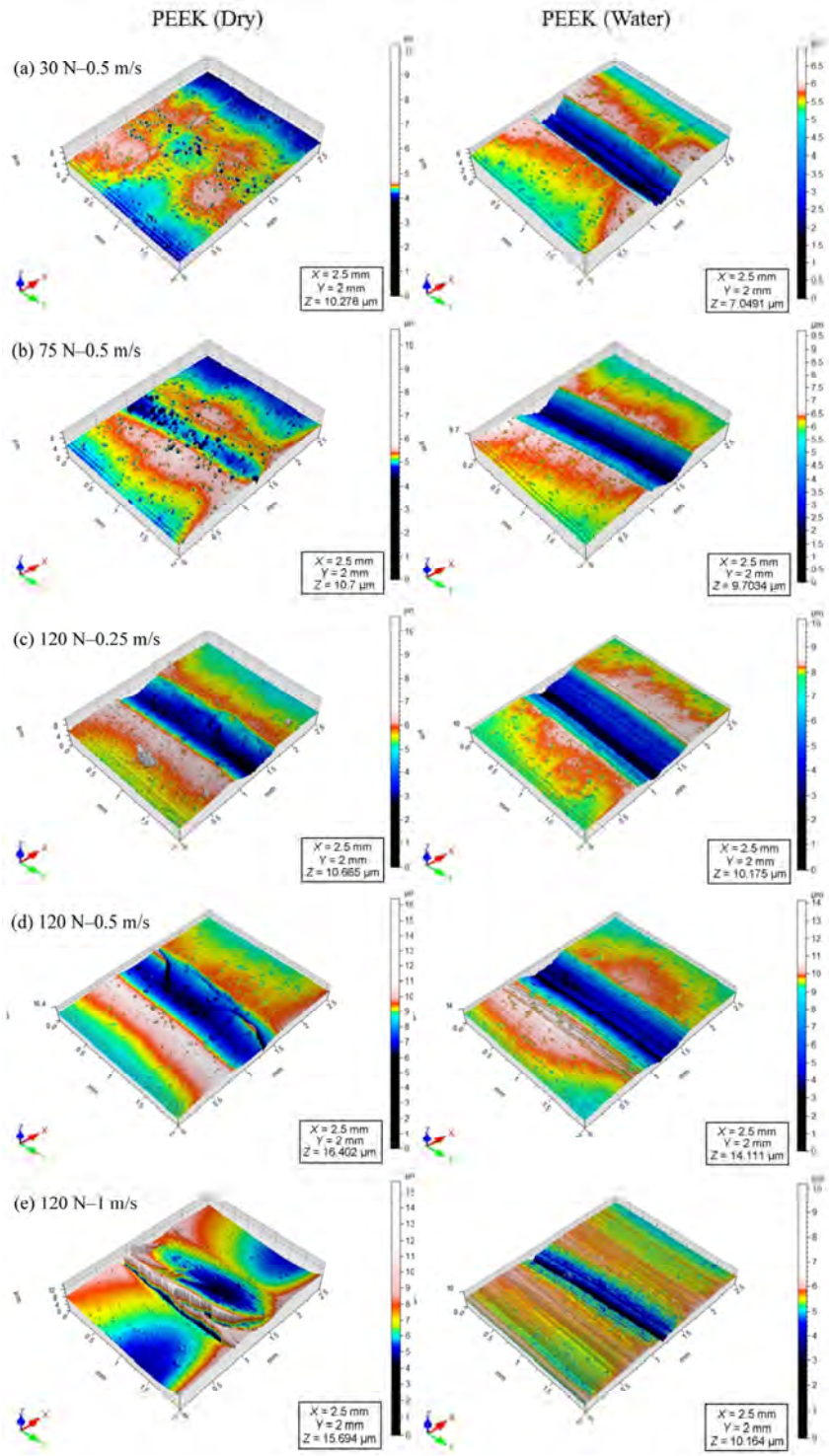

Fig. 9 3-D surface topography of PEEK materials after tests under different lubrications.

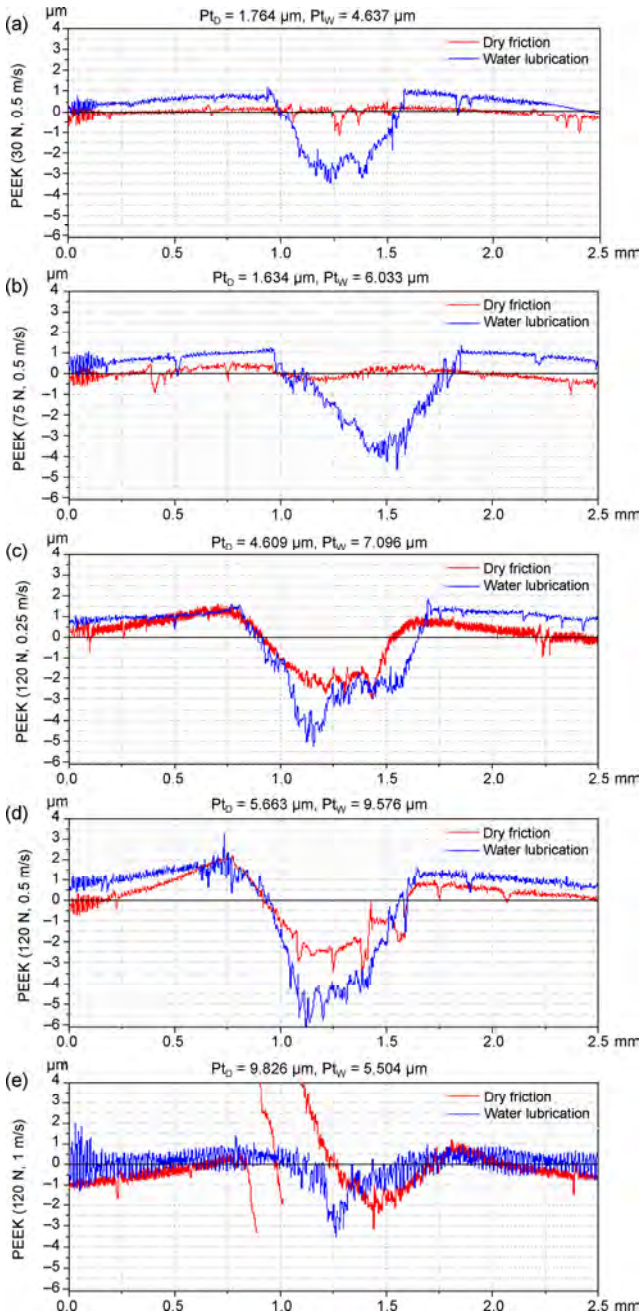

Fig. 10 Cross-sectional profiles of wear tracks from 2-D PEEK surface topography.

PEEK matrix surface could be crushed and cracked under dry friction when the load becomes extreme, such as 120 N. In this case, the shear failures of the polymers would dominate the material loss. This situation is beyond the normal working conditions of the PEEK polymer. Under the water-lubricated condition, the crack would not appear, and the wear rate increases. No crack would be observed on the surface of the PI polymer, for comparison. The wear was the main failure form. Water made the PI tribopair acquire less wear rates. Moreover, the values reduced by 32% on average than that at dry friction. It is worth mentioning that compared with PEEK, PI could withstand a greater applied load and sliding velocity under water. The comparison of the 3D micrographs between the two tribopairs also demonstrated that the PEEK tribopair obtained a smoother surface than PI under water.

3.5 Optical and SEM micrographs of surface wear tracks on tribopairs

Figures 13–14 show the optical micrographs of the worn scares of the Si_3N_4 ball and the SEM micrographs of the worn surfaces of the PEEK and PI disks. Under dry friction, the PEEK disk surface was bruised, and a surface slim crack could be observed. The wear mechanism in this condition was crushing wear. The reason for this phenomenon could be consistent with that mentioned by Samyn [35] that the molecular chains of PEEK do not have enough time to orient under such conditions, thereby inducing embrittlement, polymer degradation, and finally a brittle fracture of the PEEK composite material.

Under the water condition, the scratching phenomenon and the slight wear tracks appeared on the PEEK disk surface, verifying the result and explanation in Figs. 3, 5, 7, 9, and 10. Notably, the transfer film could be formed from the PEEK disk surface. The transfer film would reduce the friction during the friction process. Compared with the dry friction, water sped up the transfer of the PEEK surface material, causing more severe wear rates. In addition, water inhibited the appearance of the crush phenomenon, which manifested that water could enhance the carrying capacity of the PEEK tribopair.

The slight wear tracks for the PI–Si_3N_4 tribopair could be found on the PI disk under dry friction. The transfer film could also be observed on the ball. However, the transfer film was not obvious under the water condition, and significant dimples appeared on the surface.

The above data showed that PI had a more significant reduction of friction coefficients and wear rates under water. On the one hand, the PI surface had

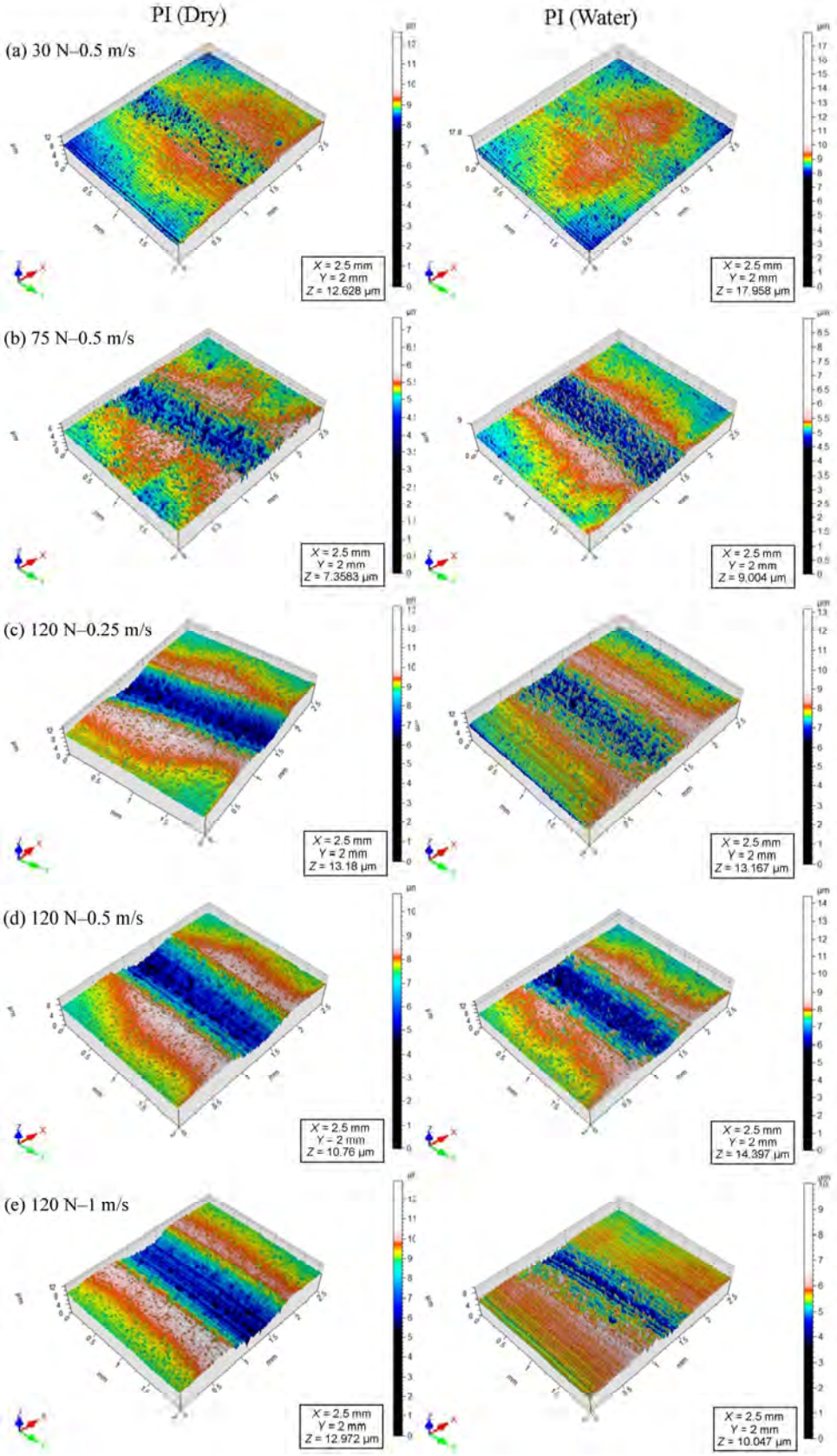

Fig. 11 3-D surface topography of PI materials after tests under different lubrications.

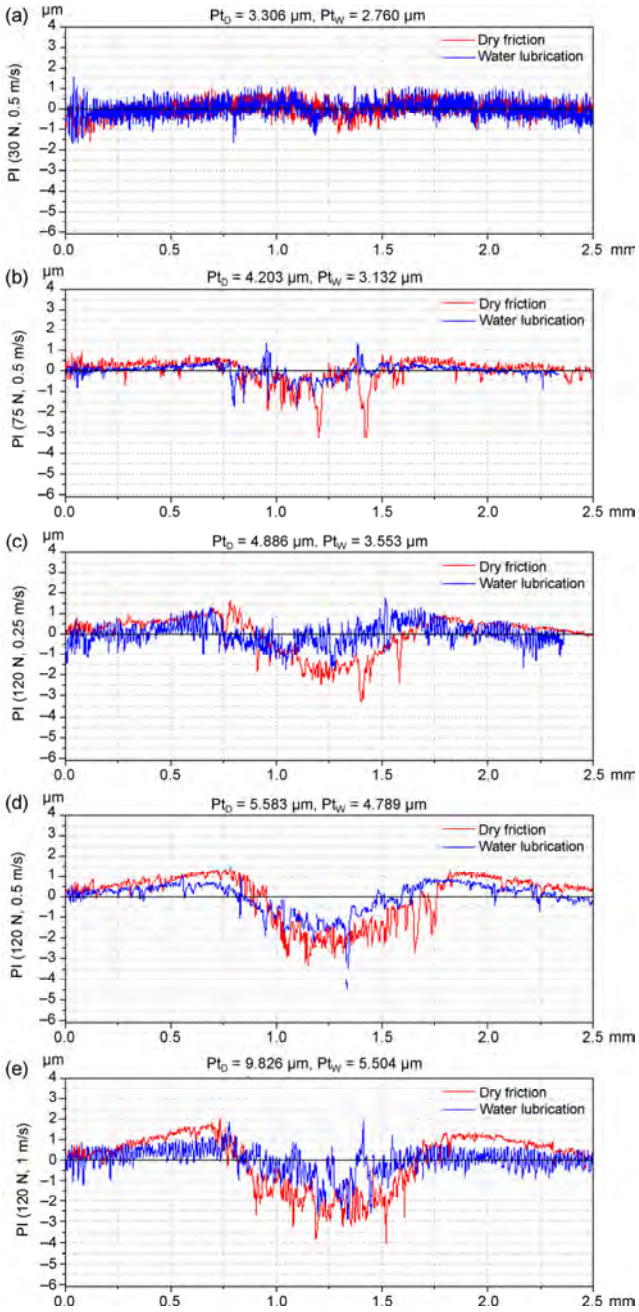

Fig. 12 Cross-sectional profiles of wear tracks from 2-D PI surface topography.

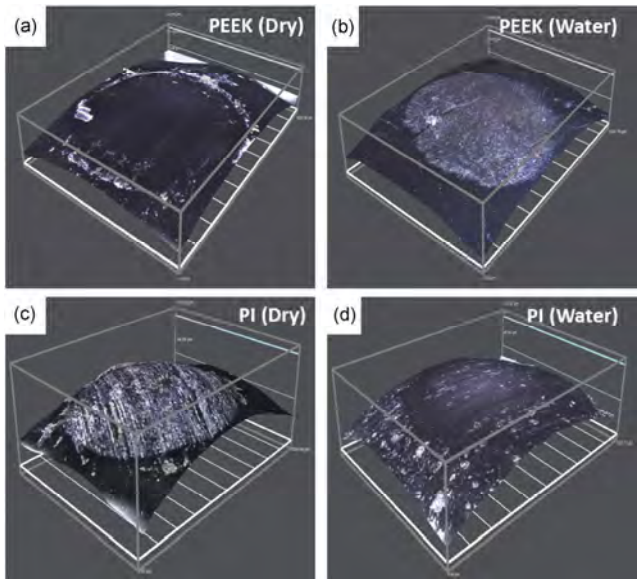

Fig. 13 Optical micrographs of Si_3N_4 ball sliding against PEEK disk (a, b) and PI disk (c, d) after tests under different lubrications.

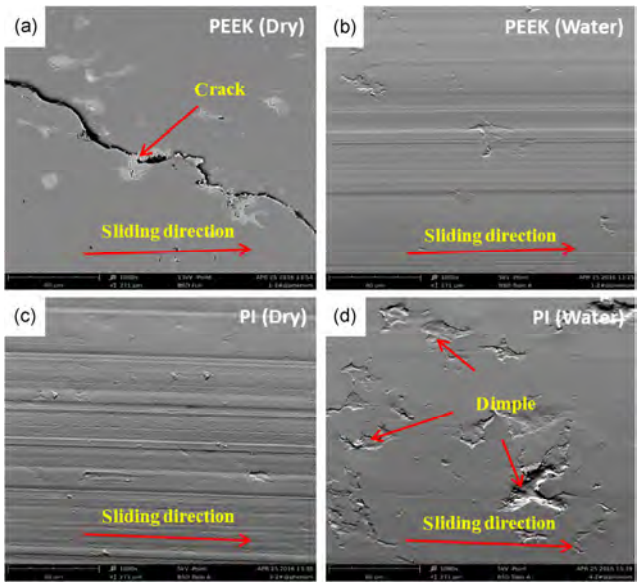

Fig. 14 SEM micrographs of PEEK disk (a, b) and PI disk (c, d) after tests under different lubrications: dry environment (a, c) and water environment (b, d).

different degrees of water absorption, which brought about swelling to reduce the shear strength. The lower surface strength induced lower friction coefficients, which was consistent with Refs. [63, 64]. On the other hand, one reason supported by Jia [65] was that the PI composite material easily contained a polar amide group bonding with the water molecules through hydrogen, which could lubricate the friction surface and reduce the wear rate by forming an adsorption water film.

The apparent dimples appeared on the PI tribopair surface under water after the test. Gao and Luo proposed that the friction coefficient was closely related to the surface topography and the lubricant viscosity. The resulting micro-textured surfaces significantly reduced the friction of the tribopair

contact during hydrodynamic lubricated sliding. The pits on the surface appeared and grew during the running-in process [68]. The generation of dimples on the worn surface was caused by the excessive wear and peeling of the solid lubricant MoS_2 added in the polymer. Moreover, the water absorption of the PI surface brought about a low shear strength, which would further aggravate the MoS_2 peeling.

The dimples in our experiments could be simplified into a circle, and the average diameter of the dimples was approximately 35 μm (Fig. 15). As reported in Refs. [66, 67], the surface of the specimens with a dimple diameter of 40 μm exhibited better lubricating effects than the untextured surface. The appearing surface dimples in our specimens also improved the tribological properties mainly because of their ability to generate hydrodynamic pressure lubricating effects. The dimples revealed more potential in improving the load-carrying capacity and friction properties than the smooth surface.

3.6 Microstructure analysis based on X-ray diffraction (XRD)

Some literatures reported that the tribochemistry of Si_3N_4 in a water medium played an important role on the tribological performance. A typical XRD spectrum of the composite PEEK and PI was designed to investigate the possibility with the hypothesis that the surface chemical corrosion may induce the changed tribological properties of specimens. Figure 16 shows

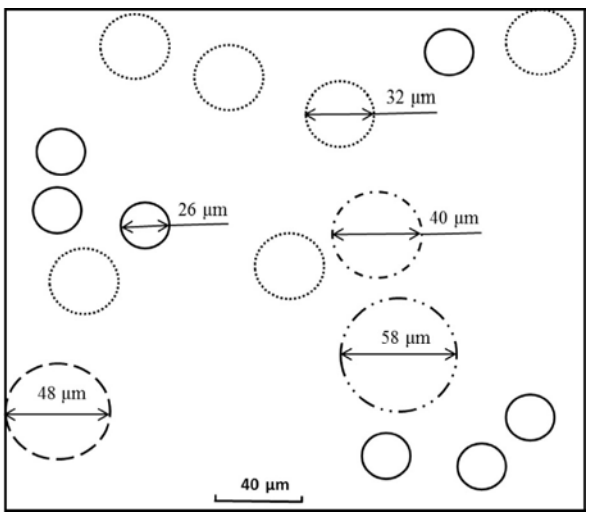

Fig. 15 Simplified patterns of PI surface texture under water after experiment.

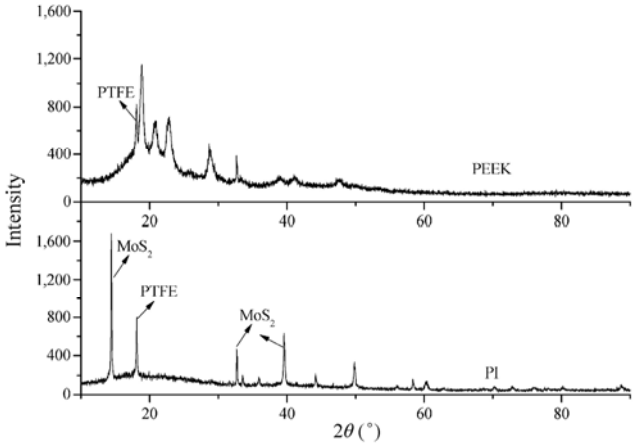

Fig. 16 Typical XRD spectrum of PEEK and PI materials after test.

that no new material was generated after the tests. With reference to Section 2.2, the Si_3N_4 ball hardness was far greater than that of the polymers. Furthermore, the wear volume losses of the Si_3N_4 ball were too little to be measured. Hence, the surface chemical corrosion was not responsible for the main wear mechanism.

5 Conclusions

This study presented the aqueous lubrication of tribopairs formed by PEEK and PI composite materials sliding against a Si_3N_4 ceramic. Two kinds of tribopairs showed different tribological properties. The conclusions drawn are as follows:

1. Water generates little influence on the PEEK–Si_3N_4 tribopair, and the minimum of the friction coefficient is 0.0425. However, the PI tribopair has lower friction coefficients under the lubricating condition. The minimum of which is 0.026, which is 41% lower than the minimum under the dry condition.

2. The wear rates of the PEEK tribopair under aqueous lubrication are approximately more than two times of those under dry sliding. Water makes the PI tribopair acquire less wear rates, and the values reduce by 32% on average than that at dry friction.

3. The wear surfaces of the PEEK– and PI–Si_3N_4 tribopairs have no chemical corrosion.

4. Water speeds up the transfer of the PEEK surface material in the PEEK–Si_3N_4 tribopair, thereby causing more severe wear rates. However, water inhibits the appearance of the crush phenomenon.

5. Compared with those of PEEK, the friction coefficients and wear rates of the PI tribopair could be reduced under water. Reasons are listed as following: (a) the PI surface has different degrees of water absorption, which brings about swelling to reduce the shear strength; (b) the polar amide group on the surface of the PI composite material bonding with the water molecules easily accelerates the formation of the lubrication water film; and (c) the dimples appearing on the PI tribopair surface under water generate additional hydrodynamic lubrication and further improve surface the friction properties.

Overall, compared with the PEEK tribopair, PI could withstand a greater applied load and a higher sliding velocity under water, making it promising for future applications in the water-based ceramic bearing industry.

Acknowledgements

This research was supported by the National Natural Science Foundation of China (Nos. 51375333, 50975199 and 51205285). Also the author thanks for all the members who have contributed their time and help in this research.

References

[1] Cong P H, Li T S, Xue Q J. Friction and wear of Polyimide and composite materials. *Lubrication Engineering* (04): 2–7 (1998)

[2] Cai H, Yan F Y, Chen J M, Xue Q J. Review on the Modification of Polyimide. *Journal of Materials Science and Engineering* **1**: 026 (2003)

[3] Hammouti S, Beaugiraud B, Salvia M, Mauclair C, Pascale-Hamri A, Benayoun S, Valette S. Elaboration of submicron structures on PEEK polymer by femtosecond laser. *Applied Surface Science* **327**: 277–287 (2015)

[4] Czichos H, Klaffke D, Santner E, Woydt M. Advances in tribology: the materials point of view. *Wear* **190**(2): 155–161 (1995)

[5] Michaljaničová I, Slepička P, Rimpelová S, Slepičková Kasálková N, Švorčík V. Regular pattern formation on surface of aromatic polymers and its cytocompatibility. *Applied Surface Science* **370**: 131–141 (2016)

[6] Hammouti S, Pascale-Hamri A, Faure N, Beaugiraud B, Guibert M, Mauclair C, Benayoun S, Valette S. Wear rate control of peek surfaces modified by femtosecond laser. *Applied Surface Science* **357**: 1541–1551 (2015)

[7] Mizobe K, Honda T, Koike H, Santos E C, Kashima Y, Kida K. Effect of PTFE retainer on friction coefficient in polymer thrust bearings under dry contact. *Advanced Materials Research* **683**: 90–93 (2013)

[8] Koike H, Mizobe K, Oyama S, Kashima Y, Kanemasu K, Kida K. Observation of wear on PEEK-PTFE hybrid radial bearings. *Advanced Materials Research* **683**: 385–390 (2013)

[9] Zhang Z, Breidt C, Chang L, Friedrich K. Wear of PEEK composites related to their mechanical performances. *Tribology International* **37**(3): 271–277 (2004)

[10] Aurélie D, Huong H T, Ahmad F, Aurore L, Guy L, Jalal B, Aissam A, Emmanuel A, Jean-François C. Improving adhesion of powder coating on PEEK composite: Influence of atmospheric plasma parameters. *Applied Surface Science* **357**: 1196–1204 (2015)

[11] Samyn P, Schoukens G, De Baets P. Micro-to nanoscale surface morphology and friction response of tribological polyimide surfaces. *Applied Surface Science* **256**(11): 3394–3408 (2010)

[12] Sun C, Zhou F, Shi L, Yu B, Gao P, Zhang J, Liu W. Tribological properties of chemically bonded polyimide films on silicon with polyglycidyl methacrylate brush as adhesive layer. *Applied Surface Science* **253**(4): 1729–1735 (2006)

[13] Zalaznik M, Kalin M, Novak S. Influence of the processing temperature on the tribological and mechanical properties of poly-ether-ether-ketone (PEEK) polymer. *Tribology International* **94**: 92–97 (2016)

[14] Koike H, Kida K, Mizobe K, Shi X, Oyama S, Kashima Y. Wear of hybrid radial bearings (PEEK ring-PTFE retainer and alumina balls) under dry rolling contact. *Tribology International* **90**: 77–83 (2015)

[15] Greco A C, Erck R, Ajayi O, Fenske G. Effect of reinforcement morphology on high-speed sliding friction and wear of PEEK polymers. *Wear* **271**(9): 2222–2229 (2011)

[16] Theiler G, Gradt T. Friction and wear of PEEK composites in vacuum environment. *Wear* **269**(3): 278–284 (2010)

[17] Guo X D, Dai Y, Gong M, Qu Y G, Helseth L E. Changes in wetting and contact charge transfer by femtosecond laser-ablation of polyimide. *Applied Surface Science* **349**: 952–956 (2015)

[18] Liu B, Pei X, Wang Q, Sun X, Wang T. Effects of proton and electron irradiation on the structural and tribological properties of MoS_2/polyimide. *Applied Surface Science* **258**(3): 1097–1102 (2011)

[19] Samyn P, Schoukens G. The effect of processing method on dry sliding performance of polyimides at high load/high velocity conditions. *European Polymer Journal* **44**(3): 716–732 (2008)

[20] Jia J H, Zhou H D, Gao S Q, Chen J M. A comparative investigation of the friction and wear behavior of polyimide composites under dry sliding and water-lubricated condition. *Materials Science and Engineering: A* **356** (1–2): 48–53 (2003)

[21] Riveiro A, Soto R, Comesana R, Boutinguiza M, del Val J, Quintero F, Lusquiños F, Pou J. Laser surface modification of PEEK. *Applied Surface Science* **258**(23): 9437–9442 (2012)

[22] Aurélie D, Huong H T, Ahmad F, Aurore L, Guy L, Jalal B, Aissam A, Emmanuel A, Jean-François C. Improving adhesion of powder coating on PEEK composite: Influence of atmospheric plasma parameters. *Applied Surface Science* **357**: 1196–1204 (2015)

[23] Tavenner E, Wood B, Curry M, Jankovic A, Patel R. Graphitic structure formation in ion implanted polyetheretherketone. *Applied Surface Science* **283**: 154–159 (2013)

[24] Laurens P, Sadras B, Decobert F, Arefi F, Amouroux J. Modifications of polyether-etherketone surface after 193 nm and 248 nm excimer laser radiation. *Applied Surface Science* **138**: 93–96 (1999)

[25] Feng Y, Gottmann J, Kreutz E W. Structuring of poly ether ether ketone by ArF excimer laser radiation in different atmospheres. *Applied Surface Science* **211**(1): 68–75 (2003)

[26] Almasi D, Izman S, Assadian M, Ghanbari M, Abdul Kadir M R. Crystalline ha coating on peek via chemical deposition. *Applied Surface Science* **314**: 1034–1040 (2014)

[27] Mackova A, Malinsky P, Miksova R, Khaibullin R I, Valeev V F, Svorcik V, Slepicka P, Slouf M. The characterization of PEEK, PET and PI implanted with Co ions to high fluences. *Applied Surface Science* **275**: 311–315 (2013)

[28] Faruque Ahmed S, Lee K R, Yoon J I, Moon M W. Nanoporous structures of polyimide induced by Ar ion beam irradiation. *Applied Surface Science* **258**(8): 3841–3845 (2012)

[29] Sun C, Zhou F, Shi L, Yu B, Gao P, Zhang J, Liu W. Tribological properties of chemically bonded polyimide films on silicon with polyglycidyl methacrylate brush as adhesive layer. *Applied Surface Science* **253**(4): 1729–1735 (2006)

[30] Ran J, Zhang J, Yao W, Wei Y. Properties of Cu film and Ti/Cu film on polyimide prepared by ion beam techniques. *Applied Surface Science* **256**(23): 7010–7017 (2010)

[31] Yang D, Dong Y, Gong J. The Tribological Behaviors of PEEK Filled PTFE Composites. *Lubrication Engineering* **38**(10): 60–63 (2013)

[32] Wang X. Investigation of tribological performance and simulation of temperature field during sliding contact for polyimide composites. Master Thesis. Nanjing Industrial University, 2005.

[33] Huang L J, Yang C C, Wang X D, Huang P. Tribological properties of polyimide composites against different metal under dry sliding friction condition. *Materials for Mechanical Engineering* **10**: 016 (2009)

[34] Wang X D, Wang X, Zhu P, Huang P. Mechanical properties and tribological performance of plastic. *Materials for Mechanical Engineering* **11**: 013 (2005)

[35] Samyn P, Schoukens G, Verpoort F, Van Craenenbroeck J, De Baets P. Friction and wear mechanisms of sintered and thermoplastic polyimides under adhesive sliding. *Macromolecular Materials and Engineering* **292**(5): 523–556 (2007)

[36] Dong W, Nie S, Zhang A. Tribological behavior of PEEK filled with CF/PTFE/graphite sliding against stainless steel surface under water lubrication. *Proceedings of the Institution of Mechanical Engineers, Part J: Journal of Engineering Tribology* **227**(10): 1129–1137 (2013)

[37] Zhang Z, Nie S, Yuan S, Liao W. Comparative Evaluation of Tribological Characteristics of CF/PEEK and CF/PTFE/Graphite Filled PEEK Sliding against AISI630 Steel for Seawater Hydraulic Piston Pumps/Motors. *Tribology Transactions* **58**(6): 1096–1104 (2015)

[38] Chen B, Wang J, Yan F. Friction and wear behaviors of several polymers sliding against GCr15 and 316 steel under the lubrication of sea water. *Tribology Letters* **42**(1): 17–25 (2011)

[39] Wu D, Liu Y, Yang S, Yang Z, Tang H. Friction and wear characteristics of WC–10Co–4Cr/Si_3N_4 tribopair lubricated under silt-laden water. *Wear* **294**: 370–379 (2011)

[40] Shi Y, Minami I, Grahn M, Björling M, Larsson R. Boundary and elastohydrodynamic lubrication studies of glycerol aqueous solutions as green lubricants. *Tribol Int* **69**: 39–45 (2014)

[41] Chen B, Wang J, Yan F. Microstructure of PTFE-based polymer blends and their tribological behaviors under aqueous environment. *Tribology Letters* **45**(3): 387–395 (2012)

[42] Guan X, Wang L. The tribological performances of multilayer graphite-like carbon (GLC) coatings sliding against polymers for mechanical seals in water environments. *Tribology Letters* **47**(1): 67–78 (2012)

[43] Liu H, Wang T, Wang Q. Tribological Properties of Thermosetting Polyimide/TiO_2 Nanocomposites Under Dry Sliding and Water-Lubricated Conditions. *Journal of Macromolecular Science, Part B* **51**(11): 2284–2296 (2012)

[44] Zhao H, Zhang J, Ji T, Yang M, Chao M, Kou K. Investigation of tribological properties of PI/FEP laminated composites under dry sliding, water-and oil-lubricated conditions. *Tribology Letters* **45**(2): 333–339 (2012)

[45] Deleanu L, Georgescu C. Water lubrication of PTFE composites. *Industrial Lubrication and Tribology* **67**(1): 1–8 (2015)

[46] Chen B, Wang J, Liu N, Yan F. Synergetic Effect of Lubricant Additive and Reinforcement Additive on the Tribological Behaviors of PEEK-Based Composites under Seawater Lubrication. *Tribology Transactions* **56**(4): 672–680 (2013)

[47] Zhang Z, Nie S, Liao W, Li L, Yuan S. Tribological behaviors of carbon fiber reinforced polyetheretherketone sliding against silicon carbide ceramic under seawater lubrication. *Proceedings of the Institution of Mechanical Engineers, Part J: Journal of Engineering Tribology* **228**(12): 1421–1432 (2014)

[48] Mimaroglu A, Unal H, Ozel A. Tribological Performance of Polyetheretherketone and its Composites under Water Environment. *Macromolecular Symposia* **327**(1): 108–113 (2013)

[49] Tomizawa H, Fischer T E. Friction and wear of silicon nitride and silicon carbide in water: hydrodynamic lubrication at low sliding speed obtained by tribochemical wear. *ASLE Transactions* **30**(1): 41–46 (1987)

[50] Li J J, Luo J B. Advancements in superlubricity. *Science China Technological Sciences* **56**(12): 2877–2887 (2013)

[51] Chen Z, Liu Y, Luo J. Superlubricity of nanodiamonds glycerol colloidal solution between steel surfaces. *Colloids and Surfaces A: Physicochemical and Engineering Aspects* **489**: 400–406 (2016)

[52] Lifang C, Chengya H, Xing H. Actuality and Prospect in Research on Friction and Wear Properties of Polymers and Polymer-based Composites. *Lubrication Engineering-Huangpu* **6**(172): 183 (2005)

[53] Zhao J, He Y, Wang Y, Wang W, Yan L, Luo J. An investigation on the tribological properties of multilayer graphene and MoS_2, nanosheets as additives used in hydraulic applications. *Tribology International* **97**:14–20 (2016)

[54] Yang Y, Zhang C, Wang Y, Dai Y, Luo J. Friction and wear performance of titanium alloy against tungsten carbide lubricated with phosphate ester. *Tribology International* **95**: 27–34 (2016)

[55] Xie G, Liu S, Guo D, Wang Q, Luo J. Investigation of the running-in process and friction coefficient under the lubrication of ionic liquid/water mixture. *Applied Surface Science* **255**(12): 6408–6414 (2009)

[56] Ma Z Z, Zhang C H, Liu S H, Luo J, Lu X, Wen S. Study of lubrication behavior of pure water for hydrophobic friction pair. *Science in China Series E: Technological Sciences* **52**(11): 3128–3134 (2009)

[57] Heshmat H, Jahanmir S. Tribological behavior of ceramics at high sliding speeds in steam. *Tribology Letters* **17** (3): 359–366 (2004)

[58] Satapathy B, Bijwe J. Analysis of simultaneous influence of operating variabales on the abrasive wear of phenolic Composite. *Wear* **253**: 787–794 (2002)

[59] Mens J W M, Gee A W J. Friction and wear behaviour of 18 polymers in contact with steel in environments of air and water. *Wear* **149**: 255–268 (1991)

[60] Zhang Z Y, Zhang M Q, Zeng H M, Liu Z R. On the tribological behavior and mechanism of Poly (etherether ketone). *Acta Materiae Compositae Sinica* 4 (1995)

[61] Unal H, Mimaroglu A, Kadıoglu U, Ekiz H. Sliding friction and wear behaviour of polytetrafluoroethylene and its composites under dry conditions. *Materials & Design* **25**(3): 239–245 (2004)

[62] Jia Z N, Hao C Z, Yan Y H. Effects of different operation conditions on the self lubricating properties of PI/PTFE composites. *CHINA PLASTICS INDUSTRY* **11**: 021 (2014)

[63] Jia J, Zhou H, Gao S, et al. The tribological behavior of carbon-fiber-reinforced polyimide composites under water lubrication. (in Chinese). *Mocaxue Xuebao* **22**: 273–276 (2002)

[64] Xiong D, Ge S. Friction and wear properties of UHMWPE/Al_2O_3 ceramic under different lubricating conditions. *Wear* **250**(1): 242–245 (2001)

[65] Jia J, Gao S, Chen J, et al. Tribological properties and wear mechanisms of PTFE and carbon fiber reinforced PI composites. (in Chinese). *Materials Science and Engineering* **21**: 183–186 (2003)

[66] Wang X, Adachi K, Otsuka K, Kato K. Optimization of the surface texture for silicon carbide sliding in water. *Applied Surface Science* **253**(3): 1282–1286 (2006)

[67] Wang X, Kato K, Adachi K, Aizawa K. Loads carrying capacity map for the surface texture design of SiC thrust bearing sliding in water. *Tribology International* **36**(3): 189–197 (2003)

[68] Gao Y, Ma L, Luo J. Pitted Surfaces Produced by lactic acid lubrication and their effect on ultra-low friction. *Tribology Letters* **57**(2): 1–8 (2015)

Anying WANG. She joined the Key Laboratory of Advanced Ceramics and Machining Technology of Ministry of Education at Tianjin University from 2013. Currently, she is a Ph.D. student in mechanical engineering at Tianjin University. Her research interests include ceramics tribology and polymer composite materials tribology.

Bin LIN. He was the lecturer, associate professor, and professor in the School of Mechanical Engineering at Tianjin University in 1994, 1996, and 2007, respectively. His current identity is a Doctoral supervisor and the Vice-director of the the Key Laboratory of Advanced Ceramics and Machining Technology of Ministry of Education. His research areas cover machining theory and machining technology of hard, brittle materials, and structural ceramics application theory and technology.

Friction **5**(4): 429–436 (2017)
DOI 10.1007/s40544-017-0156-8
ISSN 2223-7690
CN 10-1237/TH
RESEARCH ARTICLE

Preparation of Ag_2O modified silica abrasives and their chemical mechanical polishing performances on sapphire

Baichun ZHANG, Hong LEI*, Yi CHEN

Research Center of Nano-Science and Nano-Technology, Shanghai University, Shanghai 200444, China

Received: 02 November 2016 / Revised: 18 January 2017 / Accepted: 14 February 2017

Abstract: The chemical mechanical polishing (CMP) process has become a widely accepted global planarization technology. The abrasive material is one of the key elements in CMP. In the presented paper, an Ag-doped colloidal SiO_2 abrasive is synthesized by a seed-induced growth method. It is characterized by time-of-flight secondary ion mass spectroscopy and scanning electron microscopy to analyze the composition and morphology. The CMP performance of the Ag-doped colloidal silica abrasives on sapphire substrates is investigated. Experiment results show the material removal rate (MRR) of Ag-doped colloidal silica abrasives is obviously higher than that of pure colloidal silica abrasives under the same testing conditions. The surfaces that are polished by composite colloidal abrasives exhibit lower surface roughness (Ra) than those polished by pure colloidal silica abrasives. Furthermore, the acting mechanism of Ag-doped colloidal SiO_2 composite abrasives in sapphire CMP is analyzed by X-ray photoelectron spectroscopy, and analytical results show that element Ag forms Ag_2O which acts as a catalyst to promote the chemical effect in CMP and leads to the increasing of MRR.

Keywords: chemical mechanical polishing; Ag-doped colloidal silica abrasive; sapphire; material removal rate

1 Introduction

Sapphire possesses excellent optical and mechanical properties with good corrosion resistance and high hardness, and is widely used in solid lasers, infrared windows, semiconductor chip substrates, precision anti-friction bearings, and other high-tech fields [1–5]. Sapphire is well known as the substrate for gallium and indium nitride films and is used for fabricating light emitting diode devices [6]. With the rapid development of photoelectron technology, improvement of planarization efficiency and the study of planarization mechanism of sapphire have become more and more important to meet the increasing demand of higher surface quality [7]. As is known to all, sapphire substrates are difficult to be polished for their physical and chemical properties, such as high hardness, brittleness and so on. Chemical mechanical polishing (CMP) is used as one of the most effective ways to produce an atomic-level smooth surface [8–14].

During the CMP process, the abrasive was the most important factor that influenced the sapphire quality [15]. To improve surface planarization and the material removing rate (MRR) of sapphire, several polishing abrasives were studied. Xiong et al. [16] adopted silicon carbide, alumina, and silica sol as polishing abrasives for CMP on sapphire. Under the same condition, the results showed the Ra of sapphire polished with silica sol abrasive was lower than that with silicon carbide and alumina abrasives. The effect of the hardness of the abrasives on CMP of (0001) plane sapphire was researched by Zhu et al. [17], and the results showed that hard abrasives (such as monocrystalline and polycrystalline diamond, α-Al_2O_3) improve MRR of sapphire, but surface average roughness (Ra) increased. However, a lower Ra value could be reached by using silica sol as the polishing abrasive for sapphire,

* Corresponding author: Hong LEI, E-mail: hong_lei2005@163.com

but the MRR of sapphire was lower too. It could be concluded from the above examples that colloidal silica was widely regarded as the ideal polishing abrasive for sapphire CMP since it could achieve a better surface quality, but the MRR of sapphire with colloidal SiO_2 as a polishing abrasive still needed further research.

Silica-based composite particles were paid increasing attention on because the production process of silica was controllable and mature to combine with other materials. Xu et al. [18] reported the slurry of colloidal silicon dioxide (SiO_2) containing Fe-N_x/C exhibited higher MRR than the slurry containing pure SiO_2 abrasives in the CMP of sapphire substrates under the same conditions. Bai et al. [19] synthesized a kind of core-shell SiO_2/CeO_2 composite abrasive by calcining of the precursor under appropriate temperature and was used for sapphire CMP. The MRR decreased since the silica core had no direct contact with the sapphire CMP. In our previous work, silica/ceria nano composite abrasives [20] and alumina/silica core-shell abrasives [21] were prepared for hard disk CMP. Both showed high planarization efficiency and better planarization quality than pure silica abrasives under the same conditions. The examples above indicated silica-based composite abrasives resulted in both high planarization efficiency and good planarization quality. Recently, several kinds of abrasives were investigated to polish sapphire substrate, such as Mg-doped colloidal SiO_2 abrasives [22] and SiO_2/CeO_2 composite abrasives [19]. To further improve the sapphire CMP performances, new silica composite abrasives needed to be explored. In this paper, argentum ions modified silica (Ag-doped colloidal SiO_2) abrasives were synthesized by seed growth method, and the CMP performances on sapphire were investigated.

2 Materials and methods

Ag-doped colloidal SiO_2 abrasives were synthesized by a seed growth method.

A certain amount of sodium silicate (40 wt%, Jinan Dewang Chemical Industry Co., LTD, China) was diluted with water and passed through a column filled with 2 L of a strong cation exchange resin to produce silicic acid. During the ion exchange process, the sodium ions in the sodium silicate solution were replaced by hydrogen ions gradually. Finally, the 2.5 wt% silicic acid solution was obtained.

2.20 g silver nitrate ($AgNO_3$, Analytical Reagent (99.8%), Sinopharm Chemical Reagent Co., LTD, China) was dissolved in 1,395 g DI water to obtain a 0.01 mol/L silver ion solution. Then, the silver nitrate solution was mixed with the same weight of silicic acid. Next, the solution was added in drops into the crystal silica seed solution (40 wt%, Zhejiang Delixin Micro/Nano Science and Technology Co., LTD, China) to prepare a 0.5 wt% Ag-doped silica abrasive. The reaction took place in a four-neck flask under a 100 ℃ environment with constant stirring. During the reaction, sodium hydroxide (1 wt% NaOH, Analytical Reagent (96%), Sinopharm Chemical Reagent Co., LTD, China) was added to the basic solution to adjust the pH. Different Ag-doped contents of colloidal SiO_2 abrasives (0.5 wt%, 1.0 wt%, 1.5 wt%) were obtained by adding different amounts of silver nitrate during the reaction. When silver nitrate was dropped into the flask, argentum ions (Ag^+) of different amounts of silver nitrate combined with hydroxyl (OH^-) to form Ag_2O with different contents (0.5 wt%, 1.0 wt%, and 1.5 wt%) ($2Ag^+ + 2OH^- = Ag_2O + H_2O$). The experimental flow chart was shown in Fig. 1.

After the preparation of the slurry, it was used to polish the sapphire substrate. The substrate (sapphire crystals, Jiangsu Haohan Sapphire Science and Technology Co., LTD, China.) with c (0001) orientation was Φ 50.8 mm. The CMP experimental was performed on UNIPOL-1502 polishing equipment (Shenyang Kejing Instrument, Co. Ltd., China) with a Rodel

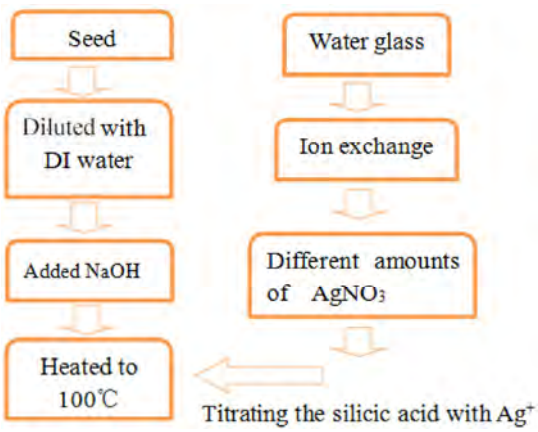

Fig. 1 The experimental flow chart of modified silica.

porous polyurethane pad. Then the sapphire was polished for 2 hours under 6 kg pressure with 60 rpm rotating speed and 180 mL/min slurry flow rate.

The Ag-doped colloidal SiO_2 was inspected with a scanning electron microscopy (SEM), time-of-flight secondary ion mass spectroscopy (TOF-SIMS), and X-ray photoelectron spectroscopy (XPS).

The SEM observations were performed with a JEOLJSM-6700F field emission scanning electron microscope with a voltage of 15.0 kV.

Elementary analysis of the modified silica was measured by time-of-flight secondary ion mass spectroscopy (TOF-SIMS, Model2100 Trift II) with a pulsed gallium ion beam with the energy of 15 kV. The analytical region was 200 μm × 200 μm and post acceleration was 5 kV/5 kV (+/−).

Mechanism analysis was characterized by X-ray photoelectron spectroscopy (XPS, ESCALAB 250Xi, 0.45 eV energy resolution and 3um spatial resolution). XPS spectra were obtained by using focused monochromatized Al K radiation (hv = 1,486.6 eV). The binding energy of C1s (284.6 eV) was used as reference.

The sapphire substrate was subjected to the MRR and surface average roughness (Ra). The MRR and Ra were the important factors to evaluate the performance of the slurry on sapphire under the same conditions. The Ra and polishing surface topography were measured by an Ambios XI-100 surface profiler (Ambios Technology Corp., USA, ZYGO) with a vertical resolution of 0.1 Å in texture modes. The measuring area was 500 μm × 500 μm. The depth of focus was 3.0 μm, the working distance was 7.4 mm, and the numerical aperture was 0.3. The mass of the sapphire substrates was measured by the analytical balance and all data were the means of four tests. The equation below was used to calculate the MRR.

$$\mathrm{MRR}=10^6\Delta m/(\rho\pi d^2 t) \quad (1)$$

(MRR—material removal rate (μm/h); m—mass of material removed (g); ρ—density of sapphire, 3.98 g/cm^3; d—diameter of sapphire, 50.8 mm; t—polishing time, 2 h)

3 Results and discussion

After the modification process, the colloidal silica particles, shown in Fig. 2(a), and Ag-doped silica

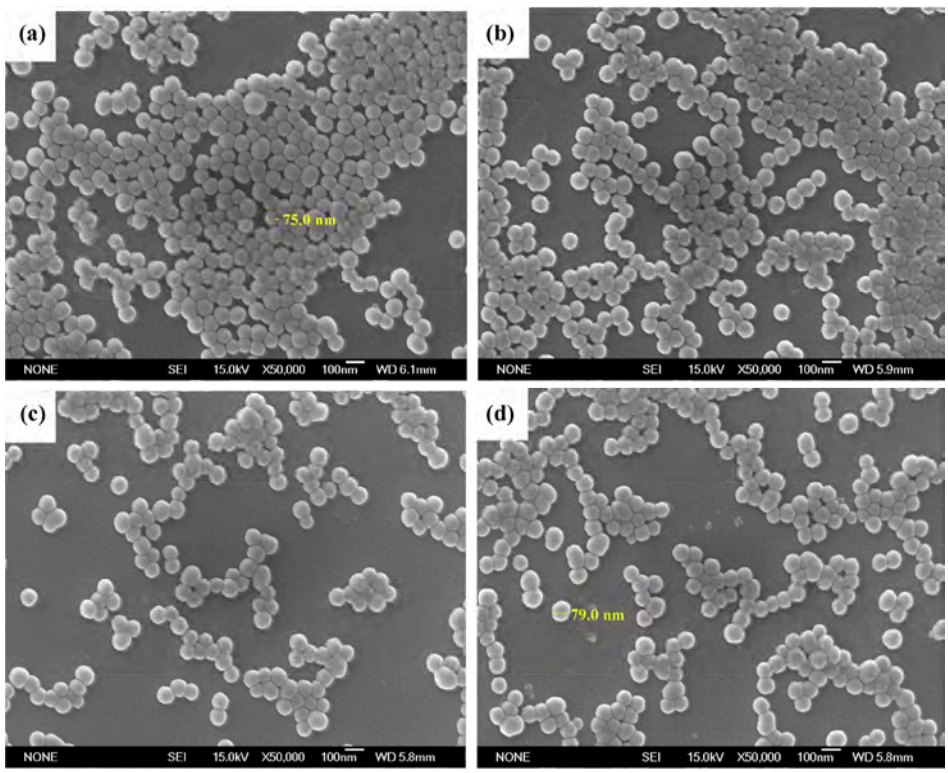

Fig. 2 The SEM images of colloidal silica abrasives and Ag-doped silica abrasives: (a) colloidal silica abrasives, (b) 0.5 wt% Ag_2O, (c) 1.0 wt% Ag_2O, and (d) 1.5 wt% Ag_2O.

abrasives with various contents of Ag_2O, shown in Figs. 2(b), 2(c), and 2(d), were observed by SEM. All particles were mono-dispersed with spherical appearance and were similar to the SiO_2/CeO_2 composite abrasives [19] and Mg doping colloidal SiO_2 abrasives [22].

To investigate whether the element Ag was absorbed into the abrasives, the colloidal silica abrasive and the modified silica abrasives were analyzed by TOF-SIMS (Fig. 3) to study the element composition of the compound which was an effect way to investigate the component of the abrasives. In Fig. 3, the *X* axis was the relative atomic mass, and the *Y* axis represented the intensity of the element in the sample. The argentum peak in Fig. 3(b) showed the evidence of surface modification of colloidal silica via this process by comparing it with Fig. 3(a).

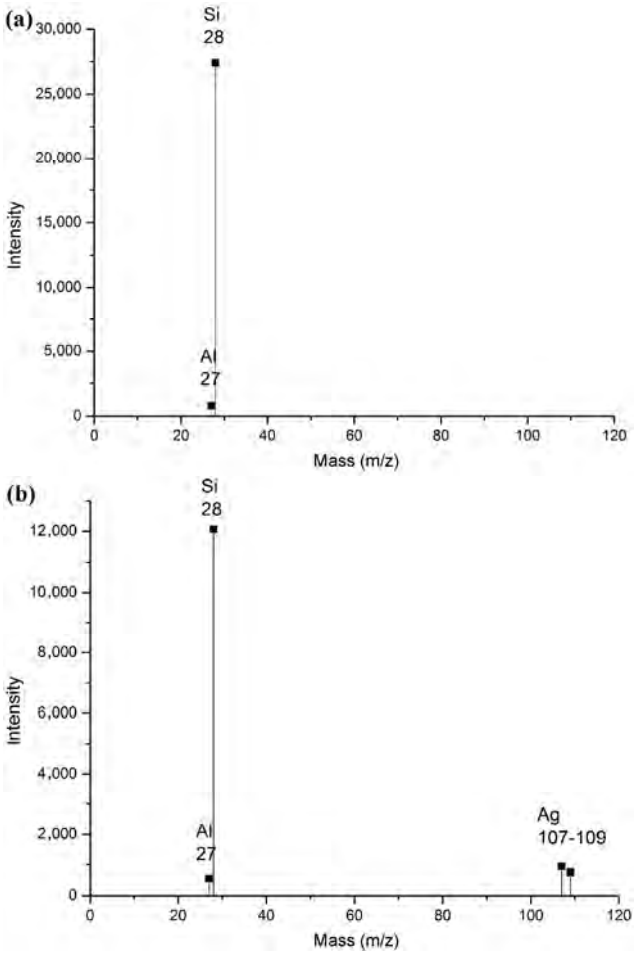

Fig. 3 TOF-SIMS spectrum of the colloidal silica abrasive (a) and Ag-doped colloidal silica abrasive containing 1.5 wt% Ag_2O (b).

Figure 4 showed the relationship between the MRR and the mass content of Ag_2O. With an increased content of Ag_2O, the MRR increased rapidly. The MRR increased steeply from 0.324 μm/h to 0.724 μm/h when the content of Ag_2O ranged from 0 to 1.5 wt%. The MRR of sapphire substrates polished by pure colloidal SiO_2 abrasive was 0.324 μm/h. When the content of Ag_2O reached 1.5 wt%, the MRR was two times greater than pure colloidal SiO_2 abrasive. In other words, the prepared Ag-doped colloidal SiO_2 composite abrasives possessed a higher MRR than pure colloidal SiO_2 abrasives. Meanwhile, when it was compared with the SiO_2/CeO_2 composite abrasive [19] and Mg-doped abrasive [22], the MRR of Ag-doped abrasive (0.724 μm/h) was much more than the SiO_2/CeO_2 composite abrasive (0.295 μm/h) and Mg-doped abrasive (0.617 μm/h). Ag-doped abrasive exhibited much better CMP performance on the MRR than the other two.

Surface roughness of sapphire was presented in Fig. 5. It was observed in Fig. 5 that surface roughness decreased linearly with the mass content of Ag_2O ranging from 0 wt% to 1.5 wt%. All Ra values of sapphire substrates polished by slurries containing Ag-doped silica composite abrasives obviously decreased when compared with the pure silica abrasive under the same testing conditions. When the content of Ag_2O reached 1.5 wt%, the sapphire substrate had the minimum value (0.854 nm). The result of the

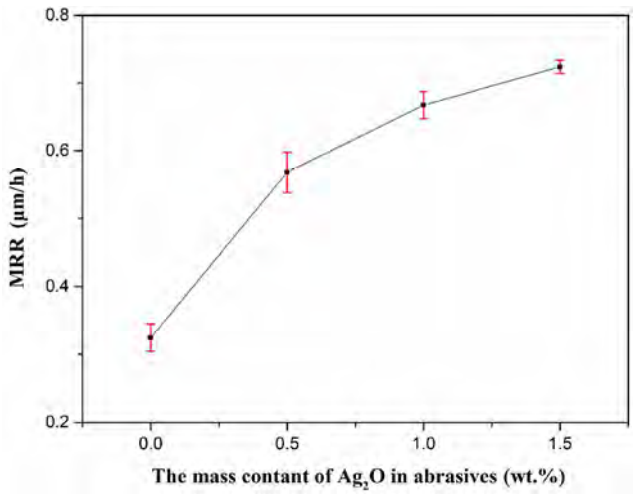

Fig. 4 The relationship between MRR and the mass content of Ag_2O in abrasives (red line is the error bar).

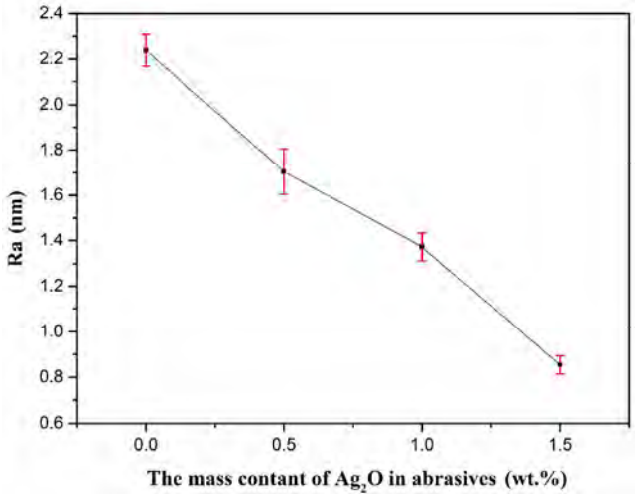

Fig. 5 The relationship between Ra and the mass content of Ag_2O in abrasives (red line is the error bar).

MRR and Ra suggested that colloidal silica abrasives after Ag modifying not only increased the removal rate but also improved the surface quality.

Figure 6 showed the surface morphology analysis of the sapphire substrate. It was performed by the AMBIOS TECHNOLOGY XI-100 Optical Surface Profiler. The surface morphology of the sapphire substrate before polishing was shown in Fig. 6(a). Figure 6(b) depicted surface profiles of sapphire polished by colloidal silica abrasives. Figure 6(c) depicted surface profiles of sapphire polished by Ag-doped colloidal silica with the mass content of 1.5 wt% Ag_2O in abrasive. In Fig. 6, it was obviously that Figs. 6(a) and 6(b) demonstrated wavier behavior than Fig. 6(c) whose surface was smoother and the topography fluctuation could hardly be observed. The peak-valley values of Figs. 6(a) and 6(b) were bigger than Fig. 6(c). A better surface could be reached by using Ag-doped colloidal silica abrasive to polish the sapphire substrate.

To further study the removal mechanism of sapphire, the Ag-doped colloidal silica containing 1.5 wt% Ag_2O after polishing was subjected to XPS in Fig. 7. After the slurry was dried in the oven, the residuum was ground into powder in the agate mortar. Finally, it was analyzed by XPS.

The XPS spectrum of element Si 2p, Al 2p, and Ag 3d was presented above. The binding energy of various substances was displayed in Tables 1–3. The black line was the real total intensity measured by

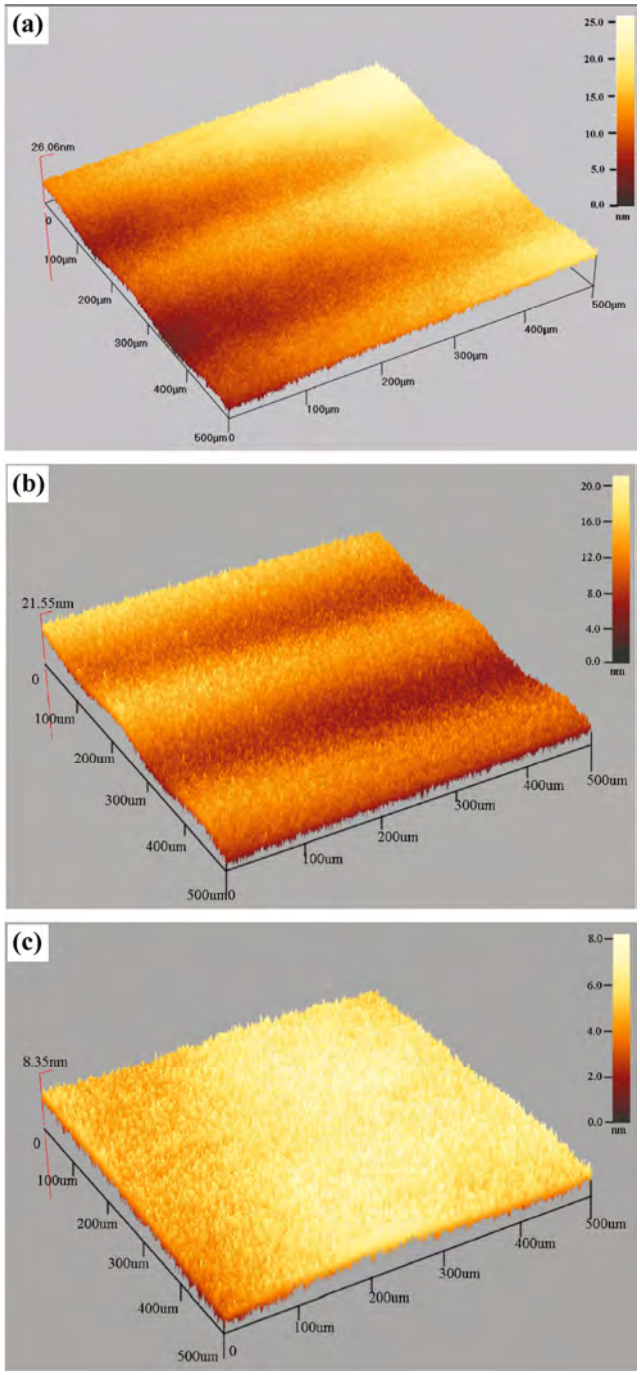

Fig. 6 Surface profiles of sapphire (a) before polishing (Ra = 3.62 nm), (b) polished by colloidal silica (Ra = 2.24 nm), and (c) polished by Ag-doped colloidal silica containing 1.5 wt% Ag_2O (Ra = 0.85 nm).

XPS test, and the green line was the total intensity after curve fitting by using the Thermo Avantage software. The overlap ratio between the real result (black line) and the fitting result (green line) contributed to more accurate measurement results.

In Fig. 7, the peak at the binding energy (BE) of 102.3 eV (Fig. 7(a)) corresponded to Si 2p of SiO_2, which were the fundamental particles of the slurry [23]. The BE at 103.1 eV (Fig. 7(a)) was in conformity with Si 2p of Al_2SiO_5 here. At the same time, the peak at

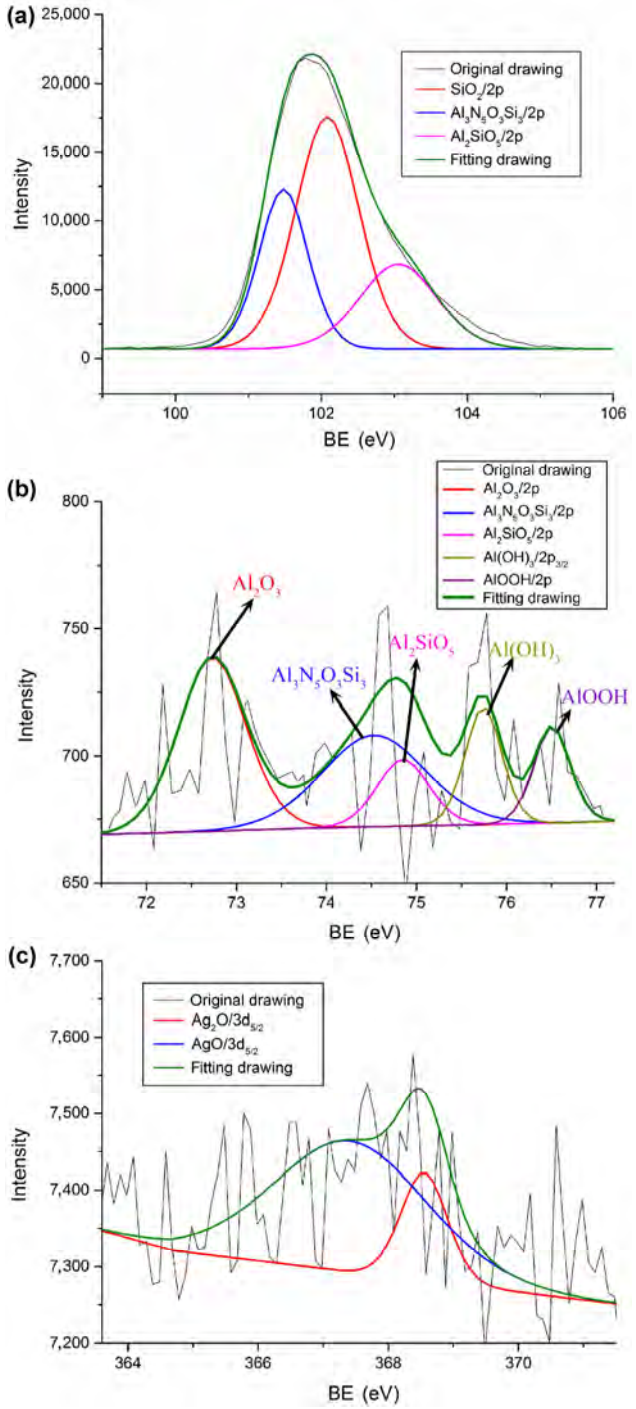

Fig. 7 XPS spectra of element Si, Al, and Ag in abrasives containing Ag-doped colloidal SiO_2 with 1.5 wt% Ag_2O after polishing: (a) Si 2p, (b) Al 2p, and (c) Ag 3d.

Table 1 Binding energy of Si 2p.

Chemical state	Binding energy (eV)
$Al_3N_5O_3Si_3$	101.7
SiO_2	102.3
Al_2SiO_5	103.1

Table 2 Binding energy of Al 2p.

Chemical state	Binding energy (eV)
Al_2O_3	72.73
$Al_3N_5O_3Si_3$	74.50
Al_2SiO_5	74.91
$Al(OH)_3$	75.77
AlOOH	76.63

Table 3 Binding energy of Ag 3d.

Chemical state	Binding energy (eV)
AgO	367.3
Ag_2O	368.6

74.91 eV in Fig. 7(b) which corresponded to Al 2p of Al_2SiO_5. This situation showed that SiO_2 might react with the sapphire, and Al_2SiO_5 might be the product. The possibility of chemical reaction during the CMP process was as follows:

$$SiO_2 + Al_2O_3 = Al_2SiO_5 \quad (2)$$

That guess was proven by Vovk who revealed that aluminum silicate with the composition Al_2SiO_5 could be formed on the polished surface and the silicon-containing near-surface layer thickness was about 20 nm [24]. The CMP process occurred on the surface activated by the destruction of interatomic bonds after an amorphous silicon-containing layer was removed under the mechanical frictional action of silica particles on sapphire surface.

In Fig. 7(b), the peaks at the BE of 75.77 eV and 76.63 eV of Al 2p XPS spectra were intermediate products ($Al(OH)_3$ and AlOOH). The forming process could be described as

$$Al_2O_3 + H_2O = 2AlOOH \quad (3)$$

$$AlOOH + H_2O = Al(OH)_3 \quad (4)$$

In addition, the peak at BE of 74.50 eV in Fig. 7(b) corresponded to Al 2p of $Al_3N_5O_3Si_3$, the peak at BE of 101.7 eV in Fig. 7(a) corresponded to Si 2p of

$Al_3N_5O_3Si_3$ [25]. In Fig. 7(c), the Ag 3d peak met with AgO at 367.3 eV. The peak at BE of 368.6 eV (Fig. 7(c)) corresponded to Ag_2O. Compared with the colloidal silica, Ag-doped colloidal silica abrasives were more effective on sapphire CMP. However, argentum did not form the new compound during the CMP process as referred to Fig. 7(c). Therefore, argentum might act as a catalyst to accelerate the reaction between sapphire and Ag-doped colloidal silica. The equations were deduced as follows:

$$2Ag^+ + 2OH^- = Ag_2O + H_2O \quad (5)$$

$$3SiO_2 + 3AlOOH + 5NO_3^- + 20Ag_2O + H_2O = Al_3N_5O_3Si_3 + 4AgO + 5OH^- \quad (6)$$

$$2AgO + H_2O + 2e^- = Ag_2O + 2OH^- \quad (7)$$

Compared to polishing with pure silica abrasive, Ag-doped colloidal SiO_2 abrasives had a great enhancement in MRR and Ra which could be explained by the chemical equations above. The addition of argentum ions could promote the reaction between abrasives and sapphire.

4 Summary

Ag-doped colloidal SiO_2 abrasives were synthesized by a seed-induced growth method. The Ag-doped colloidal SiO_2 abrasive was effective and improved polishing performance of sapphire. At the content of 1.5 wt% Ag_2O, the MRR was two times greater than the pure SiO_2 abrasive. The Ra decreased from 3.62 nm to 0.85 nm. During the polishing process, Ag_2O was formed and acted as a catalyst to accelerate the reaction between the slurry and sapphire during the CMP process.

Acknowledgments

This work was supported by the National Natural Science Foundation of China (Nos. 51475279).

References

[1] Gentilman R L, Maguire E A, Starrett H S, Hartnett T M, Kirchner H P. Strength and transmittance of sapphire and strengthened sapphire. *J Am Ceram Soc* 64(9): C-116–C-127 (1981)

[2] Li J, Nutt S R, Kirby K W. surface modification of sapphire by magnesium-ion implantation. *J Am Ceram Soc* **82**(11): 3260–3262 (1999)

[3] Niu X, Liu Y. Method of surface treatment on sapphire substrate. *Trans Nonferrous Met Soc China* **16**: s732-s734 (2006)

[4] Park H, Chan H M. A novel process for the generation of pristine sapphire surfaces. *Thin Solid Films* **422**(1): 135–140 (2002)

[5] Nakamura S. InGaN-based laser diodes. *Annual Review of Materials Research* **28**(1): 125–152 (2003)

[6] Duboz J Y. GaN as seen by the industry. *Phys Status Solidi A* **171**(1): 5–14 (1999)

[7] Shi X, Pan G, Zhou Y. A study of chemical products formed on sapphire (0001) during chemical–mechanical polishing. *Surf Coat Technol* **270**: 206–220 (2015)

[8] Lee H, Park S, Jeong H. Evaluation of environmental impacts during chemical mechanical polishing (CMP) for sustainable manufacturing. *J Mech Sci Technol*. **27**(2): 511–518 (2013)

[9] Deng H, Endo K, Yamamura K. Competition between surface modification and abrasive polishing: A method of controlling the surface atomic structure of 4H-SiC(0001). *Sci Rep* **5**: 1–5 (2015)

[10] Zhu H, Tessaroto L A, Sabia R. Chemical mechanical polishing(CMP) anisotropy in sapphire. *Appl Surf Sci* **236**: 120–130 (2004)

[11] Xu W, Lu X, Pan G, Lei Y, Luo J. Effects of the ultrasonic flexural vibration on the interaction between the abrasive particles: pad and sapphire substrate during chemical mechanical polishing (CMP). *Appl Surf Sci* **257:** 2905–2911 (2011)

[12] Merricks D. Alumina abrasives for sapphire substrate polishing. *ECS Trans* **32**(1): 1035–1039 (2011)

[13] Aida H, Doi T, Takeda H , Katakura H, Kim SW, Koyama K, Yamazaki T, Uneda M. Ultraprecision CMP for sapphire, GaN, and SiC for advanced optoelectronics materials. In *the 2nd International Symposium on Hybrid Materials and*

Processing (HyMaP), Busan, South Korea, 2011: S41–S46.

[14] Xu W, Lu X, Pan G, Lei Y, Luo J. Ultrasonic flexural vibration assisted chemical mechanical polishing for sapphire substrate. *Appl Surf Sci* **256:** 3936–3940 (2010)

[15] Wang L Y, Zhang K L, Song Z T, Feng S L. Chemical mechanical polishingand a succedent reactive ion etching processing of sapphire wafer. *J Electrochem Soc* **154**(3): H166–H169 (2007)

[16] Xiong W, Chu X F, DongY P, Bi L, Ye M F, Sun W Q. Effects of different abrasives on sapphire chemical-mechanical polishing. *J Synth Cryst* **42**(6): 1064–1069 (2013)

[17] Zhu H L. Chemical mechanical polishing(CMP) of sapphire. Ph.D Thesis. New Jersey (America): Rutgers, the State University of New Jersey, 2002.

[18] Xu L, Zou C L, Shi X L, Pan G S, Luo G H, Zhou Y. Fe-Nx/C assisted chemical-mechanical polishing for improving the removal rate of sapphire. *Appl Surf Sci* **343**: 115–120 (2015)

[19] Bai L S, Xiong W, Chu X F, Dong Y P, Zhang W B. Preparation of nano SiO_2/CeO_2 composite particles and their application to CMP on sapphire substrates. *Optics and Precision Engineering* **22**(5): 1289–1295 (2014)

[20] Lei H, Chu F, Xiao B. Preparation of silica/ceria nano composite abrasive and its CMP behavior on hard disk substrate. *Microelectron Eng* **87**: 1747−1750 (2010)

[21] Lei H, Zhang P. Preparation of alumina/silica core-shell abrasives and their CMP behavior. *Appl Surf Sci* **253**: 8754−8761 (2007)

[22] Ma P, Lei H, Chen R L. Preparation of Mg-doped colloidal silica abrasives and their chemical mechanical polishing performances on sapphire. *Nanoscience and Nanotechnology* **16**(9): 9951–9957 (2016)

[23] Hughes A E, Sexton B A. Comments on the use of implanted Ar as a binding energy reference. *J Electron Spectrosc Relat Phemon* **50**(2): c15–c18 (1990)

[24] Vovk E A, Budnikov A T, Dobrotvorskaya M V, Krivonogov S I, Dan'ko A Y. Mechanism of the interaction between Al_2O_3 and SiO_2 during the chemical-mechanical polishing of sapphire with silicon dioxide. *Journal of Surface Investigation, X-ray, Synchrotron and Neutron Techniques* **6**(1): 115–121 (2012)

[25] Hagio T, Takase A, Umebayashi S. X-ray photoelectron spectroscopic studies of beta-sialons. *J Mater Sci Lett* **11**: 878 (1992)

Baichun ZHANG. He received his bachelor degree in polymer materials and engineering in 2014 from Qingdao University, Shandong, China. Now, he is a master candidate in the Research Center of Nano-Science and Nano-Technology, Shanghai University. His research interest is chemical mechanical polishing.

Hong LEI. He received his M.S. and Ph.D. degrees in applied chemistry from Huazhong University of Science and Technology in 1996 and 2001, respectively. He joined Shanghai University from 2003. His current position is a professor in the Research Center of Nano-Science and Nano-Technology, Shanghai University. His research interests include functional abrasives, CMP slurry, and post-CMP cleaning.

Friction **5**(4): 437–446 (2017)
DOI 10.1007/s40544-017-0157-7
ISSN 2223-7690
CN 10-1237/TH
RESEARCH ARTICLE

Friction and wear behavior of Cu–4 wt.%Ni–TiC composites under dry sliding conditions

Pushkar JHA*, Rakesh Kumar GAUTAM, Rajnesh TYAGI

Department of Mechanical Engineering, Indian Institute of Technology (Banaras Hindu University), Varanasi 221005, India

Received: 19 December 2016 / Revised: 28 January 2017 / Accepted: 17 February 2017

Abstract: The present study synthesized Cu–4 wt% Ni matrix composites reinforced with different percentages of TiC (0, 2, 4, 6, and 8 wt%) through high-energy ball milling, followed by compaction and sintering. The friction and wear behavior was examined at four different normal loads of 5, 10, 15, and 20 N. A constant sliding speed of 1.25 m/s was maintained while sliding against a hardened counterface made of EN31 steel (HRC 60) under ambient conditions using a pin-on-disk test rig. The composite hardness increased until the addition of 4 wt% of TiC, beyond which it was observed to decrease. Such a trend may be attributed to the TiC agglomeration in the composites containing relatively larger amounts of TiC (i.e., 6 and 8 wt%). The wear rate linearly increased with the load. However, the composites exhibited a lower rate of wear than the matrix alloy, which may have resulted from the relatively higher hardness of composites. The observed friction and wear behavior has been explained on the basis of hardness and presence of the transfer layer on the worn surface and its nature, i.e., loose or well compacted. Addition of 4 wt% TiC showed the optimum performance in terms of friction and wear caused by its higher hardness and ability to hold a transfer layer of a relatively larger thickness compared to the other materials. The wear mechanism for the Cu4Ni matrix alloy was a mix of adhesive and oxidative wear and primarily abrasive for the composites containing hard TiC particles.

Keywords: sliding wear; composites; TiC particles; friction

1 Introduction

Metal matrix composites (MMCs) have attained growing importance because of their potential applications in the automobile, aerospace, sporting goods and general engineering industries due to their excellent properties (e.g., high specific strength, elastic modulus, specific stiffness, desirable coefficient of thermal expansion, elevated temperature resistance, and superior wear resistance) [1]. Discontinuously reinforced MMCs are endowed with properties, such as low fabrication cost and utilization in various industrial purposes [2–4]. Copper-based MMCs are promising materials because of their excellent thermo-physical properties. They are also being used in several industrial applications, such as in brush and torch nozzle materials, electrical sliding contact materials in homopolar machines, and railway overhead current collector systems, where good wear resistance at a reasonable level of electrical conductivity is the prime requirement [5, 6]. Several processing techniques, including powder metallurgy, casting, and infiltration techniques, have been developed and are being used to synthesize MMCs [7]. However, the powder metallurgy route has an edge over liquid-processing methods because it overcomes the problems of porosity, non-uniform distribution of reinforcing particles, and unwanted chemical reactions, which are a part and parcel of the casting route. It also results in the production of good quality products, particularly, when the ceramic particles are reinforced into the matrix material [8]. The agglomeration of the reinforcement particles in

* Corresponding author: Pushkar JHA, E-mail: pj.rs.mec@iitbhu.ac.in

the matrix, particularly in the case of small-sized reinforcement particulates, can be prevented by mechanical alloying that involves repeated deformation, cold welding, and fracture of powder using high-energy ball milling and further leads to a homogeneous distribution of the reinforcement phase in the matrix [9].

Researchers have reinforced various oxides, carbides, and borides in copper to enhance its mechanical and wear resistance properties [10–13]. Among these reinforcements, titanium carbide is considered attractive because of its higher modulus, hardness, and melting temperature [14]. TiC particles reinforced with copper-based composites have recently been explored because of their numerous industrial applications in electrodes, switches, motors, etc. [15–19]. Ni is used in the present investigation as a binding agent between Cu and TiC [20].

A critical review of the literature presented above clearly reveals that various studies were conducted on the mechanical and physical properties of Cu-based composites containing different reinforcements. However, only limited investigations were made toward understanding the friction and wear behavior of TiC-reinforced Cu-based composites. Hence, the present study aims to highlight the Cu-based composites through high-energy ball milling, followed by compaction and sintering containing different amounts of TiC particles. The main focus of the investigation is to evaluate and understand the friction and wear performance of the synthesized composites containing different amounts of reinforcement by performing dry sliding wear tests using a pin-on-disk tribometer under different normal loads of 5, 10, 15, and 20 N and maintaining a constant sliding speed of 1.25 m/s. The exploration equally attempts to study the effective mechanisms of wear taking place in the present circumstances.

2 Experimental procedure

2.1 Materials

Copper and nickel with 99% purity (Loba Chemie Pvt. Ltd., India) having an average particle size of 200 mesh and TiC particles (325 mesh, 98%, Sigma Aldrich, Germany) as the reinforcement were used to make the Cu–4 wt% Ni–x wt% TiC (x = 0, 2, 4, 6, and 8) metal matrix composite. These composites were designated as Cu4Ni, Cu4Ni–2TiC, Cu4Ni–4TiC, Cu4Ni–6TiC, and Cu4Ni–8TiC, respectively. Formulated composite powders were ground in a high-energy ball mill for 120 min at 400 rpm in the presence of toluene, which acted as the process control agent and restricted the generation of intermetallic compounds. Hardened stainless steel vial was used to seal the powders, and the ball-to-powder ratio was 10:1. The high-energy wet ball milling was rested periodically for every 20 min, then resumed for another 20 min to avoid overheating. The ground mixes were compacted by cold uniaxial pressing in a rigid cylindrical die at an optimized pressure of 650 MPa. For the friction-free punch movement, stearic acid was applied on the inner surface of the die as a lubricant. The compacted samples measured 12 mm × 11 mm. Green pellets were sintered in an argon atmosphere at an optimized sintering temperature of 850 ℃ for a soaking time of 60 min.

2.2 Characterization

The phase evolution of the sintered composites was studied using a Rigaku Desktop Miniflex II X-ray diffractometer with Cu-Kα (λ = 15.406 nm). The composite microstructure was examined using a ZEISS (model no. EVO/18) scanning electron microscope (SEM) equipped with energy dispersive spectroscopy (EDS). The sintered density of the samples was measured using Archimedes' principle. The Vickers micro-hardness test was performed for 15 s using a Vaiseshika electron micro-hardness tester (DHV-1000) with a load of 100 g. A minimum of ten different measurements was taken. The average value of the micro-hardness was reported accordingly.

2.3 Friction and wear tests

The friction and wear tests were conducted according to the ASTM G99-05 standard using a pin-on-disk tribometer (Magnum Engineers, Bangalore, India) with a counterface of the EN31 steel hardened to 60 HRC at an ambient temperature. Figure 1 shows a schematic diagram of the pin-on disk wear tester. The pin-shaped specimens were ground with a 800-grit SiC paper prior to the wear test. The applied normal

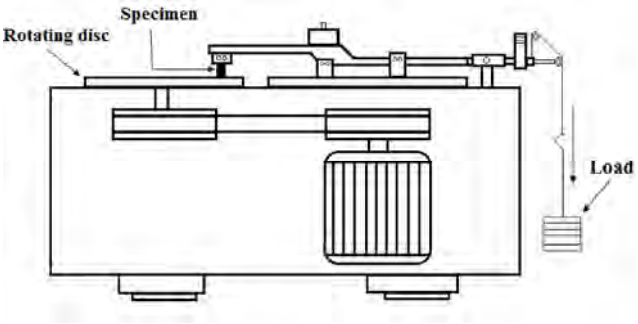

Fig. 1 Schematic of pin-on-disc wear test machine.

loads were 5, 10, 15, and 20 N, and the sliding speed was fixed at 1.25 m/s. The total sliding distance covered during the wear test was 2,250 m. The weight loss during the wear test of each specimen was measured prior to and after the test using an electronic balance with an accuracy of 0.1 mg. Meanwhile, the volume loss of the samples was calculated through weight loss divided by Archimedes' density of the material. The control panel equipped with the tribometer displayed the frictional force. The same was used to calculate the friction coefficient by dividing it by the normal load. Each test for a particular condition of load and speed was conducted thrice. The average value of three tests was reported in the present investigation. The worn surface of the specimens was subjected to SEM and EDS analyses to explore the nature of the wear mechanism.

3 Results and discussion

3.1 Microstructural characterization

Figure 2 shows the X-ray diffraction patterns of the matrix alloy and the TiC-reinforced composites revealing the occurrence of the Cu and TiC peaks, which indicated that no intermetallic compounds or other oxide phase formation took place during the sintering process. The spectra also evidently illustrated that the TiC peaks became distinct only beyond a certain amount of its addition. The peaks corresponding to the presence of Ni could not be detected in the spectra because it goes into making a solid solution due to complete solubility in copper.

Figure 3 presents the SEM morphology of the Cu4Ni matrix alloy and the other composites developed via high-energy ball milling followed by compaction and

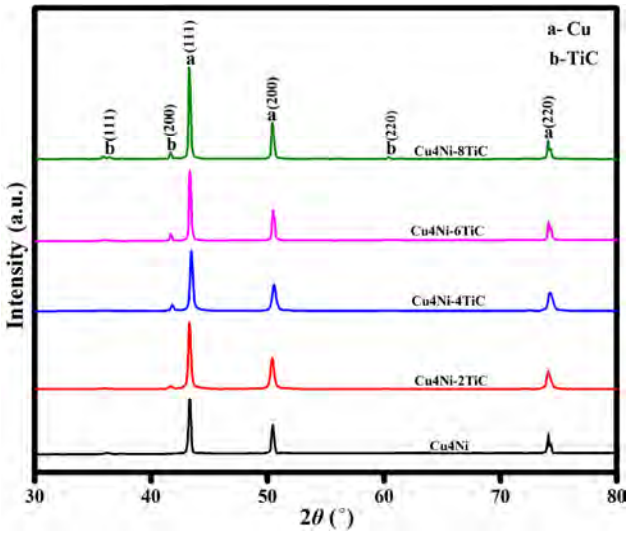

Fig. 2 XRD patterns of Cu4Ni–*x* wt% TiC (*x* = 0, 2, 4, 6 and 8) composites sintered at 850 ˚C.

sintering. The micrographs showed light and dark gray areas and sharp-edged particles representing copper, porosity, and TiC particles, respectively. The TiC particles appeared to be uniformly distributed in the matrix alloy, as seen from Figs. 3(b) to 3(e). No cracks could be observed in the micrographs. A uniform distribution of the reinforced particles resulted in the improvement of the composites' mechanical properties [21]. Furthermore, the addition of a relatively higher amount of TiC particles may result in the agglomeration leading to the formation of pores in the composites, which could also be observed from the micrographs in Figs. 3(b)–3(e) in round circles [22]. The agglomeration can be seen in the inset of Fig. 3(e). Figures 4(a) and 4(b) present the EDS analysis of the marked portion of the micrographs: (a) Cu4Ni-4TiC and (b) Cu4Ni-8TiC. The EDS analysis in Fig. 4(a) clearly demonstrated that the Cu, Ni, Ti, and C peaks appeared in the EDS spectra, whereas those of Ti and C appeared in the EDS spectra in Fig. 4(b). The TiC was present in the composite, and no oxygen peak was observed in the spectra, suggesting that no oxidation occurred during the sintering process.

3.2 Density and micro-hardness behavior

Figure 5 depicts the effect of the TiC addition on the matrix alloy density. The density enhanced to 7.96 gm/cm^3 when the TiC content was 4 wt% and deteriorated, afterward. A decrease in the density with

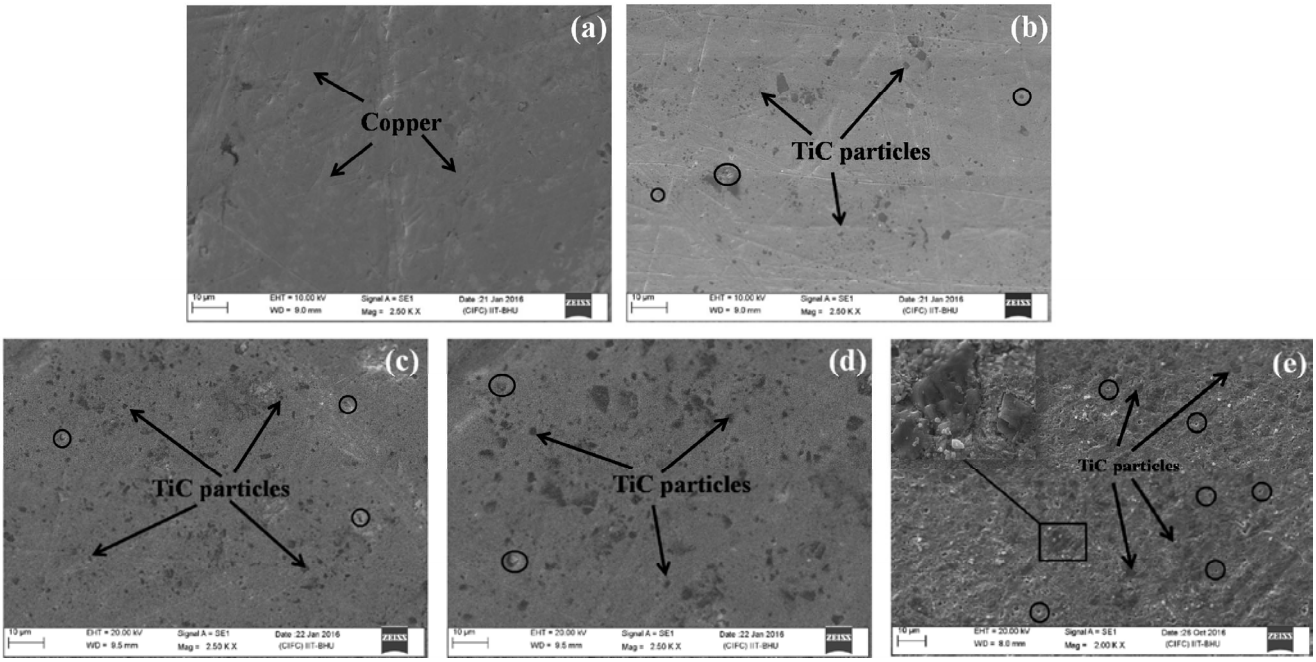

Fig. 3 SEM micrographs of (a) Cu4Ni matrix alloy, (b) Cu4Ni-2TiC, (c) Cu4Ni-4TiC, (d) Cu4Ni-6TiC, and (e) Cu4Ni-8TiC.

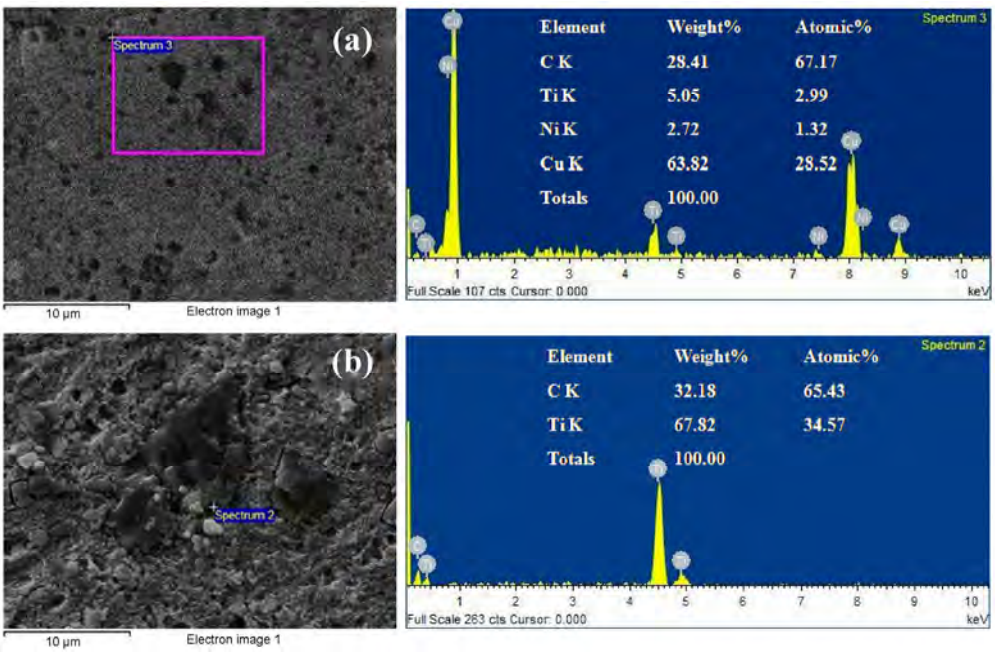

Fig. 4 EDS analysis of the marked portion of the micrographs (a) Cu4Ni-4TiC and (b) Cu4Ni-8TiC.

the increasing amount of TiC may be attributed to the TiC particle agglomeration, which promoted the pore formation and resulted in a reduced density [22].

The variation of the micro-hardness with the TiC content depicted in Fig. 6 showed that the hardness of the composite increased with the addition of TiC until 4 wt%, beyond which, it started decreasing. Relatively higher hardness values were obtained for 4 wt% TiC-reinforced composite with a hardness value of 109 HV. These values were almost 82% more than the matrix alloy. The hardness increase with the increase in the TiC amount from 2 wt% to 4 wt% can

be caused by the dispersion strengthening effect of the TiC particles. The thermal disparity between the reinforcing ceramic particles (TiC) and the matrix alloy resulted in the internal stresses that generated the dislocations leading to the increase of the dislocation density, which ultimately contributed to the improvement of the composite hardness [23]. After a certain amount of reinforcing particles (4 wt% in the present study), the composite hardness decreased, because of the increasing tendency of the TiC particle agglomeration that also resulted in the diminished load bearing capacity of the TiC. Another reason may be the increase in the actual inter-particle distance that adversely affected the hardness [24].

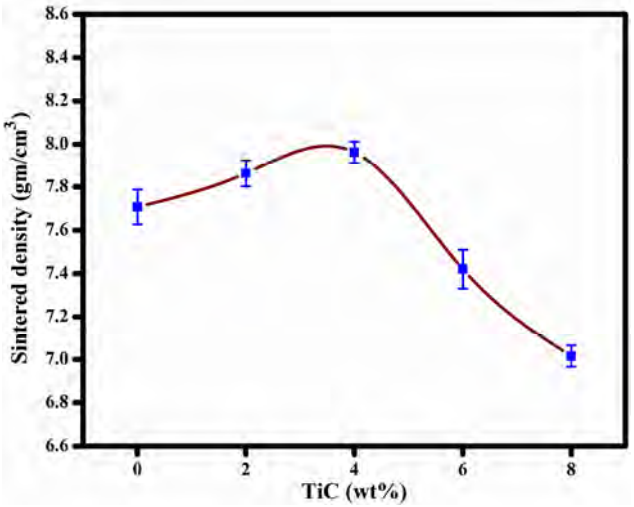

Fig. 5 Effect of TiC reinforcement on the density.

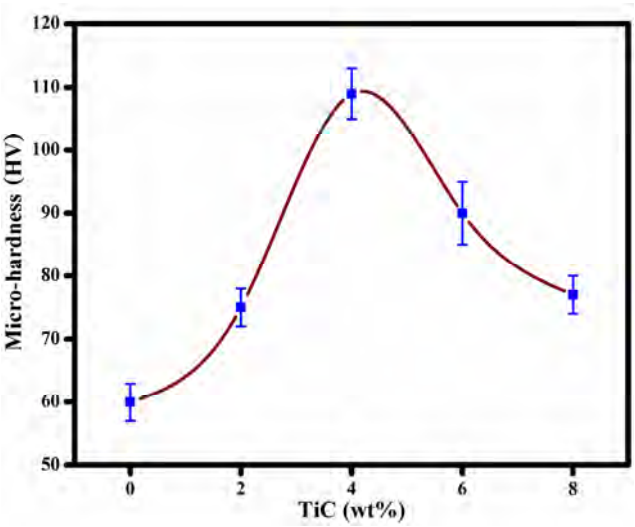

Fig. 6 Variation of micro-hardness with TiC content.

3.3 Friction and wear behavior

Figures 7(a) to 7(d) show the variation of the cumulative volume loss with the sliding distance for all the materials investigated in the present study under different loads of 5, 10, 15, and 20 N and at a constant sliding speed of 1.25 m/s. An almost linear increase in the cumulative volume loss with the increase in the sliding distance took place and confirmed through curve fitting by the linear least square fit. However, the data points were shown to join point by point in Fig. 7. Moreover, the volume loss of the matrix alloy (i.e., Cu4Ni) was consistently higher at all the normal loads in comparison to the composites. This result was not surprising because the hard TiC particles provided a shield to the relatively softer matrix during sliding and enhanced the load bearing capacity of the composites [25]. The volume loss among the composites decreased as the TiC amount increased from 2 to 4 wt%, beyond which, it again increased with the increase in TiC to 6 and 8 wt% at all the normal loads (Figs. 7(a) to 7(d)). Hence, Cu4Ni–4TiC showed the least volume loss, whereas Cu4Ni–2TiC exhibited the largest loss of volume among all the composites at all loads. This result may be attributed to a relatively higher hardness of the composite containing 4 wt% TiC in comparison to other composites.

The wear rate at a particular load was calculated from the slope of the variation of the cumulative loss with the sliding distance (Fig. 7) for Cu4Ni and the composites by fitting the data points through the linear least square fit. Figure 8 shows the wear rate variation with the normal load. The wear rate increased almost linearly with the load following Archard's law, which states that wear rate is directly proportional to the normal load, but inversely proportional to the hardness of the softer of the two mating materials [26]. The composites had a lower wear rate than the matrix alloy at all the loads, which may be credited to the higher hardness of the composites in comparison to the Cu4Ni matrix alloy. Among the composites, Cu4Ni–4TiC showed the lowest wear rate at all the normal loads used in the investigation, which may again be attributed to its hardness that was the highest in the present study. The wear rates shown by the other composites appeared to fall in the same band

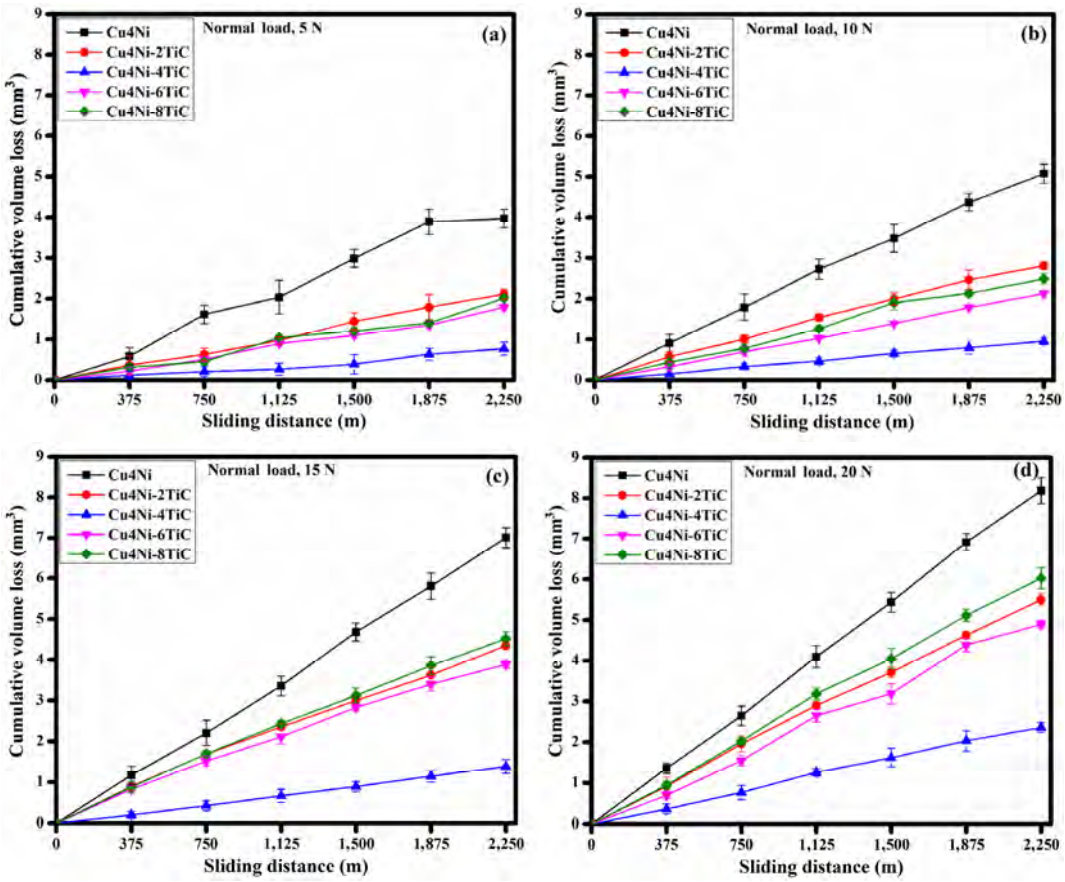

Fig. 7 Variation of cumulative volume loss with sliding distance at normal load of (a) 5 N, (b) 10 N, (c) 15N, and (d) 20 N for a constant sliding speed of 1.25 m/s.

at relatively lower loads. However, the difference appeared to increase with the increasing load, especially for Cu4Ni–8TiC (Fig. 8).

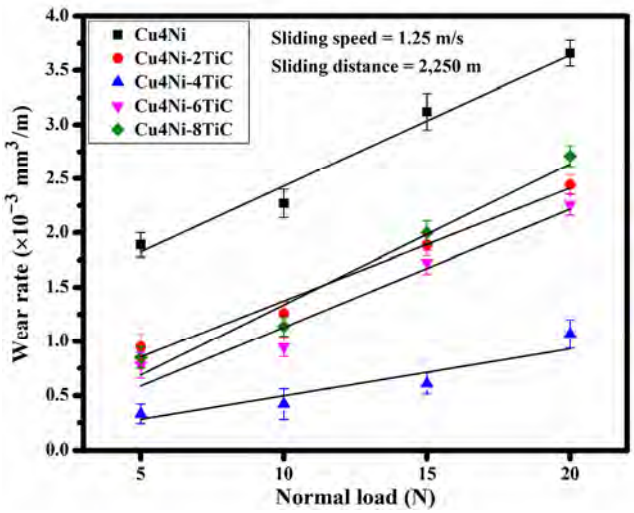

Fig. 8 Variation of wear rate with normal load.

Figure 9 shows the variation of the friction coefficient averaged over the distance slid (i.e., 2,250 m) with the normal load and at a constant sliding speed of 1.25 m/s for both Cu4Ni and composites. The average friction coefficient increased with the increasing load for all the composites synthesized in the present study. However, the friction coefficient for the Cu4Ni matrix alloy increased as the load increased from 5 to 10 N, then decreased as the load increased to 15 N, beyond which, it again increased until a 20 N load. Figure 9 illustrates that the friction coefficients shown by all the materials were from 0.78 to 0.92. The friction coefficient shown by Cu4Ni was the lowest, whereas that by Cu4Ni-8TiC was the highest at all the normal loads. The similar observations were reported by Celikyurek et al. [27].

One could observe that the friction coefficient increased with the increasing TiC content in the composites at a particular load, which may be attributed

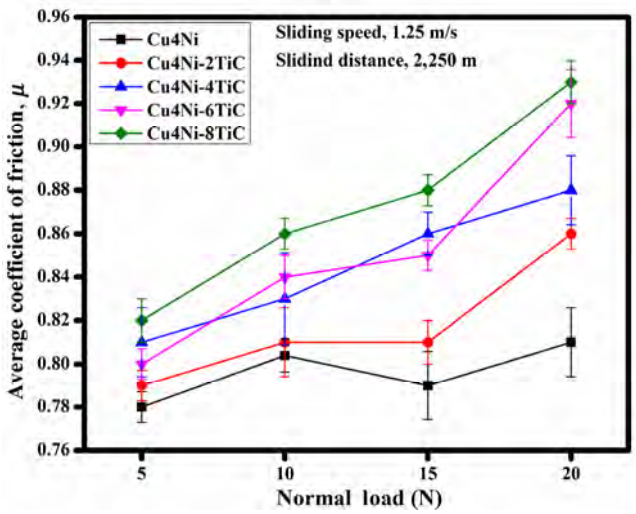

Fig. 9 Variation of average coefficient of friction with normal load.

to the abrasion caused by the TiC particles that get detached from the matrix with the increasing load and trapped between the contacting surfaces, which promoted the three body abrasion and resulted in an increased friction coefficient in the composites. An increase in the TiC content further aggravated the situation as more number of particles now get detached, thereby aiding abrasion. Hence, the friction coefficient increased with both the load and the TiC content. A relatively lower friction coefficient shown by Cu4Ni may be attributed to the relatively soft nature of the matrix in comparison to the composites as well as the absence of any abrasive action.

3.4 Worn surface analysis

Figures 10(a) to 10(c) show the SEM micrographs of the worn surfaces of the tested specimens at a normal load of 20 N after sliding a distance of 2,250 m. The SEM micrograph corresponding to the worn surface of Cu4Ni given in Fig. 10(a) exhibited the presence of the transfer layer of oxide containing the material transferred from the counter face. The extent of cover provided by this layer may explain the absence of the wear tracks, typical of the sliding process, which were not visible on the micrograph. However, this layer appeared to have been detached at some places (marked by arrow on the micrograph) from the substrate. The layer inhibited a metal–metal contact and provided a low shearing strength junction at the interface, thereby resulting in a reduced friction coefficient in comparison to the composites (Fig. 9). Figure 10(b) corresponding to the Cu4Ni–4TiC composite shows some fine wear tracks covered by the transfer layer of a well-compacted wear debris at some places along with particle pull-out at some locations. The SEM micrograph of the worn surface of Cu4Ni–8TiC depicted in Fig. 10(c) also showed the presence of a transfer layer that appeared to be a bit loose against the well-compacted layer in Fig. 10(b). However, no grooves were visible on the specimen surface, which may be caused by the filling of these groves by the loose wear particles, because Cu4Ni–8TiC has shown the largest volume loss among the composites. This could be confirmed from Fig. 7. The similar features were observed for the other composites, namely, Cu4Ni-2TiC and Cu4Ni-6TiC, with varying degrees of compaction and extent of cover provided by the transfer layer. However, these results were not shown herein. The presence of the fine grooves in Fig. 10 indicated an abrasive mechanism of wear in the composites, which might have been caused by the hard TiC particles pulled out from the matrix because of the poor bonding between TiC and the matrix despite the addition of Ni expected to improve the bonding. Furthermore, investigations must be conducted to examine the problems related to bonding. The pulled-out particles gave rise to abrasion until they were loose. However, during sliding, they get mixed with the other oxide and metallic particles that included the material transferred from the counterface and formed a transfer layer, which became compact because of frictional heating (Fig. 10(b)). A relatively higher friction coefficient shown by the composites in comparison to Cu4Ni may be caused by the abrasive action of these TiC particles. The friction coefficient among the composites increased with the increasing content of TiC (Fig. 9), which may be explained based on the chances of the TiC pull-out that are more in a composite containing relatively higher amount of TiC. These particles led to an enhanced abrasion resulting in a higher friction coefficient in composites containing a relatively larger amount of TiC. Despite a relatively lower friction coefficient, the wear rate shown by Cu4Ni was the largest and may be credited to a comparatively lower hardness of Cu4Ni in comparison to

the composites. The frictional heat during sliding aided the formation of oxide, which gets mixed with the detached wear particles and results in the formation of a transfer layer containing mixture oxides and metallic debris particles. This layer reached up to a critical thickness, after which it became unstable and got detached from the surface. It has been reported that a harder substrate is able to support a layer of larger thickness [28]. Cu4Ni has a relatively lower hardness compared to the composites. Hence, it can only support a transfer layer with a relatively smaller thickness before it detaches. This may explain the higher rate of the wear observed for Cu4Ni in comparison to the synthesized composites. Among the composites, Cu4Ni–4TiC has the lowest rate of wear, which again may be explained based on its relatively higher hardness and ability to hold a thicker transfer layer as explained earlier. The other contributing factor may be the presence of the well-compacted transfer layer in Fig. 10(b), which effectively reduced the metal–metal contact and resulted in a lower rate of wear as well as the friction coefficient in Cu4Ni–4TiC, against the loose transfer layer that appeared to have got detached at some locations (marked by arrows) illustrated in Fig. 10(c) corresponding to Cu4Ni–8TiC. Figure 11 depicts the typical EDS analysis of the marked portion of the worn surface micrograph of the Cu4Ni–4TiC pin. The presence of Fe in the EDS spectra confirmed that the metal transfer took place from the counter face. The presence of oxygen in the spectra indicated the possibility of oxidation that might have occurred during sliding.

From the above discussion, one can summarize that the addition of 4 wt% TiC in the Cu4Ni matrix alloy showed optimum hardness and tribological performance under the conditions of the load and the speed used in the present study. The operative mechanism was primarily abrasive in all the composites and a combination of adhesive and oxidative wear in the Cu4Ni matrix alloy. The TiC pull-out may be attributed to the weak bonding between the matrix and the reinforced particle in spite of the addition of Ni to improve the binding characteristics. Further investigations are required to examine the bonding-related problems.

4 Conclusions

1. The Cu4Ni–TiC composites were successfully synthesized by high-energy ball milling, followed by

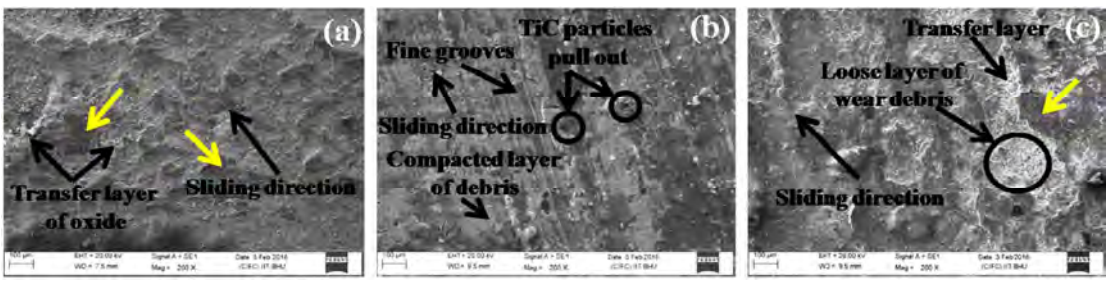

Fig. 10 SEM micrographs of worn surface of (a) Cu4Ni matrix alloy, (b) Cu4Ni-4TiC, and (c) Cu4Ni-8TiC at 20 N.

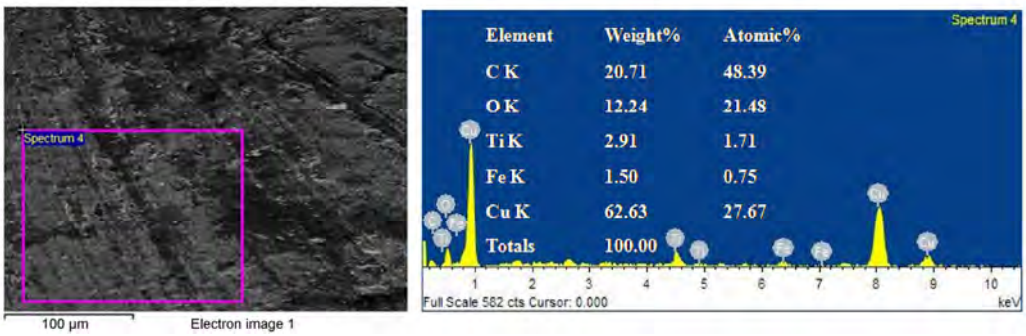

Fig. 11 Typical EDS analysis of the marked portion of the worn surface micrograph of Cu4Ni-4TiC pin.

compaction and sintering. The uniform distribution of the TiC particles can be observed from the microstructure. The hardness of the composite increased until the addition of 4 wt% of TiC, beyond which, it decreased.

2. The wear rate for the composites and the Cu4Ni matrix alloy increased linearly with the load. However, the composites showed a lower wear rate than the matrix alloy, which was correlated with the estimated hardness. The additions of 4 wt% TiC illustrated a better performance in terms of friction and wears, which was attributed to its relatively higher hardness and ability to hold a transfer layer of a relatively larger thickness in comparison to the other materials.

3. The average friction coefficient increased with the increasing load. However, the Cu4Ni matrix alloy exhibited the minimum value of the friction coefficient among all the materials investigated because of its relatively soft nature compared to the composites and the presence of the oxide layer over its surface that provided low shearing junctions at the interface. A relatively higher friction coefficient in the composites was credited to the abrasive action of the hard TiC particles.

4. The wear mechanism for the Cu4Ni matrix alloy was a mix of adhesive and oxidative wear and primarily abrasive for the composites containing hard TiC particles.

References

[1] Miracle D B. Metal matrix composites─From science to technological significance. *Comp Sci Tech* **65**: 2526–2540 (2005)

[2] Vettivel S C, Selvakumar N, Leema N, Lenin A H. Electrical resistivity, wear map and modeling of extruded tungsten reinforced copper composite. *Mater Des* **56**: 791–806 (2014)

[3] Jha P, Gupta P, Kumar D, Parkash O. Synthesis and characterization of Fe-ZrO_2 metal matrix composites. *J Comp Mater* **48**(17): 2107–2115 (2014)

[4] Kaftelen H , Ünlü N, Göller G, Öveçog ˘lu M L, Henein H. Comparative processing-structure–property studies of Al–Cu matrix composites reinforced with TiC particulates. *Compos: Part A* **42**: 812–824 (2011)

[5] Zhuang J, Liu Y B, Cao Z Y, Li Y Y. Microstructure and wear resistance of Cu-TiC composites fabricated by mechanical alloying and spark plasma sintering. *Adv Mater Res* **213**: 524–528 (2011)

[6] Ma W, Lu J. Effect of sliding speed on surface modification and tribological behavior of copper–graphite composite. *Tribo Lett* **41**: 363–370 (2011)

[7] Rosso M. Ceramic and metal matrix composites: Routes and properties. *J Mater Proce Techn* **175**: 364–375(2006)

[8] Torralba J M, da Costa C E, Velasco F. P/M aluminum matrix composites: an overview. *J Mater Proces Techn* **133**: 203–206 (2003)

[9] Suryanarayana C. Mechanical alloying and milling. *Prog Mater Sci* **46**: 1–184 (2001)

[10] Fathy A, Shehata F, Abdelhameed M, Elmahdy M. Compressive and wear resistance of nanometric alumina reinforced copper matrix composites. *Mater Des* **36**: 100–107 (2012)

[11] Dhokey N B, Paretkar R K. Study of wear mechanisms in copper-based SiCp (20% by volume) reinforced composite. *Wear* **265**: 117–133 (2008)

[12] Hong E, Kaplin B, You T, Suh M, Kim Y S, Choe H. Tribological properties of copper alloy-based composites reinforced with tungsten carbide particles. *Wear* **270**: 591–597 (2011)

[13] Tu J P, Rong W, Guo S Y, Yang Y Z. Dry sliding wear behavior of in situ Cu–TiB_2 nanocomposites against medium carbon steel. *Wear* **255**: 832–835 (2003)

[14] Li L, Wong Y S, Fuh J Y H, Lu L. Effect of TiC in copper–tungsten electrodes on EDM performance. *J Mater Proces Techn* **113**: 563–567 (2001)

[15] Akhtar F, Askari S J, Shah K A, Du X, Guo S. Microstructure, mechanical properties, electrical conductivity and wear behavior of high volume TiC reinforced Cu-matrix composites. *Mater Charac* **60**: 327–336 (2009)

[16] Buytoz S , Dagdelen F , Islak S, Kok M, Kir D, E Ercan. Effect of the TiC content on microstructure and thermal properties of Cu–TiC composites prepared by powder metallurgy. *J Ther Ana Calor* **117**: 1277–1283 (2014)

[17] Rathod S, Sharma M, Modi O P, Khare A K, Prasad B K. Effect of aluminium addition on densification behaviour and microstructural features of P/M processed Cu–TiC composites.

Inter J Mater Res **104**: 666–674 (2013)
[18] Sabbaghian M, Shamanian M, Akramifard H R, Esmailzadeh M. Effect of friction stir processing on the microstructure and mechanical properties of Cu–TiC composite. *Ceram Inter* **40**: 12969–12976 (2014)
[19] Rajkumar K, Aravindan S. Tribological performance of microwave sintered copper–TiC–graphite hybrid composites. *Tribo Inter* **44**: 347–358 (2011)
[20] Chrysanthou A, Erbaccio G. Enhancing the dispersion of TiC in copper. *J Mater Sci Lett* **15**: 774–775 (1996)
[21] Lee D W, Ha G H, Kim B K. Synthesis of Cu–Al_2O_3 nano composite powder. *Sci Mater* **44**: 2137–2140 (2001)
[22] Nemati N, Khosroshahi R, Emamy M, Zolriasatein A. Investigation of microstructure, hardness and wear properties of Al–4.5 wt.% Cu–TiC nanocomposites produced by mechanical milling. *Mater Des* **32**: 3718–3729 (2011)
[23] Arsenault R J, Shi N. Dislocation generation due to differences between the coefficients of thermal expansion. *Mater Sci Eng* **81**: 175–187 (1986)
[24] Ma Z Y, Li Y L, Liang Y, Zheng F, Bi J, Tjong S C. Nanometric Si_3N_4 particulate- reinforced aluminum composite. *Mater Sci Eng A* **31**: 219–229 (1996)
[25] Kumar A, Jha P K, Mahapatra M M. Abrasive wear behavior of in situ TiC reinforced with Al-4.5%Cu matrix. *J Mater Eng Perf* **23**: 743–752 (2014)
[26] Archard J F. Contact and rubbing of flat surfaces. *J App Phy* **24**: 981–988 (1953)
[27] Celikyurek I, Körpe N O, Olc¸er T, Gurler R. Microstructure, properties and wear behaviors of (Ni_3Al) reinforced Cu matrix composites. *J Mater Sci Tech* **27**: 937–943 (2011)
[28] Saka N, Teixeira J J P, Suh N P. Wear of two phase metals. *Wear* **44**: 77–86 (1977)

Pushkar JHA. He received his bachelor degree in mechanical engineering from I. K. Gujral Punjab Technical University (formerly Punjab Technical University), India, in 2007. He received his M. Tech. degree from Indian Institute of Technology (Banaras Hindu University), India, in 2011. He is currently pursuing Ph. D. degree in mechanical engineering from IIT (BHU), India. Areas of his research-interest include composite materials and tribology.

Rakesh Kumar GAUTAM. He is associate professor of mechanical engineering, IIT (BHU), Varanasi, India. He completed his B. E. degree from Madan Mohan Malviya Engineering College, Gorakhpur (1999), M. Tech. degree from Institute of Technology (2001) presently Indian Institute of Technology (BHU) Varanasi and PhD degree from Indian Institute of Technology (2009), Roorkee. He is working in the area of development of different types of composites, alloys and their physical, mechanical and tribological properties for various applications.

Rajnesh TYAGI. He is currently working as a professor of mechanical engineering at Indian Institute of Technology (Banaras Hindu University), Varanasi, India. He obtained his bachelor degree from Indian Institute of Technology Roorkee [IIT Roorkee] in 1992 and master and Ph.D. degrees in 1995 and 2001, respectively, from the same institute. His research interests include composite materials and tribology, solid lubrication, high temperature wear, and coatings tribology and superlubricity.

Friction **5**(4): 447–454 (2017)
DOI 10.1007/s40544-017-0158-6
ISSN 2223-7690
CN 10-1237/TH

RESEARCH ARTICLE

Effects of impact energy on the wear resistance and work hardening mechanism of medium manganese austenitic steel

Hui CHEN[1,2], Dong ZHAO[1], Qingliang WANG[1,*], Yinghuai QIANG[1], Jianwei QI[1]

[1] *School of Materials Science and Engineering, China University of Mining & Technology, Xuzhou 221116, China*

[2] *Jiangsu Key Laboratory of Large Engineering Equipment Detection and Control, Xuzhou Institute of Technology, Xuzhou 221111, China*

Received: 09 November 2016 / Revised: 07 January 2017 / Accepted: 14 March 2017

Abstract: Medium manganese austenitic steel (MMAS) fabricated through the hot rolling process has been used in the mining, military, and mechanical industries. In this paper, the abrasion performance and hardening mechanism were measured under a series of impact energies. The impact wear was tested at different impact energies from 0.5 J to 6 J using a dynamic load abrasive wear tester (MLD-10). Microstructure and surface morphologies were analyzed using scanning electron microscopy, X-Ray diffraction, and transmission electron microscopy. The results suggest that MMSA has the best wear resistance at 3.5 J and the worst wear resistance at 1.5 J. Furthermore, the wear mechanism and worn surface microstructure change with different impact energies. There are small differences between a large amount of martensite on the worn surfaces under different impact energies and the shapes of dislocation and twins change with different impact energies.

Keywords: medium manganese steel; impact abrasion wear; work hardening; twin; martensite; dislocation

1 Introduction

Since Sir Robert Hadfield invented Hadfield's steel in 1882, high manganese austenitic steel has been used in the mining, military, and mechanical industries as a wear-resistant steel, given its excellent work hardening properties under high impact energy conditions [1]. Previous studies mainly focused on the high manganese austenitic steel with 1−1.4 wt% C and 10−14 wt% Mn, which has a good combination of high strength and ductility [2−4].

In 1963, to improve the work hardening properties under low impact energy conditions, the American Metal Climax company introduced a modified medium manganese wear-resistant steel [5]. Compared with Hadfield steel, medium manganese steel has a higher work-hardening capacity and a better wear-resistant performance under low-stress abrasive conditions [6]. The work hardening ability and the wear-resistant performance of austenitic medium manganese steel increase by 60%−120% (the highest surface hardness is up to 700 HV) and 50%−140%, respectively [7].

The work hardening mechanism and performance of medium manganese austenitic steel have been studied. Jing and Jiang [8] discovered that the high-rate work hardening of medium manganese steel under impact abrasion wear is due to the transformation of strain-induced martensite, but they did not research the effect of different impact energies on the work hardening mechanism and degree. Another work by Nakada et al. [9] investigated the differences between ferrite and austenite formations of medium manganese steel in transformation behaviors, which revealed the transformation behavior between γ to α and α to γ at the transition temperature, but did not reveal any work hardening mechanism apart from martensite transformation. To increase the surface hardness of medium manganese austenitic steel (MMAS), Xu [10]

* Corresponding author: Qingliang Wang, E-mail: wql889@cumt.edu.cn

investigated the process of eutectic growth in as-cast medium manganese steel and explained the mechanism of modularization of the eutectic. Wang et al. [11] studied nano-crystallization and α-martensite formation in the surface layer of medium manganese austenitic wear-resistant steel caused by shot peening, revealing that different depths from the shot-peened surface have different grain sizes and α-martensite. Xu et al. [12] studied heat treatment effects on the microstructure and mechanical properties of medium manganese steel.

In mining machinery, impact abrasion wear is one of the most prevalent causes of failure. Hence, it is important to evaluate the impact abrasion wear performance of wear-resistant materials. Although the impact abrasion wear test is a complicated model for analysis, it provides excellent guidance for actual production. The difference between the work hardening mechanism and the abrasion performance of medium manganese austenitic steel (MMAS) under different impact energies in impact abrasion wear has not been researched. In this study, we evaluated the abrasion performance and work hardening mechanism of MMAS (0.9 C–9 Mn) at different impact energies; the microstructure and topography of the worn surface were also analyzed. The mechanism of abrasion performance and work hardening mechanism at different impact energies has been discussed.

2 Materials and methods

2.1 Materials

Medium manganese austenitic steel (MMAS) was treated by hot rolling and water-toughening. Table 1 shows the chemical compositions of the steel. The microstructure of MMAS is full of austenite; the hardness and impact toughness (ak) are 260.3 HV and 137 J/cm^2, respectively.

2.2 Experimental procedure

The abrasion wear was tested using an abrasive wear test machine (MLD-10) with dynamic load, which is shown in Fig. 1. The samples for the abrasive wear test measured 10 mm × 10 mm × 30 mm and were mounted on a holder that was connected to the bottom of a hammer. The hammer drove the case sample falling onto the bottom sample. Driven by the continuously rotating eccentric wheel, the hammer was in reciprocating movement. A high-carbon chromium bearing steel (hardness: 350.3 HV) was used as the low counterpart sample with 200 rpm. When the hammer dropped, the samples were impacted on the bottom samples; abrasive particles were present between the case and counterpart sample during the entire process. The impact energies of wear tests were changed from 0.5 J to 6 J. It is calculated by the equation:

$$AK = G \cdot H$$

in which AK is the impact energy, G is the gravity of hammer, and H is the falling height of hammer. Samples were subjected to impact 6,000 times; the abrasion material was quartz sand between 8 and 12 mesh and a flux of 50 kg/h. For each condition, three test groups were tested and the wear of the samples was quantified by mass loss measurements.

The hardness of the worn surface was measured by a HV hardness tester (tested load: 1.96 N); each sample was tested five times. The topography of the worn surface was characterized by scanning electron microscopy (SEM, Hitachi S-3000) and the microstructure of the worn sample surface was characterized by transmission electron microscopy (TEM, Tecnai G2-T20) and X-ray diffraction (XRD, Rigaku-Ultima-III).

Table 1 Chemical composition of MMAS steel (wt%).

C	Mn	Si	Cr	V	Mo	S	P
0.9	9	0.6	2	0.15	0.3	< 0.02	< 0.02

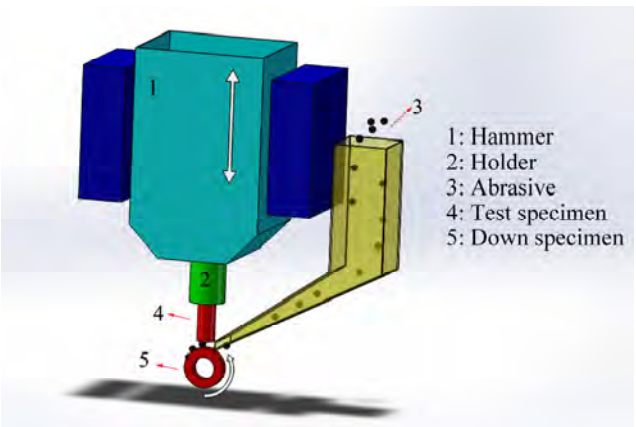

Fig. 1 Structure of the MLD-10.

3 Results

3.1 Abrasive wear performance

Figure 2 shows the relationship between the mass loss of the steel and impact energy for 6,000 impacts. As impact energy increases, the mass loss increases in the first (from 0.5 J to 1.5 J) and the third (from 3.5 J to 6.0 J) stages, while it decreases in the second stage (from 1.5 J to 3.5 J). MMAS shows the best abrasive wear resistance at the impact energy of 3.5 J and the worst wear resistance at the impact energy of 1.5 J. The mass loss of the 1.5 J impact energy sample is 259.02 mg, which is 1.78 times that at 3.5 J. The mass loss changes as the impact energy varies. The different wear performances of MMAS are attributed to the synthetic actions of surface hardness, work hardening degree, and wear mechanism influenced by the impact energy.

At lower impact energies (0.5–1.5 J), the impact stress of the wear layer is small and work hardening is not obvious. The mass loss caused by wear is greater than the effect of work hardening, which causes the mass loss to improve with the increase in impact energy. With increasing impact energy, the impact stress and work hardening of the wear layer increase significantly. The shear resistance of the wear layer improves, which reduces the cutting damage of abrasive particles to the wear layer. Consequently, the mass loss of wear reduces. When the impact energy exceeds 3.5 J, plastic deformation occurs in the wear layer under continued high cyclic stress. Crack initiation and propagation in the wear subsurface lead to fatigue fracture. Therefore, the mass loss of wear improves when the impact energy exceeds 3.5 J.

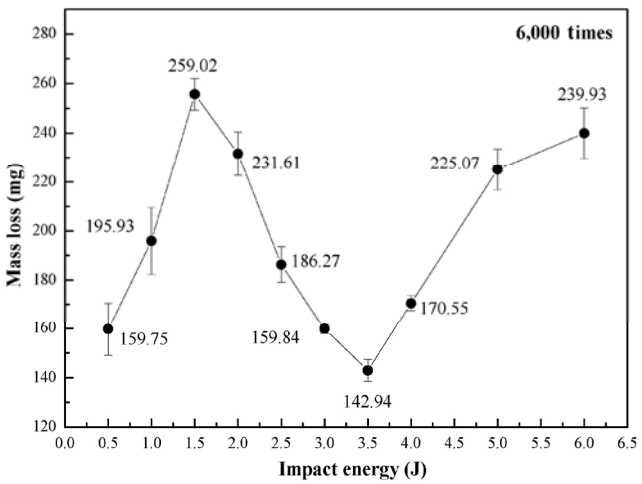

Fig. 2 The mass loss of the MMAS under different impact energies for 6,000 times.

3.2 Topography of the worn surface

Figure 3 shows the worn surface topographies of specimens at different impact energies. All surfaces are rough due to plastic deformation and the repeated impact of quartz sand. However, failure features of surface topography vary with the increase of the impact energy; there are mainly cuts, gouging pits, and plowing at 1 J, 1.5 J, and 2.5 J (Figs. 3(a), 3(b), and 3(c)), but it changes to fatigue spall at 3.5 J and 5 J (Figs. 3(d) and 3(e)). In addition, the cut pit at 1.5 J is larger and deeper than that at 1 J, and the fatigue spall of sample at 5 J is larger than that at 3.5 J.

3.3 Hardness of the worn surface

The hardness of the worn surface at different impact energies is shown in Fig. 4. As the impact energy increases, the hardness of the worn surface increases and it fluctuates around 575 HV when the impact energy exceeds 3.5 J. The hardness of the matrix is 260.3 HV, but the surface hardness increased to 385.3 HV at 0.5 J and the hardest surface is 587.6 HV when the impact energy is 3.5 J.

3.4 Subsurface hardness

Figure 5 shows the subsurface hardness of the sample at different impact energies (1 J–5 J). The work hardening degree is different at different impact energies. The work hardening depth is largest (about 2,200 μm) when the impact energy is 2.5 J; when impact energy exceeds 2.5 J, the depth is invariable. The subsurface hardness 50 μm from the surface at 2.5 J is 418.5 HV, and they are 421.2 HV, 440.3 HV, 464.6 HV, and 455.7 HV at 1 J, 1.5 J, 3.5 J, and 5 J, respectively. Though the hardness 50 μm from the surface at 2.5 J is smaller than those at 3.5 J and 5 J, the work hardening depth is approximate at 3.5 J and 5 J. In contrast, the work hardening depths of 1 J and 1.5 J are only 400 μm, in contrast with the samples whose impact energies exceeded 2.5 J.

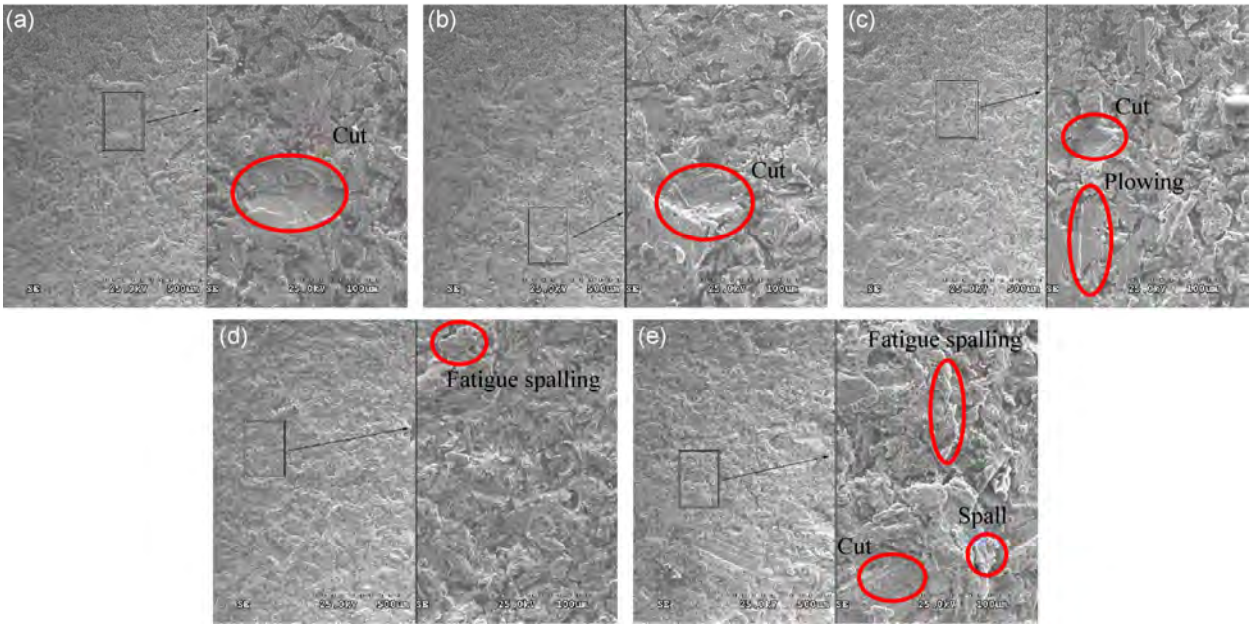

Fig. 3 The topography of the worn surface: (a), (b), (c), (d), and (e) are at 1 J, 1.5 J, 2.5 J, 3.5 J, and 5 J, respectively.

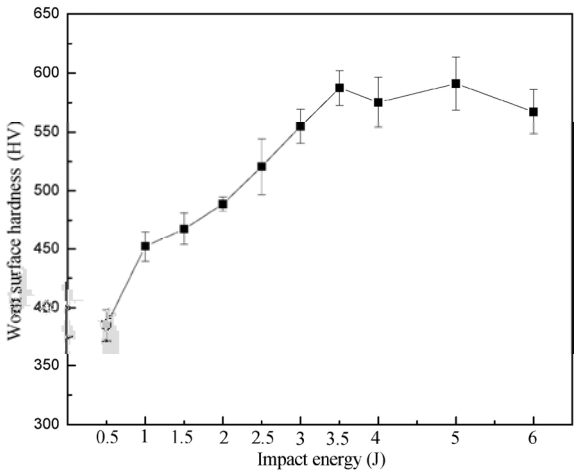

Fig. 4 The hardness of the worn surface.

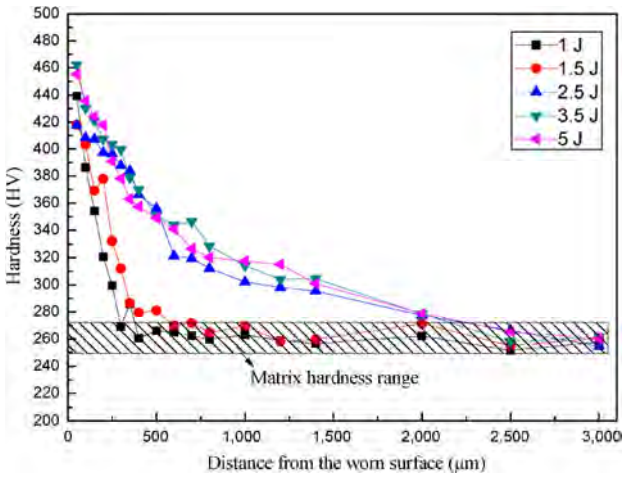

Fig. 5 The hardness of the subsurface.

3.5 The XRD results of the worn surface

The XRD patterns of the worn surface are shown in Fig. 6. The patterns for different impact energies are approximate, and there are two low intensity diffraction peaks indexed as bcc α-martensite besides three dominant peaks of fcc austenite.

Table 2 shows the amount of martensite on the worn surface. As shown, the amount of martensite accumulates slowly with the increase in impact energy. Compared with the maximum (35.9) and minimum (31.3) amounts of martensite at 4 J and 0.5 J, it can be seen that martensite transformation is approximate at

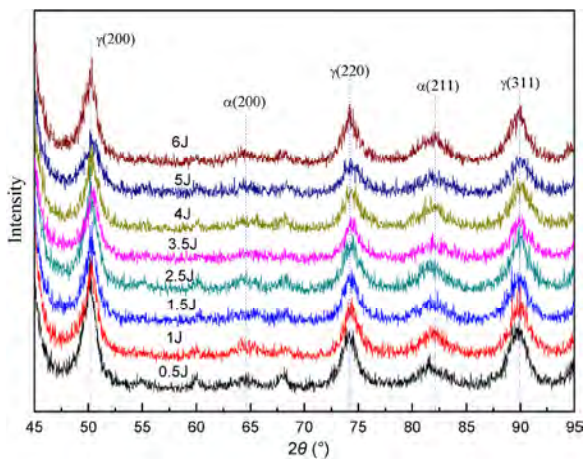

Fig. 6 XRD results of the worn surface under different impact energies from 0.5−6 J.

Table 2 The amount of martensite on worn surfaces.

Condition	0.5 J	1 J	1.5 J	2.5 J	3.5 J	4 J	5 J	6 J
Amount of martensite%	31.3	32.1	33.8	33.2	35.5	35.9	34.7	35.2

different impact energies and the martensite amount is stable when the impact energy exceeds 3.5 J.

3.6 TEM results of the worn surface

The microstructure of the subsurface is shown in Fig. 7. Figures 7(a) and 7(b) illustrate the TEM results at 1.5 J, while Figs. 7(c) and 7(d) are those at 3.5 J. Figure 7(a) shows a lath α-martensite in the austenite grain, and in Fig. 7(b) parallel acicular twins with stacking fault and dislocation wall are presented. In Fig. 7(c), there are lath twins accumulated together broader than those at 1.5 J. The α-martensite and island of dislocation are shown in Fig. 7(d), the shape of the dislocation is different from that at 1.5 J and the density of the dislocation in Fig. 7(d) is larger than that in Fig. 7(b).

4 Discussion

4.1 The wear performance and mechanism

The wear mechanism can be divided into three types: plowing, cutting, and wedge formation [13, 14]. In all abrasive wear modes, only the cut mode causes the removal of material; plowing and wedge formation lead to plastic deformation of the materials, which causes fatigue crack propagation. Hence, the wear performance strongly depends on the wear modes that are influenced by the mechanical property and abrasion conditions. In this study, the wear mechanism and hardness of the worn surface vary when the impact energy increases. When the impact energy is smaller than 2.5 J, the wear mode is mainly cutting; when the impact energy exceeds 2.5 J, it is mainly wedge formation. The multiply plastic deformation causes fatigue spall on the worn surfaces. Different wear mechanisms are caused by variation of the work hardening degree and the impact energy.

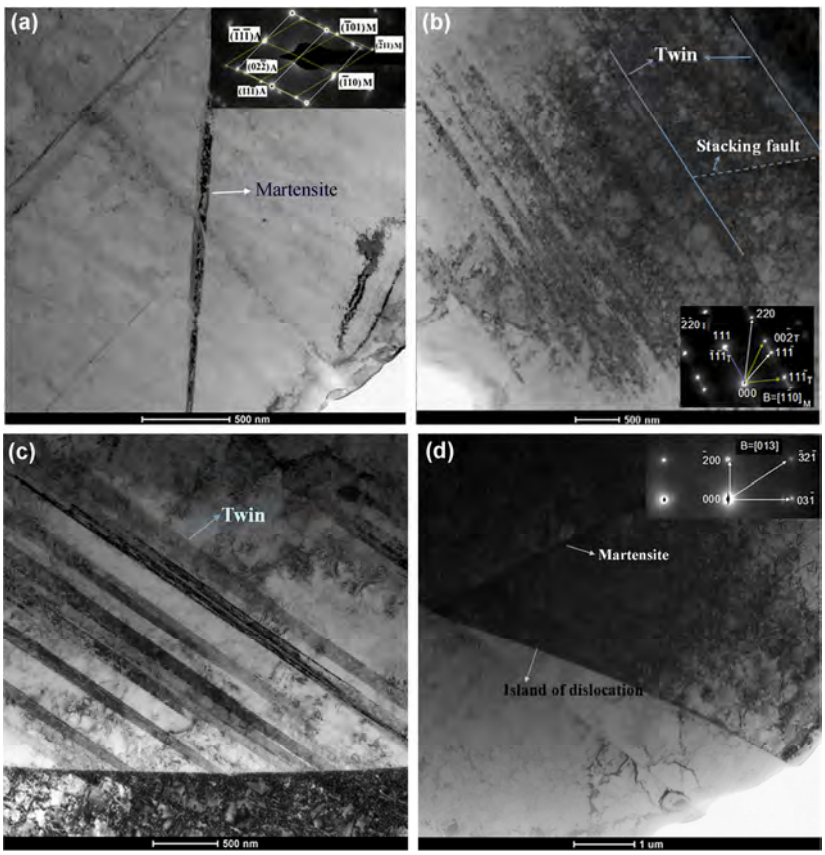

Fig. 7 The TEM results of the worn surface: (a) and (b) are the sample tested at 1.5 J impact energy; (c) and (d) are the sample tested at 3.5 J impact energy.

The difference between the worn surface's work hardening degree and work hardening depth are attributed to differences in the impact energies of the samples. Ojala et al. found that the work hardening and mechanical performance have a significant effect on wear performance [14].

As the impact energy increases from 0.5 J to 1.5 J, the worn surface hardness and work hardening depth accumulate slowly. The worn surface of the sample shows plowing and cutting when the impact energy is less than 1.5 J. In addition, the cut area and depth at 1.5 J are larger than those at 1 J due to the increase in impact energy. Therefore, the mass loss of MMAS increases with increasing impact energy in the first stage (from 0.5 J to 1.5 J).

In the second stage (from 1.5 J to 3.5 J), the work hardening degree increases with increasing impact energy. Although the hardness depths at 2.5 J and 3.5 J are similar, the surface hardness at 2.5 J is smaller than that at 3.5 J. With the increasing hardness of the surface and subsurface, the cut of the worn surface reduces so the mass loss decreases with increasing impact energy in the second stage.

The work hardening degree and hardening depth get saturated when the impact energy exceeds 3.5 J, but the strain increases with increasing impact energy. The multiply plastic deformation causes fatigue spall, so the surface is worn much easier with increasing impact energy. The pit and wedge formation increase and the mass loss increases when the impact energy exceeds 3.5 J, which leads to the increasing mass loss in the third stage (from 3.5 J to 6 J).

4.2 The work hardening mechanism

Allain et al. [15] and Dumay et al. [16] discovered that the plasticity mechanism changes with the variation of the stacking fault energy (SFE) as follows. It shows phase transformation when the SFE is less than 12 mJ/m^2 and the combined action of phase transformation and twinning when the SFE is between 12 mJ/m^2 and 18 mJ/m^2. There is twinning when the SFE is between 18 mJ/m^2 and 35 mJ/m^2, and slipping of the dislocation when the SFE exceeds 35 J/m^2. The SFE of MMAS has been calculated to be 16 mJ/m^2 [16–18], so the plastic deformation mechanism of austenitic steel is mainly twinning and phase transformation. Generally, materials with low SFE favor the twinning mechanism since the critical shear stress for twinning decreases with decreasing SFE, especially at high strain rates or low temperatures [19]. As shown above, variations of the worn surface's hardness and microstructure are presented at different impact energies. From the TEM results, the martensite transformation and the twinning are both indicated in the austenite grain at different impact energies.

At 1.5 J and 3.5 J, the amounts of martensite are 33.8% and 35.5%, respectively, and the hardness is 467.4 HV and 578.6 HV, respectively. It is observed that as the impact energy increases, the hardness accumulates and the amount of martensite measured is approximate. Therefore, martensite transformation is not the single key to the work hardening mechanism of MMAS.

Figure 8 shows the schematic summary of the microstructure features at different impact energies. With the increase of impact energy, the density of dislocations increases steeply, changing from cell to island and the twins are wider. The twin structure cuts the matrix and increases the strength [20]. The high density dislocation entanglement blocks the sliding of dislocations, which increases the plastic deformation resistance. So different shapes of dislocation and twins result at different degrees of work hardening. The different shapes of twins at different impact energies are caused by the different twin forming mechanisms.

The twin forming mechanism varies at different impact energies under two conditions. In Fig. 7(b), the twins are thin and there are stacking faults; the forming mechanism is self-partial-multiplication, which develops the twins by the reaction of the Shockley dislocation. In this forming mechanism, the Shockley should be located within the stacking fault, which is

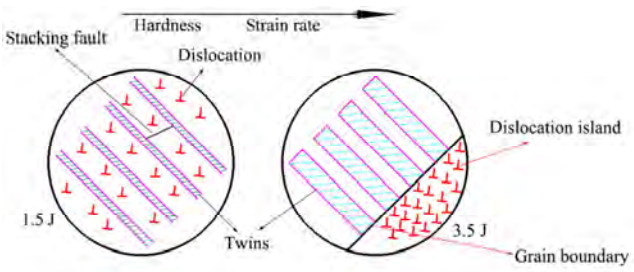

Fig. 8 Schematic summarizing the feature of twins and dislocation at different impact energies.

shown in Fig. 7(b). The twins at 3.5 J impact energy (Fig. 7(c)) are different from those at 1.5 J connected to the grain boundary, and the twin forming mechanism is the rebound mechanism in which the twin is produced by the rebounding of partial dislocations on the grain boundary. The two different twin forming mechanisms occur at different conditions: the rebound mechanism requires high strain rate and high stress but the self-partial-multiplication mechanism occurs at lower strain rate and stress [21]. The strain rates and stress increase with increasing impact energy. Therefore, the mechanism of twin forming shows variations at different impact energies. At high impact energy (3.5 J), the number of nucleation points and nucleation kinetics are higher than that at low impact energy (1.5 J), so the twins at 3.5 J are wider and denser. At the same time, the dislocation reproduces faster at higher impact energy than at lower impact energy due to the higher strain rate and stress. In addition, the dislocations entangle in the sliding process of plastic deformation. Therefore, the density of dislocations at 3.5 J is higher than at 1.5 J.

The different impact energies cause the variation in work hardening mechanisms, which determines the work hardening degree. In addition, work hardening degree and impact energy influence the wear mechanism of the worn surface. Finally, under the influence of wear mechanism and impact energy, the wear performance of MMAS varies at different impact energies.

5 Conclusions

In this paper, by using impact abrasion test methods at different impact energies, the abrasion resistance of the MMAS was evaluated by XRD, TEM, SEM, etc.

(1) In impact abrasion wear tests, the impact energy has a significant effect on the abrasion resistance of the steel. MMAS shows the best abrasion resistance at 3.5 J and worst abrasion resistance at 1.5 J.

(2) The wear modes of MMSA in impact abrasion wear tests are the combination of plowing, cutting, and fatigue spall. The wear modes vary at different impact energies. Cuts are the main wear mode at low impact energies, while fatigue spall is the main wear mode at high impact energies.

(3) MMSA has better hardening performance at 3.5 J; however, α-martensite transformation has the maximum limitation with increasing impact energy. Therefore, the shapes of twins and dislocations are the important work hardening mechanisms.

Acknowledgements

The present authors appreciate the financial support from the National Key Technology Support Program of China (Grant No. 2013BAEL3B00), Jiangsu Key Laboratory of Large Engineering Equipment Detection and Control (Grant No. JSKLEDC201403), the Fundamental Research Funds for the Central Universities (2015XKZD01), and National Basic Research Program of China (Project No. 2014CB046303).

Reference

[1] Michalon D, Mazet G, Burgio C. Manganese steel for abrasive environments: A conditioning process for Hadfield's manganese steel and a novel method of producing FAM bearings from the same material. *Tribol Int* **9**: 171–178 (1976)

[2] Efstathiou C, Sehitoglu H. Strain hardening and heterogeneous deformation during twinning in Hadfield steel. *Acta Mater* **58**: 1479–1488 (2010)

[3] Karaman I, Sehitoglu H, Gall K, Chumlyakov Y I, Maier H J. Deformation of single crystal Hadfield steel by twinning and slip. *Acta Mater* **48**: 1345–1359 (2000)

[4] Canadinc D, Sehitoglu H, Maier H J, Chumlyakov Y I. Strain hardening behavior of aluminum alloyed Hadfield steel single crystals. *Acta Mater* **53**: 1831–1842 (2005)

[5] Di X, Deng S, Wang B. Effect of pulse current on mechanical properties and dendritic morphology of modified medium manganese steel welds metal. *Mater Design* **66**: 169–175 (2015)

[6] Jost N, Schmidt I. Friction-induced martensitic transformation in austenitic manganese steels. *Wear* **111**: 377–389 (1986)

[7] He Z, Jiang Q, Fu S, Xie J. Improved work-hardening ability and wear resistance of austenitic manganese steel under non-severe impact-loading conditions. *Wear* **120**: 305–319 (1987)

[8] Jing T, Jiang F. The work-hardening behavior of medium manganese steel under impact abrasive wear condition, *Mater Lett* **31**: 275–279 (1997)

[9] Nakada N, Mizutani K, Tsuchiyama T, Takaki S. Difference in transformation behavior between ferrite and austenite formations in medium manganese steel. *Acta Mate* **65**: 251–258 (2014)

[10] Xu Z. Eutectic growth in as-cast medium manganese steel. *Mat Sci Eng A-Struct* **335**: 109–115 (2002)

[11] Wang T S, Lu B, Zhang M, Hou R J, Zhang F C. Nanocrystallization and α-martensite formation in the surface layer of medium-manganese austenitic wear-resistant steel caused by shot peening. *Mat Sci Eng A-Struct* **458**: 249–252 (2007)

[12] Xu H F, Zhao J, Cao W Q, Shi J, Wang C Y, Wang C, Li J, Dong H. Heat treatment effects on the microstructure and mechanical properties of a medium manganese steel (0.2C–5Mn). *Mat Sci Eng A-Struct* **532**: 435–442 (2012)

[13] Hokkirigawa K, Kato K. An experimental and theoretical investigation of ploughing, cutting and wedge formation during abrasive wear. *Tribol Int* **21**: 51–57 (1988)

[14] Khun N W, Liu E, Tan A W Y, Senthilkumar D, Albert B, Lal D M. Effects of deep cryogenic treatment on mechanical and tribological properties of AISI D3 tool steel. *Friction* **3**: 234–242 (2015)

[15] Ojala N, Valtonen K, Heino V, Kallio M, Aaltonen J, Siitonen P, Kuokkala V T. Effects of composition and microstructure on the abrasive wear performance of quenched wear resistant steels. *Wear* **317**: 225–232 (2014)

[16] Allain S, Chateau J P, Bouaziz O, Migot S, Guelton N. Correlation between the calculated stacking fault energy and the plasticity mechanism in Fe–Mn–C alloys. *Mat Sci Eng A-Struct* **378**–**389**: 158–162 (2004)

[17] Dumay A, Chateau J P, Allain S, Migot S, Bouaziz O. Influence of addition elements on the stacking-fault energy and mechanical properties of a austenitic Fe-Mn-C steel. *Mat Sci Eng A-Struct* **483**–**484**: 184–187 (2008)

[18] Li L, Hsu T Y. Gibbs free energy evaluation of the fcc(γ) and hcp(ε) phases in Fe-Mn-Si alloys. *Calphad* **21**: 443–448 (1997)

[19] Zhang J, Liu G, Wei X. Strengthening and ductilization potentials of nonmetallic solutes in magnesium: First-principles calculation of generalized stacking fault energies. *Mater Lett* **150**: 111–113 (2015)

[20] Jin J E, Lee Y K. Strain hardening behavior of a Fe–18Mn–0.6C–1.5Al TWIP steel. *Mat Sci Eng A-Struct* **527**: 157–161 (2009)

[21] Zhu Y T, Narayan J, Hirth J P, Mahajan S, Wud X L, Liao X Z. Formation of single and multiple deformation twins in nanocrystalline fcc metals. *Acta Mate* **57**: 3763–3770 (2009)

Hui CHEN. He received his bachelor and M.S. degrees in material science and engineering in 2006 from China University of Mining and Technology, Xuzhou, China. After then, he was a Ph.D student in the Chemical Technology School at the same university. He has recently obtained his Ph.D. degree in mineral materials engineering at China University of Mining and Technology. His research interests include wear-resistance steel, fuel cell, and nano composite materials.

Qingliang WANG. He received M.S. degree in metallurgy and material engineering from Chongqing University, China, in 1992. After then, he received his Ph.D. degree in mechanical engineering from China University of Mining and Technology, China, in 2004. He joined Institute of Tribology and Reliability Engineering at China University of Mining and Technology from 1992. His current position is a professor and his research areas include biological materials, surface engineering, and tribology of composite materials.